DESIGN AND CHARACTERIZATION OF A NEW HIGH-ENTROPY PEROVSKITE OXIDE FOR EFFICIENT THERMOELECTRIC APPLICATION

A thesis submitted towards partial fulfilment of the requirements for the degree of:

Master of Technology in Nano Science and Technology

Submitted by:

MOUSOM ROY

Roll No: **M4NST23016**

Registration No. **160429** of **2021-2022**

Under the guidance of

Prof. (Dr.) Kalyan Kumar Chattopadhyay

Head of Department, Department of Physics

Jadavpur University

Kolkata-700032

Course Affiliated to

FACULTY OF ENGINEERING AND TECHNOLOGY

JADAVPUR UNIVERSITY, KOLKATA, INDIA

2023

This page is left blank intentionally

MTech (Nano Science and Technology)

Course affiliated to:

Faculty of Engineering and Technology

Jadavpur University

Kolkata, India

CERTIFICATE OF RECOMMENDATION

This is in order to certify that the thesis entitled " **Design And Characterization Of A New High-Entropy Perovskite Oxide For Efficient Thermoelectric Application** " is a legitimate work done by Mousom Roy under our supervision and guidance for the purposes of fulfilling the requirement for the degree of Master of Technology in Nano Science and Nanotechnology in the School of Materials Science and Nanotechnology from the academic session 2021-2023.

Thesis advisor
Prof. (Dr.) Kalyan Kumar Chattopadhyay
Head of Department, Department of Physics,
Jadavpur University
Kolkata-700 032

Dean
Faculty Council of Interdisciplinary Studies,
Law and Management
Jadavpur University
Kolkata-700 032

Director
Dr. Sourav Sarkar
School of Materials Science and Nanotechnology
Jadavpur University
Kolkata-700 032

MTech (Nano Science and Technology)

Course affiliated to:

Faculty of Engineering and Technology

Jadavpur University

Kolkata, India

CERTIFICATE OF APPROVAL

I hereby endorse the foregoing thesis as an engineering study, conducted and presented in a manner satisfactory enough to justify its acceptance as an engineering study, in order to obtain the degree for which it has been submitted. This approval does not endorse or approve any statement made, opinion expressed or conclusion drawn therein, but merely approves the thesis for the purpose for which it has been submitted.

Committee of the final examination for evaluation of the Thesis.

_____

_____

_____

_____

_____

** Only in case the thesis is approved.

DECLARATION OF ORIGINALITY AND COMPLIANCE OF ACADEMIC ETHICS

I hereby declare that this thesis contains a literature survey and original research work by the undersigned candidate for the Master of Technology (Nano Science and Technology) program during the academic year 2021-2023. The information in this document has been gathered and presented according to academic standards and ethical conduct. I also declare that I have cited and referred to all materials and results that are not original to this work as required by these rules and conduct.

Name: MOUSOM ROY

Roll Number: M4NST23016

Registration Number: 160429 of 2021-2022

Thesis Title: **DESIGN AND CHARACTERIZATION OF A NEW HIGH-ENTROPY PEROVSKITE OXIDE FOR EFFICIENT THERMOELECTRIC APPLICATION**

SIGNATURE DATE

To the experiences we have never expected,

To the memories, dandelions and love I have been blessed with.

To my father, his love and sacrifices, and tears that never dries.

To the friends and family found along the way.

To the memories that are of a lifetime, and one more.

"I have loved the stars too fondly to be fearful of the night."

— Sarah Williams

To the ones I love, and hold dear to my weary soul, my heart.

Acknowledgements

Embarking on this remarkable journey, I find myself compelled to express profound gratitude to those whose unwavering support and encouragement have made this thesis a reality. Their presence has not only shaped this work but has also played a pivotal role in nurturing my growth as an individual and a researcher.

To my mother, Sandhya Roy, your struggles, sacrifices, and boundless love have been the bedrock of my journey. Your unwavering belief in me, your ceaseless support during the darkest hours, and your blessings have guided me through challenges with strength. I dedicate this accomplishment to you, knowing that your sacrifices have made it possible. Thank you, Maa.

My late father, Dr. Manoj Kumar Roy, lives on in my heart as the embodiment of unwavering faith and boundless dreams. Your blessings and sacrifices continue to inspire me, driving me to fulfill the dreams you held close to your heart. You will always be my guardian angel. I miss you, Dad.

I extend heartfelt thanks to my thesis guide, mentor, and teacher, Prof. (Dr.) Kalyan Kumar Chattopadhyay. Your guidance, mentorship, and cordial approach have not only facilitated my work but have also inspired a deep admiration. Your support has been pivotal in making the journey comfortable and the learning enriching. I learnt so much from you, including various life lessons you shared with us. I am deeply honored and wish to implement your teachings in our lives. Thank you so much, Sir.

To my esteemed teachers, Dr. Sourav Sarkar, Dr. Mahua Ghosh Chowdhury, and Dr. Chandan Kumar Ghosh, I am grateful for your teachings, insights, and constructive feedback that have broadened my perspective and honed my skills.

A special appreciation goes to my mentor, Souvik Bhattacharjee "dada." Your valuable inputs, guidance, and the opportunity to learn from you have been instrumental in expanding my horizons and developing new skills. Your insights have been a guiding light in my pursuit. When things were difficult or experiments were not satisfactory, your advices and memes came at rescue! Thank you, Dada!

To my brother, Sattyam Roy, your unwavering patience, understanding, and unflinching support have made you an exceptional ally. Your presence has been a source of strength, and your faith in me has fueled my determination. Thank you, my brother.

My dear friend, Nilanjana Mukherjee, your unwavering presence during the highs and lows, your helping hand in times of need, and your constant positivity have been a blessing. Your friendship is cherished. Thank you for believing in me.

I am deeply thankful to old friends Subham, Monojit Sarkar and Dipika whose contributions in building the experimental setup were instrumental in the success of this research. Your insights were precious.

To my best friends, Aditya Debapriya Gayen and Sourav Debnath, your camaraderie and support have illuminated this journey, both in work and daily life. Krishnendu Haldar, your assistance during challenging times has been invaluable.

I extend my appreciation to my friend Abhrajit Roy, a shy guy with so much potential. Thank you for helping me whenever I needed, my friend.

Thank you, my friends Aaishiki Saha, Surjayan Biswas, and my lab partner, Sampurna Mukherjee, Biplab, Kusmkoli, Dhara, Gaurav, Soumyajit, Susmita, Prantik, Tanveer, Imran for the shared experiences and camaraderie. I will always cherish our memories.

To seniors like Mrinmoy Da, Manas Da, Tanay Da, Pulak Da, Suvankar Da, Suvra Di, Nabamita Di, Dimitra Di, Dipayan Da, Nabanita Di, Dipanwita Di, and your guidance has been enlightening.

I extend my heartfelt gratitude to all those not mentioned explicitly, for your contributions, big and small, have been pivotal. To the collective support from friends, colleagues, and well-wishers who have been part of this journey, my sincere thanks.

Your generosity, encouragement, and positivity have played an integral role in making this accomplishment a reality. As we collectively look toward a brighter future, may our shared journey continue to be one of growth, inspiration, and collaboration.

With heartfelt appreciation,

Mousom Roy

Abstract

This thesis presents a comprehensive exploration of perovskite materials with a focus on novel high entropy perovskites (HEPs) and their potential as thermoelectric materials. Six distinct perovskite compositions were synthesized, characterized, and evaluated, culminating in the design and creation of two innovative high entropy perovskites, HEP-1 and HEP-2. The ABX3 structure, a hallmark of perovskite materials, was reimagined in HEP-2 with an unprecedented configuration involving La and Sr in site A, and Fe, Mn, Cu, Ni, Co, and Cr in site B, along with oxygen in site X.

The synthesis methodology employed a tailored sol-gel approach, followed by solvent-aided grinding and calcination. The rationale behind the design was to simultaneously enhance electrical conductivity while mitigating thermal conductivity through phonon dispersion mechanisms, with the ultimate goal of improving the power factor and figure of merit—a vital aspect of thermoelectric performance.

Characterization efforts encompassed structural, chemical, and physical analyses of the synthesized samples, including thin films and pellets. An Arduino-based device setup was meticulously crafted and customized from scratch to facilitate real-time data collection and analysis of thermoelectric properties. This experimental arrangement underscored the commitment to pushing the boundaries of thermoelectric research and technology.

The findings from this research highlight the relationship between composition, crystal structure, and thermoelectric performance. The synthesis of novel high entropy perovskites, especially the groundbreaking HEP-2 structure, offers new avenues for enhancing energy conversion and harvesting technologies. The optimization of power factor and figure of merit through improved electrical conductivity and tailored phonon dispersion holds substantial promise.

Table of Contents

List of Tables and Figures

XIII. **2.2.2 Seebeck coefficient of $CuAlO_2$ thin films**, A.N. Banerjee et al., "Thermoelectric and electrical properties of dc-sputtered copper aluminum oxide thin films," Thin Solid Films 474 (2005), pp. 261–266.

XIV. **2.3 XRD patterns of CNTS sample, EDS analysis, Raman spectra (a, b, c)**, Sarkar, S., Das, B., Midya, P. R., Das, G. C., & Chattopadhyay, K. K. (2015). Optical and thermoelectric properties of chalcogenide-based Cu2NiSnS4 nanoparticles synthesized by a novel hydrothermal route. Materials Letters, 152, 155-158.

XV. **2.4 Cu L2,3-edge XAS kinetics; PXRD analysis of HEO material transformation**, Fracchia et al. (2020) explored CO oxidation in high-entropy oxides (HEOs).

XVI. **2.6 Electrical properties and ZT of annealed $(Ca_{0.2}Sr_{0.2}Ba_{0.2}Pb_{0.2}La_{0.2})TiO_3$: (a) electrical conductivity; (b) Seebeck coefficient; (c) power factor; (d) ZT**., Zheng, et al. "High-Entropy Perovskite Oxides for Thermoelectric Applications." J Adv Ceram (2021) 10: 377-384."

XVII. **2.7 TEM (a), HRTEM (b), SAED (c) and HAADF corresponding EDS mapping of high-entropy CSBLP ceramic sintered at 1250°C-2h and then annealed at 1300°C-8h.**, Zhang, P., Lou, Z., Qin, M., et al. (2022). Synthesis and thermoelectric properties of high-entropy CSBLP ceramics. Journal of Materials Science & Technology, 97, 182-189.

XVIII. **2.8 Temperature dependence of conductivity of the samples $La_{1-x}Sr_xCrO_3$ (x¼0, 0.1, 0.2)**., Wang, S., Huang, K., Zheng, B., Zhang, J., & Feng, S. (2013). Mild hydrothermal synthesis and physical property of perovskite Sr doped LaCrO3. Materials Letters, 101, 86-89. doi:10.1016/j.matlet.2013.03.083

XIX. **2.9 SEM images of $La_{0.85}Sr_{0.15}Cr_{0.95}Ni_{0.02}Co_{0.02}O_3$ perovskite powder prepared by EDTA–citrate complexing method at (a) pH 4.9 and (b) pH 6.9. Samples were calcined at 800 ◦C for 2 h**., Ding, X., Liu, Y., Gao, L., & Guo, L. (2008). Synthesis and Characterization of Doped LaCrO3 Perovskite Prepared by EDTA–Citrate Complexing Method. Journal of Alloys and Compounds, 458, 346–350.

XX. **2.10 SEM micrographs of the nanocomposite with [Co/La]nominal = 0.055 (a) and of the supporting La2O3 (b)**, Natile, M. M., Glisenti, A., Faticanti, M.,

Grillo, F., & Martra, G. (2007). Synthesis, Characterization, and Reactivity of Lanthanum Cobalt Oxide Perovskites in Carbon Monoxide Oxidation. Applied Catalysis B: Environmental, 72(3-4), 351–362. doi:10.1016/j.apcatb.2006.12.007

XXI. **2.13 Electrical conductivity (s) and Seebeck coefficient (a) are plotted as a function of temperature**, Kumar, A., Thakur, A. D., & Tomy, C. V. (2018). Synthesis and Thermoelectric Effects of High Entropy Perovskites. Journal of Alloys and Compounds, 735, 1787-1791.

XXII. **2.11.2 a) Seebeck coefficient (a), (b) electrical resistivity (r) as a function of temperature for $(LaNdPrSmEu)_{1-x}Sr_xCoO_3$.**, Kumar, A., Dragoe, D., Berardan, D., & Others. (2022). Thermal Conductivity and Thermoelectric Properties of High-Entropy Rare-Earth Cobaltates. Journal of Materiomics

XXIII. **2.11.1 a) XRD pattern of $La_{0.95}Sr_{0.05}CoO_3$ and $(LaNdPrSmEu)_{0.95}Sr_{0.05}CoO_3$ are shown. The crystal structure using Vesta software is shown for (b) $La_{0.95}Sr_{0.05}CoO_3$, and (c) $(LaNdPrSmEu)_{0.95}Sr_{0.05}CoO_3$. The structural parameters are obtained from the Rietveld refinement of the XRD pattern**., Kumar, A., Dragoe, D., Berardan, D., & Others. (2022). Thermal Conductivity and Thermoelectric Properties of High-Entropy Rare-Earth Cobaltates. Journal of Materiomics

XXIV. **3.1 ESEM schematic diagram**, Wikipedia

XXV. **3.2. FESEM (Hitachi S-4800) set up**

XXVI. **3.3 Bragg's Law**, Wikipedia

XXVII. **3.4 X ray gun schematic,**

XXVIII. **3.5 XRD setup "D8 Advance Bruker"**

XXIX. **3.6 Basic working principle of UV-Vis spectroscopy**

XXX. **3.7 Diffuse and Specular Reflectance**

XXXI. **3.8 UV-VIS-NIS (SHIMADZU UV-3600) Spectrophotometer**

XXXII. **3.9 A simple spectrometer layout**

XXXIII. **3.10 Internal components of FTIR instrument.**

XXXIV. **3.11 Process of generating an FTIR spectra**

XXXV. **3.12 Electronic Balance**

1 Introduction

1.1 History of Nanotechnology

The year was 1959. Space Race just begun a year or so back and there was this impetus towards advancement in the field of science. Antarctic treaty was just signed nearly twenty days ago, which allowed international cooperation for scientific research. The memories of war and devastation of nuclear weapons was slowly being replaced by newer developments like the cold war between US and Soviets. Between these, on a sunny cool afternoon, December 29, 1959, amidst the festive mood and holidays, Dr. Richard P. Feynman, delivered a seminal talk titled “"There's Plenty of Room at the Bottom: An Invitation to Enter a New Field of Physics" at the annual American Society meeting in Beckman Auditorium, Caltech. He envisioned the remarkable potential of manipulating matter at the atomic scale. The concept of nanotechnology was a revolutionary idea at that time. He emphasized the importance of quantum mechanics in understanding the behavior of matter at such tiny scales and proposed the possibility of manipulating individual atoms and molecules to create new materials and devices with unprecedented properties. Nanotechnology is destined to change people’s lives more than anything in coming years, and the possibilities are truly endless.

Ancient civilizations have used the concepts of nanotechnology in many examples without any knowledge. In Keeladi, India, carbon nanotubes have been found in pottery dating to c. 600-300 B.C, though not known whether they were deliberately added or just pure chance [1].

Nanoparticles were used artisans dating as far back as ancient Mesopotamia for creating glittering effect on surface of pots [2]. In above cases, the practices were purely based on craft practices and passed on as working knowledge without much knowledge about the reasons of why nanoparticles or nanowires etc. worked the way do. Atoms have been considered indivisible for the majority of history. Works of scientists like Marie & Pierre Cuire, Becquerel, Thomson, Chadwick, Rutherford, Bohr and so on showed that atoms were in fact divisible, and it opened up a whole new world of new rules, governed by quantum mechanics. Minds like Planck, Einstein, Heisenberg, Dirac who made significant contributions to the field, and often considered as key founders of the field, they themselves were taken aback with the strangeness of quantum world and how much the properties and laws varied when compared to the macroscopic universe.

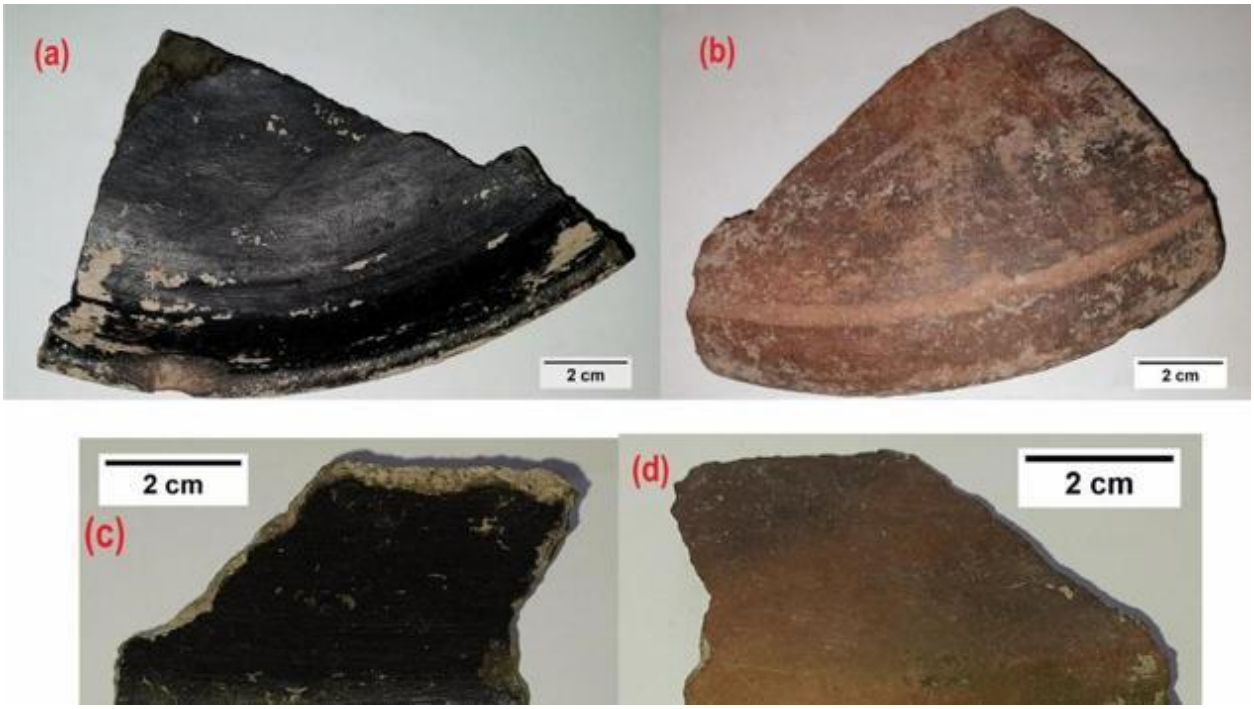

Fig 1.1 CNT coated earthen pots found in Keeladi, Tamil Nadu.,

Properties of materials at nanoscale often vary greatly often nearly opposite to that of bulk. Various properties like electrical and thermal conductivity, boiling point, melting point, refractive index and so on which are considered essentially intrinsic at bulk level, changes when compared at nanoscale. This allows some interesting solutions to the researchers for various applications. Nanotechnology, the term was first used by Norio Taniguchi of Tokyo University of Science in a 1974 conference and his definition was "'Nano-technology' mainly consists of the processing of, separation, consolidation, and deformation of materials by one atom or one molecule."[3] but the term was not used again until K. Eric Drexler, who was unaware of Taniguchi's prior use of the term, published his first paper on nanotechnology in 1981[4]. Though ideas regarding nanotechnology was gaining traction however, true developments began in the field with invention of Scanning Electron Microscope in 1981 by Gerd Binning and Heinrich Rohrer at IBM Zurich Research Laboratory, for which they were awarded Nobel Prize in Physics in 1986. Binning, along

with Clavin Quate and C. Gerber went on to invent Atomic Force Microscope in 1986. These tools allowed researchers to observe and manipulate objects at nanoscale.

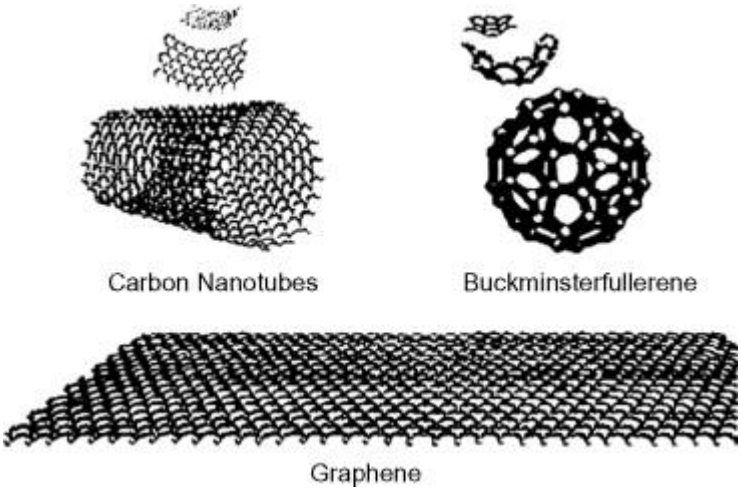

Fig 1.2 Types of carbon-based nanostructures

Around the same time, in the groovy year of 1985, a trio of intrepid scientists - Harry Kroto, Robert Curl, and Richard Smalley - embarked on an experiment that would take the world of science by storm. They were on a mission to understand the mysterious world of carbon clusters, those tiny building blocks of life lurking in the depths of stars and space. As they tinkered away in their lab, something extraordinary happened. Among the jumble of carbon clusters, they stumbled upon a peculiar and unexpected molecular species. It was a carbon molecule, but not just any carbon molecule. This one had precisely 60 atoms, cleverly arranged in a breathtaking hollow, spherical shape. Imagine a tiny, perfectly crafted soccer ball made of carbon atoms - and voilà! They had stumbled upon a "buckminsterfullerene." Now, one might wonder, why the fancy name? Well, these scientists had a flair for connecting the dots. They named the molecule after the brilliant architect and inventor Buckminster Fuller, known for his stunning geodesic domes - structures with similar shapes. And, because they couldn't resist, they affectionately coined the nickname "buckyballs," since they looked like tiny balls from a futuristic game called "buckyball." But wait, the adventure didn't end there.

The discovery of buckyballs sparked a wildfire of excitement in the scientific community. It wasn't just about finding a new type of carbon molecule; it was like opening a hidden door to a brand-new realm - the world of nanotechnology! Buckyballs were the pioneers of a whole family of fascinating carbon nanomaterials. They led the way for exploring other marvels, like carbon nanotubes and the famous graphene, a single layer of carbon atoms. Suddenly, scientists were

jumping down the rabbit hole of nanoscale wonders. And the cherry on top of this scientific sundae? In 1996, the Nobel Prize in Chemistry was awarded to Kroto, Curl, and Smalley for their groundbreaking discovery of buckyballs and their fantastic contributions to the burgeoning field of nanotechnology.

Before moving on to what is nanotechnology and its applications, lets quickly walk through the timeline of important milestones in this field in brief.

1.1.1 Timeline of Nanotechnology in Brief

- 1959: Richard Feynman envisioned the possibilities of manipulating individual atoms and molecules in his lecture "There's Plenty of Room at the Bottom," laying the groundwork for nanotechnology.
- 1981: Gerd Binnig and Heinrich Rohrer developed the scanning tunneling microscope (STM), allowing visualization and manipulation of atoms at the nanoscale.
- 1985: Harry Kroto, Robert Curl, and Richard Smalley discovered fullerenes, a new class of carbon molecules, including the famous Buckminsterfullerene or "buckyballs," expanding possibilities for nanomaterials.
- 1991: Sumio Iijima discovered carbon nanotubes (CNTs), opening a new frontier in nanomaterials research.
- 1996: Nadrian Seeman created the first DNA nanomachines, using DNA molecules to build nanostructures and devices.
- 2000: Researchers, including Richard W. Siegel and Chad A. Mirkin, developed dip-pen nanolithography, a precise nanoscale printing technique for nanomaterials.
- 2004: Andre Geim and Konstantin Novoselov discovered graphene, a single layer of carbon atoms with remarkable properties, sparking interest in 2D materials.
- 2010: Andre Geim and Konstantin Novoselov were awarded the Nobel Prize in Physics for their groundbreaking discovery of graphene.
- 2016: Jennifer Doudna and Emmanuelle Charpentier received the Nobel Prize in Chemistry for their development of CRISPR-Cas9, a revolutionary gene-editing technology with implications for nanomedicine.

- 2021: F. Duncan M. Haldane, J. Michael Kosterlitz, and David J. Thouless were awarded the Nobel Prize in Physics for their theoretical discoveries of topological phase transitions and phases of matter, with applications in quantum nanotechnology.
- These major events represent just a fraction of the rich history of nanotechnology. They highlight the pioneering efforts of brilliant minds who have driven the field forward, uncovering the potential of manipulating matter at the nanoscale for numerous applications in science, engineering, medicine, and beyond.

1.1.2 Advances in Microscopy: Unveiling the Nanoscale World

The journey into the realm of nanotechnology began with a quest to explore the infinitesimally small, a world previously hidden from human sight. Advancements in microscopy played a pivotal role in turning the hypothetical into the tangible, as researchers sought to visualize and manipulate objects at the nanoscale. This chapter delves into the remarkable evolution of microscopy techniques that opened windows into the nanoscale world.

In the mid-20th century, as the potential for manipulating matter at atomic and molecular levels captured the imagination of scientists, the limitations of conventional optical microscopes became apparent. The wavelength of visible light imposed a fundamental restriction on resolving structures smaller than the wavelength itself. Enter the scanning tunneling microscope (STM) and atomic force microscope (AFM), two revolutionary tools that defied these limitations.

The STM, introduced in the early 1980s, functioned on a principle that was both elegant and groundbreaking. It relied on the quantum phenomenon of electron tunneling – the flow of electrons between a sharp metallic tip and a sample surface separated by a nanoscale gap. By maintaining a constant current through this gap and precisely moving the tip, scientists could map the contours of individual atoms on a surface. Suddenly, the nanoscale world was no longer an enigma; it was a landscape of atoms and molecules that could be directly observed and manipulated.

The AFM followed suit, utilizing an entirely different concept. Instead of tunneling current, it measured the interaction forces between a sharp tip and the sample surface as it was scanned. This allowed researchers not only to visualize atoms and molecules but also to feel the forces

between them. The AFM could even be used to manipulate individual atoms and molecules, paving the way for the burgeoning field of nanomanipulation.

These microscopy techniques initiated a new era of nanoscience and nanotechnology. They offered a view into the intricacies of nanoscale structures, enabling researchers to study the properties and behaviors of materials with unprecedented precision. Furthermore, they provided a playground for exploring the principles of quantum mechanics and molecular interactions in ways previously deemed unfeasible.

The advances in microscopy were not limited to the laboratory; they fueled innovations in fields ranging from materials science to medicine. Scientists and engineers began to engineer materials at the atomic level, tailoring their properties for specific applications. The impact of these breakthroughs resonated across industries, from electronics and energy to healthcare and beyond.

The story of advances in microscopy is a testament to human curiosity and ingenuity. By conquering the barriers of optical limitations, researchers gained access to a universe of tiny wonders, setting the stage for the remarkable developments that have characterized the field of nanotechnology. The STM and AFM were the keys that unlocked the door to the nanoscale world, a world that continues to astonish, inspire, and transform our understanding of the building blocks of matter.

1.1.3 Challenges and Future Prospects: Navigating the Path Ahead in Nanotechnology

As nanotechnology accelerates towards new horizons, a landscape of immense promise and intricate challenges unfolds before researchers, engineers, and society at large. The realm of the very small holds unparalleled potential for transforming industries, medicine, and our understanding of nature itself. Yet, with these possibilities come profound questions that demand careful consideration and innovative solutions.

At the forefront of the nanotechnology narrative lies the puzzle of precision. The manipulation of matter at the nanoscale necessitates an unprecedented level of control. As structures shrink to the atomic and molecular levels, the effects of quantum mechanics and surface forces become increasingly dominant. Ensuring reproducibility, scalability, and stability in

nanoscale manufacturing becomes an intricate dance with these underlying phenomena. Researchers grapple with developing techniques that guarantee uniformity in production while harnessing the inherent variability that emerges at such diminutive dimensions.

Ethical and safety concerns emerge hand in hand with technological breakthroughs. The potential impact of nanoparticles on health and the environment is a topic of intense scrutiny. Understanding the interactions between nanomaterials and living systems is a complex endeavor that demands interdisciplinary collaboration. Regulation and risk assessment struggle to keep pace with the rapid evolution of nanotechnology, as stakeholders' endeavor to strike a balance between innovation and responsible development.

Innovation in nanotechnology also extends to energy solutions. The potential for highly efficient energy storage, improved solar cells, and enhanced catalysts raises hopes for a more sustainable future. Yet, transitioning from laboratory prototypes to large-scale implementation requires overcoming challenges related to cost, scalability, and integration with existing systems.

The convergence of nanotechnology with other cutting-edge fields, such as artificial intelligence and biotechnology, introduces a new dimension of complexity. The symbiotic relationship between these domains holds transformative potential. For instance, nanotechnology could revolutionize medical diagnostics and treatment delivery when coupled with advances in AI and personalized medicine. However, navigating this synergy demands interdisciplinary thinkers who can bridge the gaps between traditionally distinct disciplines.

Despite these challenges, the allure of nanotechnology remains irresistible. Exploring uncharted territories at the nanoscale unveils novel properties of materials and introduces revolutionary approaches to problem-solving. The development of nanomaterials with tailored properties and functionalities continues to surprise scientists and engineers, sparking inspiration across industries.

1.2 Nanotechnology and Its Importance

1.2.1 Types of Nanomaterials

Nanomaterials, materials with unique properties due to their nanoscale dimensions, have garnered significant attention in recent years for their potential applications in various fields, from electronics and medicine to energy and environmental remediation. The term "nanomaterials" encompasses a diverse array of materials that can be categorized based on their composition, structure, and properties. Let's quickly glance through some common nanomaterials with applications.

- **Nanoparticles:** Nanoparticles are nanoscale entities with at least one dimension measuring 1 to 100 nanometers. They can be made from a variety of materials, including metals, semiconductors, oxides, and polymers. Nanoparticles often exhibit unique size-dependent properties, such as enhanced catalytic activity, optical properties, and surface reactivity. They find applications in drug delivery, sensors, catalysts, and electronics.
- **Nanotubes:** Carbon nanotubes (CNTs) are cylindrical structures made of carbon atoms arranged in a hexagonal lattice. They possess exceptional mechanical strength, electrical conductivity, and thermal conductivity. CNTs have applications in nanoelectronics, composite materials, and even potential applications in space elevators.
- **Nanowires:** Nanowires are elongated structures with diameters on the order of nanometers and lengths on the order of micrometers. They can be made from various materials, including metals, semiconductors, and insulators. Nanowires are utilized in nanoscale electronics, sensors, and photovoltaic devices.
- **Nanoplates:** Nanoplates are thin, plate-like structures with nanoscale thickness and larger lateral dimensions. They exhibit unique properties due to their anisotropic geometry. Nanoplates are used in catalysis, energy storage, and biomedical applications.
- **Nanorods:** Similar to nanowires, nanorods are elongated structures with nanoscale dimensions. However, nanorods often have larger diameters and can have various shapes, such as cylindrical, hexagonal, or tapered. They are utilized in photonics, sensing, and drug delivery.

- **Nanosheets:** Nanosheets are two-dimensional nanomaterials with a high aspect ratio. Graphene, a single layer of carbon atoms arranged in a honeycomb lattice, is a well-known nanosheet. Nanosheets are investigated for applications in electronics, energy storage, and flexible displays.
- **Nanoporous Materials:** Nanoporous materials have a network of pores with dimensions in the nanometer range. They can be used for gas storage, separation, and catalysis. Metal-organic frameworks (MOFs) and zeolites are examples of nanoporous materials.
- **Quantum Dots:** Quantum dots are semiconductor nanocrystals that exhibit quantum mechanical properties due to their small size. They have tunable optical properties and find applications in displays, imaging, and biological labeling.
- **Nanocomposites:** Nanocomposites are materials composed of two or more distinct phases, with at least one phase having nanoscale dimensions. By incorporating nanoscale fillers, such as nanoparticles or nanofibers, into a matrix material, nanocomposites can achieve enhanced mechanical, electrical, and thermal properties.
- **Nanoparticles with Functional Coatings:** Nanoparticles can be coated with functional layers to tailor their properties for specific applications. For example, magnetic nanoparticles coated with biocompatible materials can be used for targeted drug delivery and hyperthermia cancer treatment.
- **Nanoporous Membranes**: Nanoporous membranes consist of nanoscale pores that allow selective passage of molecules based on size and charge. These membranes have applications in filtration, water purification, and separation processes.
- **Nanostructured Thin Films:** Nanostructured thin films are deposited onto surfaces with controlled nanoscale morphology. They have applications in optics, electronics, and photovoltaics.
- **Nanogels:** Nanogels are three-dimensional networks of polymer chains that can encapsulate and release molecules, making them promising for drug delivery and tissue engineering.
- **Nanofibers:** Nanofibers are extremely thin fibers with diameters in the nanometer range. They find applications in tissue engineering, filtration, and electronics.

1.2.2 The need of Nanotechnology

Nanotechnology, or nanotech for short, is a field that involves working with matter on tiny scales, dealing with atoms, molecules, and supramolecular structures for various industrial purposes. The journey of nanotechnology began with a particular goal: the precise manipulation of atoms and molecules to create products on a larger scale, known as molecular nanotechnology. Imagine a world where we can engineer materials at the tiniest levels, crafting them atom by atom to create groundbreaking innovations. This was the vision of molecular nanotechnology. But as the field evolved, so did our understanding. A more comprehensive definition emerged from the National Nanotechnology Initiative, which expanded the horizon of nanotechnology beyond a single goal.

According to this broader definition, nanotechnology now encompasses anything involving the manipulation of matter that falls within the tiny size range of 1 to 100 nanometers (nm). At this quantum realm scale, the rules of quantum mechanics come into play, bestowing extraordinary properties upon materials. Nanotechnology now covers a wide range of research and technologies, all seeking to harness the special and magical properties that arise when things are super small. In essence, nanotechnology unlocks a world of possibilities, where we can explore the extraordinary and transform how we build, create, and innovate.

Now one might argue what is the general benefit of manipulation of materials at nanoscale except the obvious, production which needs any materials having at least one dimension in nano scale. Well, in that case, there are a large number of reasons why often nano materials are preferred than their bulk counterparts. Nanostructured materials often exhibit exceptional strength and hardness compared to their bulk counterparts. For instance, nanostructured metals like nano twinned copper demonstrate superior mechanical properties, making them ideal for reinforcing lightweight materials in aerospace and automotive applications. They possess a significantly larger surface area per unit mass than bulk materials. This unique characteristic makes them perfect for applications in catalysts, such as platinum nanoparticles in fuel cells, where increased surface area enhances reaction rates. Zero-Dimensional Quantum dots (QDs), semiconductor nanocrystals, showcase extraordinary optical properties that differ from bulk materials. Quantum dots emit specific colors of light based on their size, making them valuable in advanced display technologies

and medical imaging. In some cases, nanoscale materials exhibit enhanced thermal conductivity compared to bulk materials. For example, carbon nanotubes demonstrate excellent thermal conductivity and find applications in heat dissipation for electronics. However, nanoscale materials can have lower thermal conductivity than their bulk counterparts also. One prominent example of this phenomenon is seen in nanocrystalline materials. Nanocrystalline materials are characterized by grains or crystalline domains with sizes in the nanometer range. Due to their small grain size, the phonon scattering, which is the main mechanism for thermal transport in crystalline materials, becomes more effective. Phonons are quantized vibrational energy waves that carry heat in solids. In bulk crystalline materials, phonons can travel relatively long distances with minimal scattering, resulting in higher thermal conductivity. However, in nanocrystalline materials, the boundaries between the nanoscale grains act as barriers for phonon transport. When phonons encounter these grain boundaries, they experience scattering, which reduces their mean free path and, consequently, lowers the overall thermal conductivity of the material.

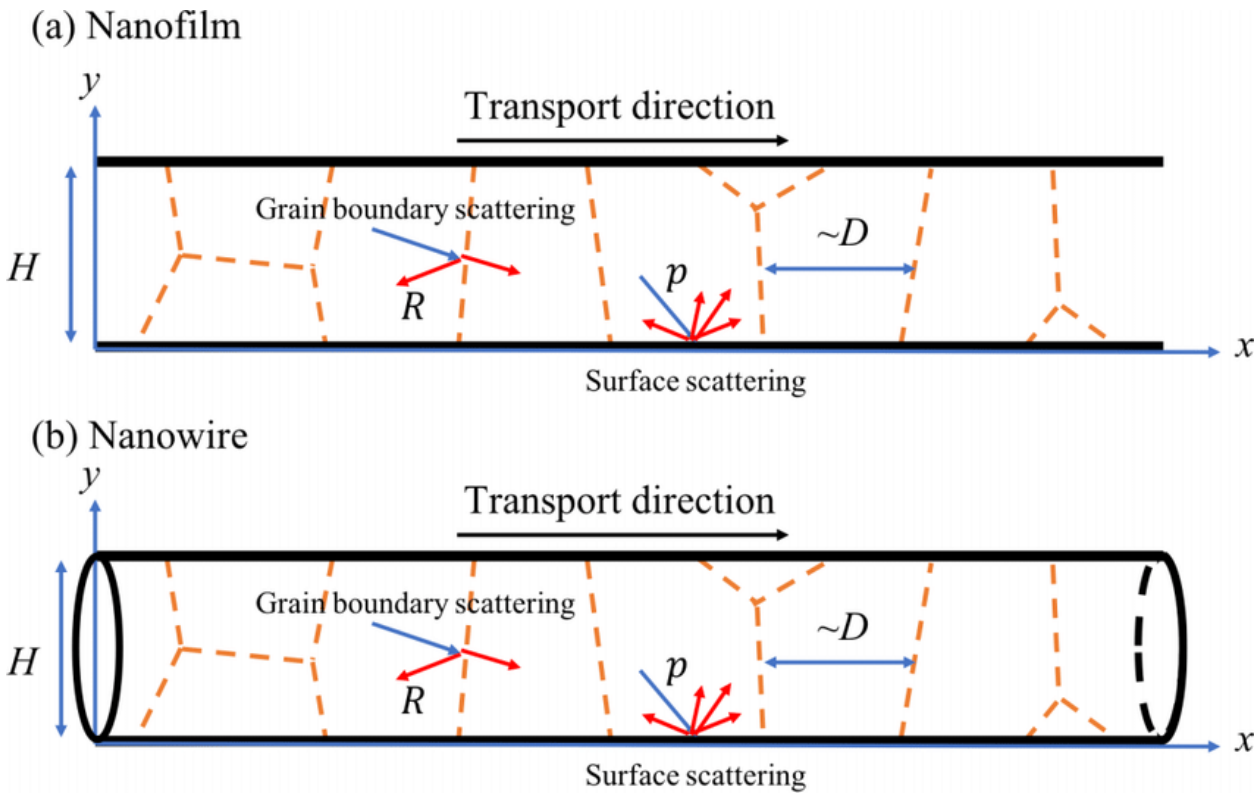

Fig 1.3 (a, b) phonon scattering in nanofilm and nanowires.

An excellent example of this behavior is observed in nanocrystalline silicon. Bulk silicon has relatively high thermal conductivity, making it a prevalent material for thermal management in electronics. However, when silicon is synthesized as nanocrystals or thin films with nanoscale grain boundaries, its thermal conductivity decreases significantly. This reduced thermal conductivity can be advantageous for certain applications, such as thermoelectric materials, where lower thermal conductivity is desired to enhance the efficiency of converting heat to electricity.

Nanotechnology allows for the fine-tuning of electrical conductivity in materials. Graphene, a single layer of carbon atoms, possesses remarkable electrical conductivity, making it a promising candidate for flexible electronics and energy storage devices. Nanoparticles with tailored sizes and shapes exhibit distinct magnetic properties. Magnetic nanoparticles are employed in medical imaging as contrast agents and targeted drug delivery vehicles.

Now why do these properties differ between bulk and nano? The variations arise from quantum effects and increased surface interactions in nanomaterials. At the nanoscale, the number of atoms or molecules becomes limited, leading to unique properties not observed in bulk materials. For example, the quantum confinement effect in semiconductor nanoparticles causes changes in their electronic band structure, leading to altered optical properties. Additionally, nanomaterials' increased surface area-to-volume ratio enables stronger surface interactions, influencing their behavior. This results in different mechanical, electrical, and chemical responses compared to their bulk counterparts.

1.2.3 Applications of Nanotechnology

Nanotechnologies have significant applications in medicine, electronics, energy, environmental remediation, materials, food and agriculture, consumer products, space exploration, water filtration, automotive, and military. Nanomedicine offers targeted drug delivery, improved imaging, and diagnostics. Electronics improves energy storage and conversion, while nanomaterials address environmental challenges. Nano-coatings offer water and stain resistance, UV protection, and antibacterial properties. Food and agriculture use nano sensors, pesticides, and fertilizers. Automotive uses nano coatings for scratch resistance and improved fuel efficiency.

1.3 Thermoelectric Effect

1.3.1 Story of Heat and Temperature

Imagine being a small boy living in some cave before the discovery of fire. Life was cold, scary, dangerous and unimaginable by people living in our age. We often take the presence of fire in our lives for granted. However, it was the pivotal moment in our short history on this blue dot. Fire not only provides us with light to keep darkness away, but also provides us warmth, ability to cook food, melt metals and eventually give birth to industrial age. Fire somewhat jumpstarted human civilization and changed the game forever. Heat. It was the key, as early humans figured. It enables us to survive harshest winters, and also can be harnessed to make the likes of engines that took men to moon. It's that transformative. That's how the story begun.

Civilization after civilization added more knowledge about heat- its nature, how it flows, and what can be done with it except the obvious- to heat anything. Much progress came as post renaissance as industrial revolution started taking its shape. Electricity, just like heat, had immense effect over mankind and its progress. In our present era we electricity is essentially ubiquitous in every aspect of life. From birth to death, we are surrounded by electrical and electronics systems. Such dependence also comes at a cost, the need of more energy to meet our needs. The need of electricity has also increased due to impetus towards greener, renewables sources of energy. Various sources of energy like solar, wind, hydrothermal, OTEC, nuclear and so can be harnessed and converted into electrical energy to use and store for many applications. Heat could be one such source.

Well, heat has been used historically to power cities. Thermal power plants essentially use any source of heat (coal, natural gas, petroleum etc.) to vaporize water into steam which is then used to run turbines and generators. But this process involves production of heat to generate power, rather than any difference in temperature.

Now heat and temperature are related, yet distinct. Let us imagine a lively dance floor where particles move to the rhythm of energy - that's heat. Heat is the energy transferred from one object or substance to another due to a temperature difference. It's like the party-goers passing their energy to neighboring dancers, causing the atmosphere to heat up and the excitement to spread. The amount of heat transferred depends on factors like the specific heat capacity and mass of the substances involved, as well as the duration of their interaction. Now, temperature takes center

stage, setting the mood for the dance. It's a measure of the average kinetic energy of the particles in a substance. Picture it as the rhythm that guides the dancers' movements - the faster they move, the higher the temperature, and vice versa. Temperature is an intensive property, meaning it remains constant regardless of the amount of substance. Here's the captivating connection between the two: heat loves to move towards regions of lower temperature, eager to spread the warmth and find equilibrium. It's like the party-goers seeking out cooler spots to cool off after an energetic dance. This flow of heat from hot to cold regions is the essence of heat transfer, a phenomenon that shapes our daily experiences, from feeling the warmth of sunlight to savoring a hot cup of cocoa on a chilly day.

1.3.2 History of thermoelectric phenomenon

Alessandro Volta, an Italian physicist, was the first to identify the thermoelectric phenomenon's fundamental component—the temperature difference—in 1794. He discovered that if there was a temperature difference between the ends of an iron rod, it could cause a frog's leg to spasm. Later, in 1821, Seebeck independently rediscovers it, and the effect now carries his name.

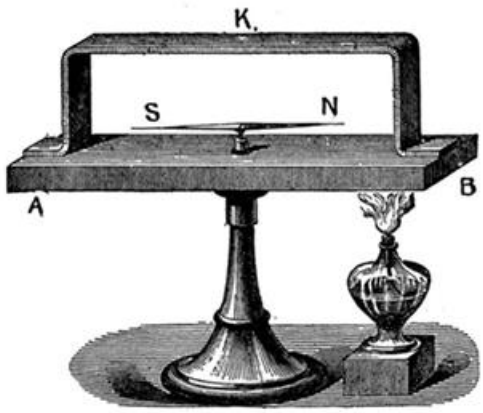

Fig 1.4 A schematic of the original setup used by Thomas Seebeck. A and B are the two junctions, one of block of bismuth and a U- strip of copper (K). The compass needle shows deflection when heated at one end.

Today Although Tallinn is the capital of Estonia, in the 17th century it was governed by the Tsarist Russian Empire. When it was Reval, Thomas Johann Seebeck was born there into a Baltic-German family. He had a medical degree, but he really liked science. In attempt to

comprehend Ørsted's discoveries, he experimented with voltaic current and magnets and discovered something unusual. He discovered that a magnetic needle deflects when a circuit comprised of two different metals with connections at different temperatures is present. Seebeck thought that the temperature differential was what caused the magnetic. He therefore referred to the phenomenon as the "thermomagnetic effect" because he was not aware that electric current was involved. in the 1820s, the perplexing relationship between electricity and magnetism was the subject of a tangle of theories and explanations among the scientific community. Imagine that there were some who sought links between various forces like electricity, magnetism, heat, light, and even chemical processes on one side and those who believed in nature's enigmatic polarity. The illustrious André-Marie Ampère and a group of French physicists led the disciples of the great Newton who adhered to his idea of force. German chemists and physicists, along with Ørsted, Seebeck, and Ritter, embarked on an investigation to learn more about this complex link. They probed the core of the issue in search of links that would unite electricity, magnetism, and heat into a mellow symphony of forces.

However, Ørsted saw a distinct perspective in Seebeck's experiment thanks to his great sense of potential. He perceived a subsurface connection between heat, electricity, and magnetism. He had no idea that he was about to learn a fascinating secret about how the Seebeck effect came to be.

It was rapidly understood that Seebeck's effect was an electric current that was created, which by Ampere's law deflected the magnet, after the discovery of the electron and its fundamental charge. To be more precise, a closed circuit's electric current can be driven by the electric potential (voltage) created by the temperature differential. The Peltier-Seebeck effect is the name given to this phenomenon nowadays. The field of thermoelectricity continues to astound us with its limitless potential and promising potential for a greener and more exciting future. It was formed from the enthusiasm and curiosity of great minds.

1.3.3 The Seebeck effect

The Seebeck effect can be used to capture leftover heat, higher temperatures brought on by global warming, etc. In essence, this effect can be used to create thermoelectric generators, which operate similarly to heat engines but are less bulky, have no moving parts, and currently have a

slightly higher cost and lower efficiency. However, these characteristics are expected to improve as we continue to research various materials that can be used for this purpose.

The Seebeck effect is the electromotive force (emf) that arises when there is a temperature differential between two points of an electrically conducting material. The emf is also known as a thermoelectric, thermoemf, or Seebeck emf. The Seebeck coefficient is the product of the emf and temperature differential. Generally speaking, the local generation of an electromotive field describes the Seebeck effect,

$$E_{emf} = -S\nabla T \quad (1)$$

Here S is the Seebeck coefficient and ∇T the temperature gradient. The local current density here is given by,

$$J = \sigma(-\nabla V + E_{emf}) \quad (2)$$

Where is the local conductivity and V is the local voltage. The Seebeck coefficients change with temperature and are highly affected by the conductor's composition. At ambient temperature, for common materials, the Seebeck coefficient may range in value from −100 μV/K to +1,000 μV/K. If the system enters a steady state with J=0, the voltage gradient is simply provided by the emf:

$$\nabla V = -S\nabla T \quad (3)$$

The simple relationship, that does not depend on conductivity, is broadly used in the thermocouple to measure a temperature difference; a complete temperature may be found by executing the voltage measurement at a known reference temperature.

Thermocouples in series form a thermopile, that is an electronic device that converts thermal energy into electrical energy.

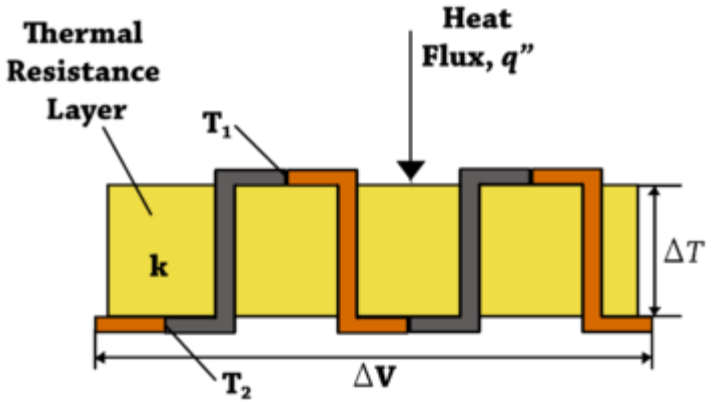

Fig 1.5 Schematic of a differential temperature thermopile

1.3.3.1 Sign Convention of Seebeck Effect

$$S = -\frac{V_{left} - V_{right}}{T_{left} - T_{right}} \quad (4)$$

Therefore, if S is positive, the end with the lower voltage and vice versa has the higher temperature. The voltage gradient in the material will point against the temperature gradient. The Seebeck effect is generally controlled by the contribution from charge carrier diffusion. which is prone to push charge carriers towards the cold side of the material until a recompensating voltage has built up.

Thus, in p-type semiconductors (which have only positive mobile charges, electron holes), S is positive. In the same way, in n-type semiconductors (which have only negative mobile charges, electrons), S is negative.

In most of the conductors, however, the charge bearers reveal both hole-like and electron-like behavior and the sign of S mainly depends on which of them prevails.

1.3.3.2 Physical factors that determine the Seebeck coefficient

The temperature, crystal structure and impurities of the material affect the value of thermoelectric coefficients. The Seebeck effect can be assigned to two things: [12] diffusion of charge carriers and phonon resistance. At a basic level, the voltage difference indicates the difference in thermodynamic chemical potential of the charge carriers, and the direction of flow under the voltage difference is fixed by the universal thermodynamic process in which (at the same temperature) particles flow upward. from chemical potential to low chemical potential.

1.3.3.3 Diffusion of charge carrier

Charge carriers (such as thermally excited electrons) are continually diffusing in a conducting material. Due to temperature variation, some of these charge carriers move with higher-than-average energy and some with lower energy. When no voltage or temperature differences are put in , carrier diffusion balances perfectly and thus no average current is seen: $J=0$.

A net current can be brought about by applying a voltage difference (Ohm's law), or by appealing a temperature difference (Seebeck effect). To understand the microscopic origin of the thermoelectric effect, it is generally better to first narrate the microscopic mechanism of the normal Ohm's law electrical conductance—to understand what determines the σ in $J=-\sigma\nabla V$.

From a microscopic point of view, what's happening in Ohm's law is that the higher the energy level, the higher gathering of the number of carriers per state on the side with the higher the chemical potential. For every interval of energy, carriers tend to disperse and spread into the part of the device where there are less carriers per state of this energy. However, as carriers move, they sometimes scatter dissipatively. Disperse means that they re-randomize their energy based on the local temperature and the local chemical potential. Disperse also removes carriers from those higher energy states, leaving more carriers to diffuse in. A combination of diffusion and disorientation leads to an overall drift of charge carriers towards the part of the material with the lower chemical potential.

Now let's look at a case where there's a temperature gradient with uniform voltage and uniform chemical potential. At the hotter end of the material, there's more variation in charge carriers' energies than at the colder end. High energy levels have higher carriers occupied per state at the hotter end, but the hotter side also has a lower carrier occupied per state at a lower energy level. As we saw above, high energy carriers drift away from the hotter end, causing entropy by drifting toward the cold end. At the same time, low energy carriers drift back toward the hot end. Both of these processes generate entropy, but they work in opposite directions from each other as far as charge current is concerned. Net current only occurs when one drifts more than the other.

The net current is given by, $J=-\sigma S\nabla T$, the thermoelectric coefficient σS depends exactly on how conductive high-energy carriers are, as compared to low-energy carriers. The difference may

be due to a contrast in rate of scattering, a dissimilarity in speeds, a contrast in density of states, or a combination of these effects.

1.3.3.4 Mott Formula

The processes described above are applicable to materials in which each charge carrier encounters a virtually stationary environment, so that its movement can be described independently of other carriers, and independently of other dynamics (e.g., phonons). In electronic materials with weak interactions between electrons and photons, etc., it can be generally demonstrated that the linear response conductor is,

$$\sigma = \int c(E)(-\frac{df(E)}{dE})dE, \tag{5}$$

and the linear response thermoelectric coefficient is,

$$\sigma S = \frac{k_B}{-e}\int \frac{E-\mu}{k_B T} c(E)\,(-\frac{df(E)}{dE})dE \tag{6}$$

where *c(E)* represents energy-dependent conductivity and f(E) represents the Fermi-Dirac distribution function. These equations are known as Sir Nevill Francis Mott's Mott relations. [14] The resultant,

$$-\frac{df(E)}{dE} = \frac{1}{4k_B T} sech^2(\frac{E-\mu}{2k_B T}) \tag{7}$$

is a function maxed around the chemical potential or Fermi level μ with a breadth of approximately $3.5k_B T$. The energy-dependent conductivity (a parameter that cannot be directly measured – only σ is measured) is computed as,

$$c(E) = e^2 D(E) v(E) \tag{8}$$

Where *D(E)* is the electron diffusion constant and *v(E)* is the electronic density of states (both parameters are generally functions of energy).

In strong-interacting materials, none of these equations can be applied because each charge carrier cannot be thought of as a self-consolidating entity.

Wiedemann-Franz can also be derived exactly using the free electron picture. For example, in superconductors, the Mott relation also tends to fail. [15]

According to the Wiedemann-Franz law, the ratio of a metal's electronic contribution to thermal conductivity (κ) to electrical conductivity (σ) is proportional to temperature (T),

$$\frac{\kappa}{\sigma} = LT, \tag{9}$$

Where the proportionality constant L, often known as the Lorentz number, is theoretically equal to $2.44 \times 10^{-8}\ V^2K^{-2}$. This empirical law was given its name after Gustav Wiedemann & Rudolph Franz, who found in 1853 that $\frac{\kappa}{\sigma}$ had about the same value for various metals at identical temperatures.[16] The κ/σ proportionality with temperature was discovered in 1872 by Ludvig Lorenz.

Whenever the semiconductor is slightly doped, the Seebeck coefficient is maximum; nevertheless, an elevated Seebeck coefficient is occasionally beneficial on its own. It is more necessary to improve the thermoelectric power factor σS^2 for thermoelectric power equipment (coolers, generators etc.) or the thermoelectric figure of merit, whose optimization commonly found at high levels of doping.

1.3.3.5 Phonon Drag

Phonons (also called quantized lattice vibration wave or QLVs) are a central thermal carrier that contribute to thermal capacity (sustainable heat storage), conductive heat transfer, and thermal conversion in condensed phase.

Phonon drag is the increase in conduction electron or valence hole mass due to interactions in the crystal lattice where the electron is moving. Phonons do not always travel in local thermal equilibrium. They travel against the thermal gradient and lose momentum due to interactions with electrons (or carriers) and defects in the crystal.

When the interaction between electrons and phonons is dominant, the phonons tend to push electrons to one side of the material and lose momentum, resulting in a thermoelectric contribution. This contribution is greatest in the thermal region where the interaction between phonons and electrons is dominant. This happens when,

$$T \approx \frac{1}{5}\theta_D \tag{10}$$

Where θ_D is the Debye temperature. What is Debye temperature? Debye temperature is the temperature at which a solid's vibrational modes (in particular its phonon modes) become fully excited and significantly contribute to the solid's heat capacity. At temperatures much below Debye, only a small number of low-energy vibrational modes are excited. The heat capacity of a material at this temperature is relatively low. As the temperature rises and approaches Debye temperature, the number of phonon modes that are excited increases, resulting in an increase in heat capacity. What determines the Debye temperature of a material? The temperature at which a material's phonon modes become fully excited is determined by a number of factors, including the crystal structure of the material, lattice constants and the atomic masses of the materials.

Less phonons are available for drag at lower temperatures. At higher temperatures, the phonons lose momentum in the phase-phonon scattering (P- scattering) instead of the phase-electron scattering (PES). At lower temperatures, the material boundaries also increase as the phonons travel large distances.[18]

Phonon drag is a significant effect in semiconductors at ambient temperatures (however its well above $\theta/_5$) and in reality, the size of this impact is comparable to the carrier-diffusion effect discussed in the preceding section. Under a magnetic field, this section of the thermopower-versus-temperature curve is very changeable.

1.3.3.6 Seebeck coefficient and entropy

The Seebeck coefficient of a substance relates thermodynamically to the quantity of entropy "dragged along" by the movement of charge inside a material; it is the entropy per unit charge in the substance in certain ways [19]. The Seebeck coefficient represents the amount of entropy that particles may transport without the assistance of the temperature gradient. [20]

1.3.3.7 Seebeck coefficients for some common materials

Seebeck coefficients at ambient temperature for several typical, non-exotic materials, evaluated in relation to platinum, are shown in the table below [21]. The Seebeck coefficient of platinum is around −5 μV/K at ambient temperatures,[22] and so the results enlisted here below is adjusted accordingly. For e.g., the Seebeck coefficients of Ag, Cu, Au is around 1.5 μV/K, and of

Al is −1.5 μV/K. The semiconductor Seebeck coefficient is highly dependent on doping, with usually values that are positive for p doped substances and a negative value for n doped materials.

Material	**Seebeck coefficient relative to platinum (μV/K)**
Selenium	900
Tellurium	500
Silicon	440
Germanium	330
Antimony	47
Nichrome	25
Iron	19
Molybdenum	10
Cadmium, tungsten	7.5
Gold, silver, copper	6.5
Rhodium	6.0
Tantalum	4.5
Lead	4.0
Aluminum	3.5
Carbon	3.0
Mercury	0.6
Platinum	0 (definition)
Sodium	-2.0
Potassium	-9.0
Nickel	-15
Constantan	-35
Bismuth	-72

1.3.4 Peltier effect

If an electric current is sent through a thermocouple circuit, heat is created at one of the junctions and absorbed at the other. The presence of cooling or heating at the electrified junction between two distinct conductors is known as the Peltier effect. The effect is named after Jean Charles Athanase Peltier, a French scientist who discovered it in 1834 [23]. When a current is sent across a junction between the two conductors, both A and B, heat can be created or dissipated at the junction. The Peltier heat created at the intersection per unit time equals,

$$\dot{Q} = (\Pi_A - \Pi_B)I \tag{11}$$

Where Π_A and Π_B are called the Peltier coefficients for the conductors mentioned, both A and B. The electric current (from A to B) is designated as *I*. The amount of heat produced is not dictated just by the Peltier effect, but also by the Joule heating and temperature gradient effects.

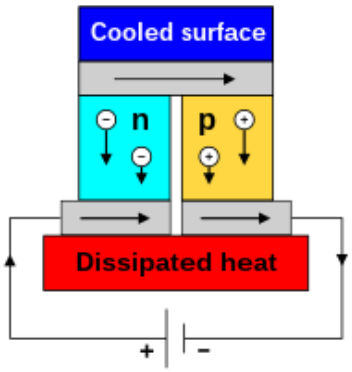

Fig 1.6 The Seebeck circuit configured as thermoelectric cooler

Peltier coefficients reflect the amount of heat transported per unit charge. Because charge current needs to be uninterrupted across the junction, the related heat flow will create a discontinuity if this condition is not met, that is Π_A *and* Π_B are different. The Peltier effect is the back-action equivalent to the Seebeck effect (which is comparable to that of back-EMF in magnetic induction): if an ordinary thermoelectric circuit is closed down, the Seebeck effect will produce a current, which will continually move heat from the hot to the cold junction (via the Peltier effect). The straight correlation between their coefficients demonstrates the close association between the Peltier & Seebeck effects: $\Pi = T$. Peltier heat pumps are typically made up

of a number of series of junctions, through which a flow of heat is generated. Some of these junctions lose heat as a result of the Peltier effect, but some of them also gain heat. A thermoelectric heat pump takes advantage of this, as do thermo-cooling devices such as those used in refrigerators.

1.3.5 Thomson Effect

The Seebeck coefficient does not stay constant in different materials. A spatial temperature gradient can cause the Seebeck coefficient to change. If a current passes through this gradient, a continuous version of Peltier's Peltier effect occurs. This continuous version of the Seebeck effect is called the Thomson effect. Lord Kelvin predicted the Thomson effect in 1851, and William Thomson observed it in 1851. [24]

When a current passes through an uneven heated conductor, it evolves or absorbs heat along its length, depending on how the current flows. This phenomenon is called the Thomson effect. This effect is, however, reversible.

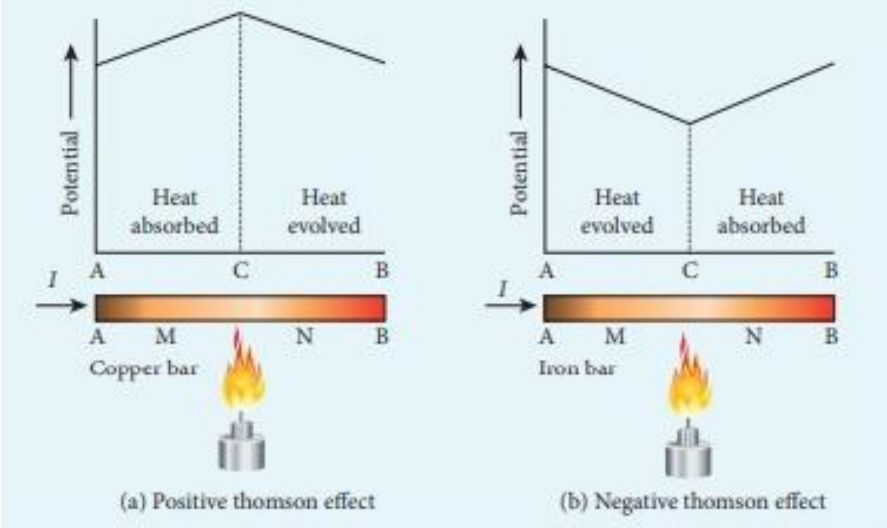

Fig 1.7 (a, b) Positive and Negative Thomson effect.

Let us consider a thick copper bar AB whose is both ends are maintained at the same temperature and the center is maintained at a higher temperature. When current flows through the bar from end A and B, then it is found that the heat is absorbed at end A and is evolved at the end

B (Fig1.6 a). Thus, there is a transfer of heat due to the current in the direction of the current. This is called the positive Thomson effect. The other elements showing a positive Thomson effect are Cd, Zn, Ag, and Sb.

Let's take an example of a thick copper bar AB, where both ends of the bar AB are maintained at constant temperature and the center of the bar AB is maintained at constant temperature. When there is a flow of current through the bar AB from ends A and B, it is observed that the heat at end A is absorbed and the heat evolves at end B (Fig.1.6a). Hence, there is a heat transfer due to the direction of current. This is known as positive Thomson effect. Other elements showing positive Thomson effect are: Cd, Zn, Ag, Sb.

Let's now look at the case of an Iron bar under the same conditions. When the current flows in the bar from A through B, heat evolves at A and heat absorbs at B (see Fig.1.6b). Hence, there is heat transfer due to the current flow and it takes place in opposite direction to that of the current flow. This is known as negative Thomson effect (see Fig.1.6b). The other elements that exhibit a negative Thompson effect are Fe (Fe), Co (Co), Ni (Ni), Pi (Pi), and Hg (Hg). Lead exhibits no Thomson effect.

The Thomson effect describes the warming or cooling of the current carrying conductor with a gradient of temperature. If the current density J passes through a homogenous conductor, the Thompson effect predicts the heat production per unit volume.

$$\dot{q} = -\mathcal{K}\mathrm{J} \cdot \nabla\mathrm{T} \qquad (12)$$

Where ∇T is the thermal gradient and K is given as the Thomson coefficient. Thomson coefficient can be stated as the amount of energy absorbed or produced when a unit current flows for 1 second between two different points in any conductor which differs in temperature by a kelvin (1K). The Thomson coefficient is connected to the Seebeck coefficient as $K = T\frac{dS}{dT}$. In this equation, however, Joule heating and general thermal conductivity is neglected.

The reason for this is that the difference in temperature between two points on the same conductor gives rise to a difference in electron density. At low temperatures, the electron density is greater than at high temperatures. Therefore, a potential difference exists between two points on a connector. When a current flows in a conductor, work along or against the direction of that

potential difference is done. This heat is either absorbed or developed. The difference between the number of absorbed and developed energies is what gives rise to the Thomson effect (see Seebeck coefficient below).

The origin of the Thompson effect is very similar to the one of Peltier. This is because Lord Kelvin discovered the relationships between these three coefficients in 1854. This means that the three effects are manifestations of the same effect (see Seebeck coefficient below).. [25]

The first relation is given as, [26]

$$K \equiv \frac{d\Pi}{dT} \tag{13}$$

Where T is the absolute temperature in terms of Kelvin, K is the Thomson coefficient. Peltier coefficient is given as Π and S is the Seebeck coefficient.

The second relation is given by $\Pi = TS$. This relationship establishes a link between Peltier and the Seebeck Effect. This second Thomson relation is guaranteed only for time-reversal symmetric materials; if the material is put in a magnetic field or is magnetically structured (ferromagnetic, antiferromagnetic, etc.), the second Thomson relation does not assume the simple form given above. Instead, by using second relation, first Thomson relation becomes,

$$K = T\frac{dS}{dT}. \tag{14}$$

The Thomson coefficient is the only thermoelectric coefficient that can be directly measured for individual materials. Peltier and Seebeck can only be measured for pairs of materials, so it is hard to find absolute Seebeck and Peltier values for a specific material.

1.3.6. Nerst-Ettingshausen Effect

Named in honor of Walther Nernst, a notable German chemist, and Albert von Ettingshausen, a distinguished Austrian physicist, the Ettingshausen effect emerged during the tenure of Ettingshausen as a physics professor at Graz University of Technology. It was during this time that he collaborated with his doctoral student, Walther Nernst, in their investigation of the Hall effect and its manifestations in metallic substances.

The Hall effect, originally discovered by Edwin Hall in 1879, refers to the creation of an electrical potential difference, known as the Hall voltage, across a conductor. This voltage arises perpendicular to both the electric current flowing within the conductor and the externally applied magnetic field that is oriented at a right angle to the current.

While conducting studies on the Hall effect in bismuth, Ettingshausen and Nernst made a noteworthy observation: when one side of the bismuth sample was subjected to heating, an unexpected perpendicular flow of electrical current occurred. This phenomenon was subsequently termed the Nernst effect. Essentially, they identified a thermoelectric occurrence wherein an electrically conductive sample, exposed to a magnetic field and a perpendicular temperature gradient, would generate an electric field that is perpendicular to both the magnetic field and the temperature gradient.

This effect is quantified by the Nernst coefficient *v,* which is defined as

$$v = \frac{E_y}{B_z}\frac{1}{\partial_x T} \tag{15}$$

Where we have E_y which represents the y-component of the electric field generated by the z- component of the magnetic field B_z along with the x-component of the temperature gradient $\partial_x T$.

In contrast to this scenario, when an electric current is introduced (aligned with the y-axis) and combined with a magnetic field oriented perpendicularly (aligned with the z-axis), a distinct temperature gradient emerges along the x-axis. This phenomenon is referred to as the Ettingshausen effect. The presence of the Hall effect results in electrons being compelled to travel at right angles to the applied current direction. This electron movement discrepancy leads to an accumulation of electrons on one side of the specimen, subsequently causing an upsurge in collision occurrences and consequent heating of the material.

This phenomenon is quantified by means of the Ettingshausen coefficient, denoted as 'P', which is precisely defined as:

$$P = \frac{1}{|B_z| \cdot J_y} \frac{dT}{dx} \quad (16)$$

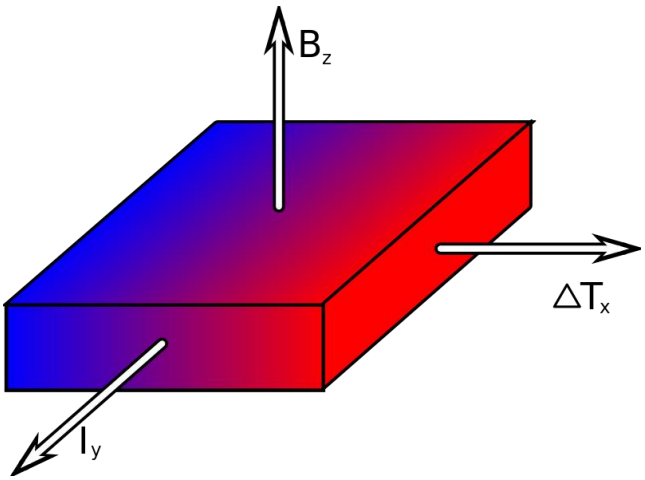

Fig 1.8 Temperature gradient due to Ettingshausen effect with applied magnetic field and electric current.

The temperature gradient, denoted as *dT/dx*, arises from the y-component (J_y) of electric current density (measured in A/m^2) and the z-component (B_z) of the magnetic field. In typical metals such as copper, silver, and gold, the P value is approximately 10^{-16} m·K/(T·A), making its detection challenging within usual magnetic fields. However, in the case of bismuth, the Ettingshausen coefficient exhibits significantly greater values due to its limited thermal conductivity. Specifically, for bismuth, the Ettingshausen coefficient is measured at (7.5±0.3) × 10^{-4} m·K/(T·A), differing by several orders of magnitude.

1.3.7 Thermoelectric Materials

While the thermoelectric effect exists in all materials to some extent, its practical utility is often limited by its minimal magnitude in most cases. Nevertheless, there is a focus on identifying cost-effective materials that exhibit a sufficiently robust thermoelectric effect, along with other requisite properties. These materials are being explored for various applications, such as power generation and refrigeration. A commonly utilized thermoelectric material is an alloy based on Bismuth Telluride, which is intentionally doped to create distinct 'N' and 'P' characteristics within individual blocks or elements. The production of thermoelectric materials is primarily

accomplished through either controlled crystallization from a molten state or compressed powder metallurgy techniques. Although each manufacturing approach has its own advantages, the directional crystallization method is the most prevalent. Beyond Bismuth Telluride (Bi2Te3), alternative thermoelectric materials include Lead Telluride (PbTe), Silicon Germanium (SiGe), and Bismuth-Antimony (Bi-Sb) alloys, which find specific utility in certain scenarios.

1.3.7.1 Thermoelectric figure of merit

The efficacy of a substance in thermoelectric setups is ascertained by its performance within the device. This performance is gauged by the material's electrical conductivity (σ), thermal conductivity (κ), and Seebeck coefficient (S), all of which undergo alterations with temperature (T). The utmost effectiveness of the energy conversion procedure, applicable to power generation and cooling alike, at a specific temperature junction within the material, is dictated by the thermoelectric material's figure of merit, denoted as zT. This value is formulated as follows:[27]

$$zT = \frac{\sigma S^2 T}{\kappa} \tag{17}$$

1.3.7.2 Device efficiency

The effectiveness of a thermoelectric apparatus in generating electricity is denoted as η.

$$\eta = \frac{\text{energy provided to the load}}{\text{heat energy absorbed at the hot junction}} \tag{18}$$

This parameter is defined as the ratio of the energy delivered to the load to the thermal energy taken in at the hot junction. In the realm of thermoelectric devices, the upper limit of efficiency is commonly expressed using a metric called the device figure of merit, ZT. The highest attainable efficiency of a thermoelectric device can be approximately ascertained using the following expression:

$$\eta_{max} = \frac{T_H - T_C}{T_H} \frac{\sqrt{1+Z\overline{T}}-1}{\sqrt{1+Z\overline{T}}+\frac{T_C}{T_H}} \tag{19}$$

At the hot junction, a fixed temperature denoted as T_H is established, while at the cooled surface, another fixed temperature denoted as T_C is maintained. The average temperature, T, is determined as the mean of T_H and T_C. This equation for maximum efficiency remains accurate when thermoelectric properties exhibit no temperature dependence. When considering a single thermoelectric module, the efficiency of the device can be computed by utilizing the temperature-sensitive characteristics, namely, Seebeck coefficient (S), thermal conductivity (κ), and electrical conductivity (σ), in conjunction with the flow of heat and electric current through the material [28].

In the practical configuration of a thermoelectric device, two distinct materials are employed (typically, one n-type and one p-type), connected by metallic interconnects. The ultimate efficiency, η_{max}, is subsequently derived from the efficiencies of both thermoelectric modules, while also accounting for the electrical and thermal losses that arise due to the interconnects and the surrounding environment.

By disregarding these losses and assuming that the temperature dependencies of S, κ, and σ can be overlooked, a somewhat approximate estimation of the thermoelectric figure of merit (ZT) is provided:

$$Z\overline{T} = \frac{(S_p - S_n)^2 \overline{T}}{[(\rho_n \kappa_n)^{1/2} + (\rho_p \kappa_p)^{1/2}]^2} \tag{20}$$

In the context of electrical resistivity represented by ρ, the properties being discussed are averaged across a range of temperatures. The subscripts 'n' and 'p' are used to indicate properties associated with n-type and p-type semiconducting thermoelectric materials, respectively. The crucial condition for the following statements is that the n-type and p-type elements exhibit identical properties that remain consistent regardless of temperature.

$$(S_p = -S_n) \text{ does } Z\overline{T} = z\overline{T}. \tag{21}$$

As thermoelectric devices are also heat engines, their efficiency is constrained by the Carnot efficiency. $\frac{T_H - T_C}{T_H}$The first factor in η_{max} is $\frac{T_H - T_C}{T_H}$, while ZT and zT are indicators that establish the upper limits of thermodynamic process reversibility on a global and local scale, respectively. Nevertheless, the coefficient of performance exhibited by contemporary

thermoelectric refrigerators available in the market spans from 0.3 to 0.6. This range is one-sixth of the coefficient of performance found in traditional vapor-compression refrigerators [29].

1.3.7.3 Power Factor

Generally, the thermoelectric power factor for a thermoelectric material, is given by ,

$$Power\ Factor = \sigma S^2 \left[\frac{\frac{W}{m}}{K^2}\right]. \quad (22)$$

Where the Seebeck coefficient, denoted as 'S,' and the electrical conductivity, symbolized by 'σ,' hold pivotal roles. While there is a common assertion that thermoelectric (TE) devices incorporating materials possessing a higher power factor can ostensibly 'generate' more energy—essentially facilitating a more efficient transfer of heat or extraction of energy from temperature differentials—this proposition exclusively holds true under the premise of an unchanging device geometry and unrestricted heat source and cooling mechanisms. However, when we shift our focus to a more realistic scenario where the device geometry is meticulously tailored to the specific application at hand, the behavior of thermoelectric materials is primed to operate at peak efficiency. This pinnacle of efficiency is governed not by the product of electrical conductivity σ and the square of Seebeck coefficient S^2 that is σS^2, but rather by a dimensionless figure of merit known as zT.

1.3.7.4 Factors for Materials Choice

For optimal efficiency, it is necessary to employ materials that possess high electrical conductivity, low thermal conductivity, and a high Seebeck coefficient. When considering the thermal conductivity (κ) in crystalline solids, it comprises two primary components: $\kappa_{electron}$ and κ_{phonon}. As indicated by the Wiedemann-Franz law, heightened electrical conductivity leads to an increase in κ electron. As a result, in metals, the thermal-to-electrical conductivity ratio remains relatively constant due to the predominant contribution from electrons. However, in semiconductors, the role of phonons, which are vibrations in the crystal lattice, becomes crucial and cannot be dismissed. The presence of phonons impacts efficiency adversely.

To attain optimal efficiency, it is imperative to achieve a low ratio of κ_{phonon} to $\kappa_{electron}$, i.e. $\kappa_{phonon} / \kappa_{electron}$. When examining the band structure of materials, semiconductors exhibit more favorable thermoelectric effects compared to metals. This distinction arises from the positioning of the Fermi energy concerning the conduction band. In semiconductors, the Fermi energy lies below the conduction band, leading to an asymmetric state density distribution around this energy level. Consequently, the average electron energy in the conduction band surpasses the Fermi energy, creating a favorable environment for charge movement toward a lower energy state.

Metals on other hand, have their Fermi energy situated within the conduction band. This arrangement results in a symmetric state density distribution around the Fermi energy, causing the average energy of conduction electrons to align closely with the Fermi energy. Consequently, the driving forces for charge transport are diminished. This divergence underscores the superior potential of semiconductors as ideal candidates for thermoelectric materials, mainly due to their band structure and resulting charge dynamics.

1.3.7.5 Promising Material Categories

Enhancing the efficiency of thermoelectric performance involves two primary strategies: advancements in bulk materials and the utilization of low-dimensional systems. The pursuit of methods to decrease lattice thermal conductivity can be categorized into three fundamental material classifications:

a) Alloy Enhancement: This method involves the manipulation of point defects, vacancies, or oscillating structures (involving heavy-ion species exhibiting substantial vibrational amplitudes within partially occupied structural sites). This manipulation effectively scatters phonons within the crystal's unit cell. [31]

b) Complex Crystal Engineering: The concept here is to segregate the phonon "glass" from the electron "crystal" by adopting techniques analogous to those used in superconductors. In this approach, the electron transport zone is structured as a high-mobility semiconductor, constituting an electron crystal. Meanwhile, the phonon glass, meant to accommodate

disordered structures and dopants, remains separate without disrupting the electron crystal, much like the role of a charge reservoir in high-Tc superconductors. [32]

c) Multiphase Nanocomposites: This approach centers around scattering phonons at interfaces within nanostructured materials. These interfaces can exist in the form of mixed composites or thin film superlattices. [33]

1.3.8 Applications of Thermoelectric effect

The thermoelectric effect, which converts temperature differences into electric voltage, finds a myriad of applications spanning various industries. From propelling spacecraft to powering energy-efficient devices, the thermoelectric effect has showcased its value across diverse realms. Below is an exhaustive list of applications, shedding light on their significance and influence:

- Thermoelectric Generators (TEGs): TEGs represent devices directly transforming heat differentials into electricity. Their applications encompass:
- Space Exploration: TEGs empower spacecraft and satellites by exploiting temperature disparities between their sunlit and shaded facets.
- Remote Power Generation: TEGs capture residual heat from industrial processes, geothermal reservoirs, and exhaust gases to engender electricity.
- Automotive Sector: TEGs seize waste heat from vehicle engines and exhaust systems, augmenting fuel efficiency and curtailing emissions.
- Industrial Operations: Thermoelectric modules recover dissipated heat from furnaces, power plants, and other industrial operations.
- Body Heat-Powered Devices: Thermoelectric constituents are amalgamated into wearable gadgets, fueling sensors and diminutive electronics via bodily warmth.
- Implantable Devices: Thermoelectric materials serve as energy sources for medical implants, such as pacemakers and sensors, employing the temperature variance between the body and ambient surroundings.
- On-the-Go Charging: Thermoelectric charging cases exploit heat origins like warm beverages to replenish smartphones and other portable contrivances.

- HVAC Systems: Thermoelectric modules optimize heating, ventilation, and air conditioning (HVAC) systems, capturing and utilizing residual heat or cooling effects.
- Remote Sensors: Military establishments employ thermoelectric sensors energized by ambient temperature fluctuations to detect breaches or surveil pivotal zones.
- Fitness Apparatus: Wearable fitness trackers can harness bodily temperature fluctuations during exertion to invigorate their sensors and tracking mechanisms.
- Targeted Cooling: Thermoelectric coolers are employed to cool distinct components in electronics, assuring optimal operation and protracted longevity.
- Geothermal Energy: Thermoelectric systems harness heat from the Earth's interior to fabricate electricity within geothermal power plants.
- Remote Weather Stations: Thermoelectric sensors fuel remote weather stations, facilitating precise data accumulation amidst inclement conditions.
- Aircraft Components: Thermoelectric materials regulate temperatures in aircraft components, augmenting efficiency and efficacy.

1.4 Perovskites

Perovskite stands as a mineral comprised of calcium titanate ($CaTiO_3$). Its initial discovery took place within Russia's Ural Mountains, courtesy of Gustav Rose. This mineral gained its moniker from Lev Perovski, a Russian Mineralogist. The captivating intricacies of its structure were initially unveiled by Victor Goldschmidt in 1926 through his exploration of tolerance factors. The structural blueprint was subsequently unveiled in 1945 through the examination of barium titanate via X-Ray diffraction techniques. This pioneering work was accomplished by Helen Dick Megaw, an Irish luminary in the field of X-Ray crystallography.

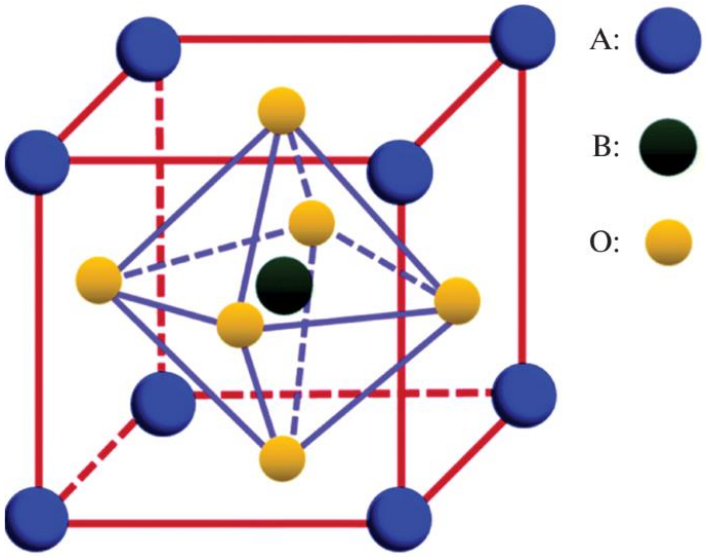

Fig 1.9 General structure of Perovskite

Broadly speaking, perovskite serves as an umbrella term for materials embodying a crystal arrangement adhering to the ABX_3 formula. Here, 'A' and 'B' denote two positively charged ions, typically differing in size, while 'X' signifies a negatively charged ion or an anion that establishes bonds with both cations. Notably, 'A' entities are characteristically larger than their 'B' counterparts. Within the ideal cubic configuration, the 'B' cation is encompassed by an octahedron of anions, demonstrating a 6-fold coordination, whereas the 'A' cation resides within 12-fold cuboctahedra coordination.

Furthermore, variants of the perovskite structure may manifest, encompassing scenarios where either or both the 'A' and 'B' sites adopt an arrangement akin to $A1_{x-1}A2_x$ and/or $B1_{y-1}B2_y$. Additionally, deviations from the standard coordination arrangement can occur within the 'X' anions, driven by shifts in the oxidation states of the ions within the 'A' and 'B' sites [5].

Perovskite structure has found particular relevance in the realm of photovoltaics. Perovskite solar cells have surged into the limelight owing to their impressive power conversion efficiencies and ease of fabrication. Their unique optoelectronic properties, stemming from the interplay of 'A', 'B', and 'X' constituents, make them promising candidates for next-generation solar energy conversion technologies [34].

Beyond photovoltaics, perovskites exhibit catalytic activity, electronic conductivity, and superconductivity, showcasing their multifaceted utility. Additionally, perovskite-related research is shedding light on emergent phenomena like multiferroicity and magnetoelectric coupling, where the intricate interplay between 'A', 'B', and 'X' components gives rise to unique material behaviors [35].

Perovskites are widely abundant in nature, boasting a structure that pervades an extensive array of compounds. This versatility yields diverse properties and applications, contributing to their remarkable prevalence and significance.

Perovskite materials have become a captivating focus of research, sparking growing interest within the scientific community, especially in the realm of thermoelectricity. These fascinating materials, with their unique properties and diverse applications, hold the promise of revolutionizing thermoelectric technology.

1.4.1 Structure

The perovskite crystal structure is a distinctive arrangement of atoms that follows the general formula ABX3, where 'A' and 'B' are cations and 'X' is an anion. This structure was first identified in the mineral perovskite, which is composed of calcium titanate (CaTiO3). The perovskite structure has become a fundamental framework for various materials with diverse properties and applications. Here's a detailed description of the perovskite crystal structure:

1.4.1.1 Crystallographic Arrangement:

The perovskite crystal structure is cubic and belongs to the space group Pm-3m (No. 221) in the International Tables for Crystallography. In its ideal form, the structure consists of a three-dimensional network of corner-sharing octahedra and cuboctahedra.

1.4.1.2 Unit Cell:

The perovskite unit cell contains one 'A' cation at the center, surrounded by twelve 'X' anions forming a cuboctahedron. Additionally, there are six 'B' cations situated at the vertices of the octahedra surrounding each 'X' anion.

1.4.1.3 Coordination Polyhedra:

'A' Site: The 'A' cations occupy large cavities formed by the coordination of twelve 'X' anions. This arrangement results in a coordination number of 12 for the 'A' site cation. 'B' Site: The 'B' cations are located at the vertices of octahedra, each of which is shared with six neighboring 'X' anions. The coordination number of the 'B' site cation is 6. 'X' Site: The 'X' anions are positioned at the center of each of the faces of the cube, forming a distorted octahedral coordination environment.

1.4.1.4 Tolerance Factor:

The ratio of the radii of the 'A' and 'B' cations (r_A and r_B) to the radius of the 'X' anion (r_X) is known as the tolerance factor (t). The tolerance factor plays a crucial role in determining whether a given combination of 'A', 'B', and 'X' elements will yield a stable perovskite structure. The ideal tolerance factor for stability is around 1.

1.4.1.5 Variations and Distortions:

Real perovskite structures often deviate from the ideal cubic arrangement due to factors such as ionic size mismatches and electronic interactions. These deviations lead to various distortions, such as tilting of octahedra, rotations of octahedra, and displacements of 'A' and 'B' cations. These structural variations contribute to the diverse properties observed in perovskite materials.

1.4.1.6 Doping and Substitution:

The flexibility of the perovskite structure allows for the substitution of different cations at the 'A' and 'B' sites. This doping and substitution can be used to tailor properties such as electronic conductivity, dielectric behavior, and more.

The perovskite crystal structure serves as a foundation for a wide range of materials with distinct properties. While the ideal cubic arrangement is a hallmark, the ability to manipulate and modify this structure has enabled the design of perovskite-based materials for applications across electronics, energy, catalysis, and more.

1.4.2 Types of Perovskites

Perovskites exhibit a diverse array of types and compositions, each characterized by variations in the 'A' and 'B' cations as well as the anionic 'X' species. These distinct configurations give rise to a multitude of perovskite categories with unique properties and applications. Some prominent types of perovskites include:

- Oxide Perovskites: These are the traditional perovskite materials and are often oxides. They adhere to the general ABX_3 structure. Well-known examples include calcium titanate ($CaTiO_3$) and strontium titanate ($SrTiO_3$). These materials have been extensively studied due to their interesting electronic, magnetic, and optical properties.

- Ferroelectric Perovskites: Certain perovskite materials exhibit ferroelectric properties, characterized by the ability to switch their electric polarization under an external electric field. Lead zirconate titanate ($Pb(ZrTi)O_3$ or PZT) is a widely studied ferroelectric perovskite used in actuators, sensors, and memory devices.

- High-Temperature Superconducting Perovskites: Some perovskite materials exhibit superconducting behavior at relatively high temperatures. Yttrium barium copper oxide ($YBa_2Cu_3O_7$ or YBCO) is a well-known high-temperature superconducting perovskite that has been extensively researched for its potential applications in power transmission and medical imaging.

- Multiferroic Perovskites: Multiferroic materials exhibit both ferroelectric and magnetic properties. Bismuth ferrite ($BiFeO_3$) is a notable multiferroic perovskite, exhibiting spontaneous magnetization and ferroelectric polarization simultaneously. Such materials are of interest for novel electronic and spintronic devices.

- Organic-Inorganic Hybrid Perovskites: These materials combine organic and inorganic components to form unique perovskite structures. Organic-inorganic hybrid perovskites, such as methylammonium lead iodide ($CH_3NH_3PbI_3$), have gained significant attention in the field of photovoltaics due to their remarkable efficiency in solar cell applications.

- Double Perovskites: Double perovskites have an extended ABX_6 formula, where 'A' and 'B' are two different cations, often with different valence states. Strontium iron oxide nitride (Sr_2FeMoO_6N) is an example of a double perovskite with potential applications in spintronics and magneto-optics.

- Mixed-Anion Perovskites: These perovskites contain a mixture of different anions ('X' species) in the structure. For instance, calcium scandium oxide fluoride (CaScO2F) is a mixed-anion perovskite with interesting dielectric properties.

- A-Site Deficient Perovskites: In these perovskites, the 'A' cation site is intentionally left vacant, leading to unique properties such as enhanced oxygen transport. $La_{0.6}Sr_{0.4}Co_{0.2}Fe_{0.8}O_3$-δ (LSCF) is an example used in solid oxide fuel cells.

- High Entropy Perovskite Oxides: A recent addition to the perovskite family, high entropy perovskite oxides involve multiple cations at the 'A' or 'B' sites, offering enhanced tunability and novel properties for applications in catalysis, energy storage, and more. For instance, a representative HEPO could be a compound formulated as $(La_{0.2}Sr_{0.2}Ba_{0.2}Ca_{0.2}Na_{0.2})CoO3$. In this composition, a mix of lanthanum (La), strontium (Sr), barium (Ba), calcium (Ca), and sodium (Na) cations populate the 'A' site, offering a wide range of valence states and ionic radii. Similarly, cobalt (Co) cations occupy the 'B' site. This intricate mixture of cations creates a highly versatile lattice structure with enhanced tunability.

These are just a few examples of the diverse range of perovskite types. The manipulation of 'A', 'B', and 'X' components and their compositions allows researchers to tailor the properties of perovskite materials for specific applications across various scientific and technological domains.

1.4.3 Various Synthesis Techniques for Perovskites

- Solid-State Reaction (Ceramic Method): This classic method involves mixing stoichiometric amounts of precursor oxides, carbonates, or nitrates of 'A' and 'B' cations and the anion 'X'. The mixture is then calcined at high temperatures to form the perovskite phase. This technique is widely used due to its simplicity, but it can require high temperatures and long reaction times.

- Sol-Gel Method: In this technique, metal alkoxides or salts are dissolved in a solvent to form a solution (sol). Controlled hydrolysis and condensation reactions lead to the formation of a gel, which is then heated to obtain the perovskite phase. Sol-gel methods offer better control over composition and homogeneity.

- Hydrothermal/Solvothermal Synthesis: This method involves using a high-pressure, high-temperature aqueous solution to promote the crystallization of perovskites. It allows for the synthesis of well-defined and finely-tuned perovskite particles in a relatively short time.

- Mechanical Activation or High-Energy Ball Milling: Mechanical activation involves milling the precursor powders in a high-energy ball mill. The mechanical forces induce chemical reactions and phase transformations, resulting in the formation of perovskite structures at lower temperatures and shorter times.

- Pulsed Laser Deposition (PLD): PLD involves using a laser to ablate a target material, creating a plasma plume that deposits material onto a substrate to form thin films. While PLD is not a conventional method for perovskite synthesis, it has been explored for growing thin films of complex perovskite-related materials.

- Chemical Vapor Deposition (CVD): CVD techniques involve the reaction of vapor-phase precursors on a substrate to deposit thin films. In perovskite synthesis, this method is used to create thin films with precise control over composition and structure.

- Spray Pyrolysis: In this method, a precursor solution is sprayed onto a heated substrate, leading to the formation of a perovskite film. The technique offers scalability and control over film thickness.

- Template-Assisted Methods: These methods involve using templates, such as self-assembled monolayers or nanoporous substrates, to guide the growth of perovskite films with enhanced properties.

1.4.4 Properties of Perovskites

Perovskite materials exhibit a diverse array of physical and chemical properties that stem from their unique crystal structure and composition. Here are some of the key physical and chemical properties of perovskite materials:

1.4.4.1 Physical Properties:

- Crystal Structure: Perovskite materials adopt the distinctive ABX3 crystal structure, where 'A' and 'B' are cations and 'X' is an anion. This structure leads to a range of properties due to the arrangement of these components.

- Lattice Distortion: The distortion of the perovskite lattice can lead to variations in properties such as ferroelectricity and ferromagnetism. The tolerance factor, which measures the degree of distortion, affects the stability of the perovskite structure.

- Ionic Radii: The size of 'A' and 'B' cations and 'X' anions influences the stability and properties of perovskite materials. Mismatches in ionic radii can lead to lattice distortions and modifications in electronic and magnetic properties.

- Crystal Symmetry: Perovskite structures exhibit different symmetries depending on the arrangement of cations and anions, which can impact properties like ferroelectricity and piezoelectricity.

- Optical Absorption: Some perovskites have remarkable light absorption capabilities, making them suitable for photovoltaic applications. The energy bandgap can be tuned by varying the composition, enabling absorption of specific wavelengths of light.

- Magnetic Properties: Perovskites can display a variety of magnetic behaviors, including paramagnetism, ferromagnetism, antiferromagnetism, and more complex magnetic orders. The presence of transition metal ions in the 'B' site contributes to magnetic properties.

1.4.4.2 Chemical Properties:

- Chemical Stability: Perovskites can exhibit varying degrees of chemical stability, depending on the composition and environmental conditions. Some perovskites are sensitive to moisture and can undergo chemical degradation.

- Redox Properties: Transition metal ions in perovskite materials can undergo oxidation-reduction (redox) reactions, which contribute to their catalytic and electronic properties.

- Ionic Conductivity: Perovskites can possess high ionic conductivity, making them useful in applications like solid oxide fuel cells and oxygen sensors.

- Catalytic Activity: Some perovskites exhibit catalytic behavior due to their redox properties and surface chemistry. They can catalyze reactions in fields such as energy conversion and environmental remediation.

- Ion Diffusion: Perovskites' crystal structure allows for the diffusion of ions within the lattice, which is relevant for their behavior in solid-state batteries and fuel cells.

- Phase Transitions: Certain perovskites undergo phase transitions under specific conditions, leading to changes in properties such as ferroelectricity, ferromagnetism, and dielectric behavior.

- Thermal Conductivity: Perovskites' thermal conductivity can vary with composition and temperature, impacting their use in thermal management and thermoelectric devices.

- Chemical Reactivity: Perovskites' chemical reactivity influences their interaction with other materials and their behavior under different conditions.

The intricate interplay between the physical and chemical properties of perovskite materials contributes to their versatility and potential applications in a wide range of fields, from electronics and energy to catalysis and beyond.

1.4.4.3 Material Properties

- Ferroelectricity: Specific perovskites showcase ferroelectric behavior, characterized by a spontaneous electric polarization that can be manipulated by an external electric field. This property is integral to memory devices, sensors, and actuators.

- Ferroelasticity: Perovskites can exhibit ferroelastic characteristics, manifesting reversible structural changes in response to external stresses. This property holds significance in microelectromechanical systems (MEMS) and other mechanical devices.

- Dielectric Properties: Numerous perovskite materials boast elevated dielectric constants, rendering them valuable in capacitors, microwave devices, and communication systems.

- Piezoelectricity: Certain perovskites demonstrate the piezoelectric effect, generating an electric charge when subjected to mechanical stress. This phenomenon finds applications in sensors, transducers, and energy harvesting systems.

- Optical Properties: Perovskite materials engage in robust interactions with light, positioning them as viable candidates for optoelectronic applications such as light-emitting diodes (LEDs), lasers, and photodetectors.

- Superconductivity: Select perovskites, particularly those containing copper or iron, exhibit superconducting behavior at low temperatures. This property underpins applications in energy transmission and magnetic resonance imaging (MRI).

- Ionic Conductivity: Certain perovskite compositions showcase notable ionic conductivity, rendering them pertinent to solid oxide fuel cells, oxygen sensors, and electrochemical devices.

- Magnetic Properties: Perovskites enriched with transition metals can manifest magnetic attributes, including ferromagnetism, antiferromagnetism, and intricate magnetic behaviors. Such properties contribute to data storage and spintronics applications.

- Photovoltaic Properties: Organic-inorganic hybrid perovskites have gained substantial traction for their exceptional photovoltaic traits. With high light absorption coefficients and charge carrier mobility, they hold promise in solar cell technologies.

- Catalytic Activity: Certain perovskite materials exhibit catalytic prowess owing to distinctive surface chemistry and redox capabilities. They find utility in fuel cells, catalytic converters, and environmental remediation.

- Thermal Properties: Some perovskites present exceptional thermal stability and minimal thermal expansion coefficients, qualifying them for high-temperature applications in aerospace, electronics, and thermal barrier coatings.

- Thermal Conductivity: Perovskites' thermal conductivity varies with composition and structure, affecting their applicability in thermal management and thermoelectric devices.

- Thermoelectric Properties: Certain perovskite materials display thermoelectric behavior, allowing them to convert heat differentials into electricity, thereby holding promise in waste heat recovery and energy harvesting.

- Stability: Perovskite materials' stability, especially under ambient conditions, is crucial for their durability in various applications, including photovoltaics and electronics.

- Multiferroicity: Select perovskites simultaneously exhibit ferroelectric and magnetic attributes, providing avenues for coupled functionalities in memory and sensing devices.

- Flexoelectricity: Flexoelectricity, a property involving electric polarization induced by strain gradients, is present in some perovskites. This feature finds relevance in nanoelectromechanical systems (NEMS).

- Mixed Ionic-Electronic Conductivity: Specific perovskites showcase a combination of ionic and electronic conductivity, making them pertinent for applications like solid oxide electrolytes in advanced batteries and fuel cells.

1.5 High Entropy Perovskites

Alright, let's dive into the fascinating world of high entropy perovskites (HEPs) —a story that combines science and intrigue on the atomic scale! Imagine a realm so small, it's beyond the reach of our eyes, where atoms dance in a mesmerizing ballet. At the heart of this story lies the perovskite—a crystal structure that has caught the attention of scientists and materials enthusiasts alike. But now, imagine something even more enchanting: high entropy perovskites!

Perovskites, as mentioned in last section, are like tiny building blocks that can stack together to create intricate structures. They're named after a mineral discovered in the Ural Mountains that caught the eye of a 19th-century Russian mineralogist, Lev Perovski. The magic of perovskites lies in their versatility—they're like LEGO bricks for scientists, allowing them to craft all sorts of materials with unique properties.

Now, picture a colorful mosaic where each tile is a different element. HEPs are like mosaics taken to the extreme! Traditionally, perovskites are made using three main types of atoms, creating a sort of 'trilogy' in the crystal structure. But in the high entropy version, it's a gathering of not just three, but a whole party of different elements. Imagine trying to fit not just red, blue, and green tiles, but a rainbow of colors into each tile! It's like throwing a fabulous masquerade ball where every atom wears a different costume.

The formation of HEPs is based on the principle of entropy stabilization. Thermodynamics predicts that the structure which minimizes Gibbs free energy for a given temperature and pressure will form. The formula for Gibbs free energy is given by,

$$\Delta G = \Delta H - T\Delta S \quad (23)$$

Where, G is Gibbs free energy, H is enthalpy, T is absolute temperature and S is entropy. It can clearly be seen from this formula that a large entropy reduces Gibbs free energy and thus favors phase stability. It can also be seen that entropy becomes increasingly important in determining phase stability at higher temperatures. In a multi-component system, one component of entropy is the entropy of mixing, (ΔS_{mix}). For an ideal mixture, ΔS_{mix} takes the form:

$$\Delta S_{mix} = -R \sum_{i=1}^{n} c_i \ln c_i \quad (24)$$

Where R is the ideal gas constant, n is the number of components, and c_i is the atomic fraction of component i. The value of ΔS_{mix} increases as the number of components increases. For a given number of components ΔS_{mix} is maximized when the atomic fractions of the components approach equimolar amounts. Evidence for entropy stabilization is given by the original rock salt High Entropy Oxide $(MgNiCuCoZn)_{0.2}O$. Single-phase $(MgNiCuCoZn)_{0.2}O$ may be prepared by solid-state reaction of CuO, CoO, NiO, MgO, and ZnO [6]. Rost et al. reported that under solid state reaction conditions that produce single-phase $(MgNiCuCoZn)_{0.2}O$, the absence of any one of the five oxide precursors will result in a multi-phase sample [6], suggesting that configurational entropy stabilizes the material. It can clearly be seen from the formula for Gibbs free energy that enthalpy reduction is another important indicator of phase stability. For a HEP to form, the enthalpy of formation must be sufficiently small to be overcome by configurational entropy. Furthermore, the discussion above assumes that the reaction kinetics allow for the thermodynamically favored phase to form.

The first report on the successful synthesis of high-entropy oxides (HEOs) with a rock salt structure formed from equimolar amounts of five transition metals was published in 2015 by Rost et al. [6]

But why create such a chaotic, diverse gathering of elements? Well, this is where the intrigue deepens. The atomic dance in high entropy oxides generates a chaotic jumble that, surprisingly, leads to remarkable properties. Imagine a symphony orchestra, where each musician plays their instrument perfectly, creating a harmonious masterpiece. Recent studies reveal that a

variety of multicomponent oxides systems with high configuration entropy can be produced, which possess remarkable electrical, thermal, catalytic, or magnetic properties. This is why HEOs are considered as attractive functional materials for various fields, such as microelectronics, catalytic converters, and energy and data storage. [7] Successful synthesis of perovskite-type HEOs was reported for the first time in 2018 by Sarkar et al. [8] They obtained a series of multicomponent oxides of rare earth and transition metals with high configuration entropy, namely, multicomponent equiatomic perovskite oxides, employing the nebulized spray pyrolysis technique. multicomponent equiatomic perovskite oxides should be considered as a key idea for controlling electronic and magnetic properties of transition metal perovskite oxides, providing a means for subtle control of the B-site charge and tolerance factor by introducing various cations into A-sites. [7] In high entropy perovskites, each atom contributes its unique 'note,' resulting in an orchestra of extraordinary properties—like the ability to conduct electricity, generate light, or even convert sunlight into energy more efficiently than ever before. There is high potential for the development of new types of electronic composite-type materials based on HEPs. It yields additional degrees of freedom for the design of advanced devices based on multifunctional (magnetic, ionic, and electronic) properties of perovskite oxides stabilized by high entropy.

In 1926, Goldschmid introduced a structural "tolerance factor" [9] to predict the stability of perovskite,

$$t = \frac{R_A + R_0}{\sqrt{2}(R_B + R_0)} \tag{25}$$

where R_A, R_B and R_O, respectively, are the radii of A cation, B cation and oxygen anion.

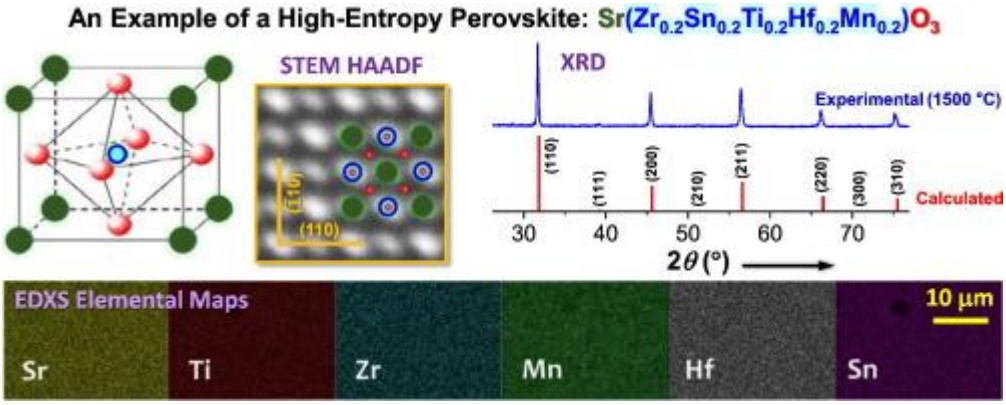

Fig 1.10 example of a high entropy perovskite [11]

A cubic phase is likely stable if $0.9 \leq t \leq 1.0$, while a hexagonal or tetragonal phase may form if $t > 1.0$ and an orthorhombic or rhombohedral phase may form if $t < 0.9$. [10]

ABO_3 perovskite oxides have excellent, diverse physical properties for applications in many different areas and doping them with multiple cations may allow simultaneous tailoring of multiple physical properties of ABO_3 perovskite oxides to meet challenging requirements of various applications. [11]

What's the most thrilling part? These substances have a chance to change the face of technology. Consider a world in which a cell phone charges in a matter of seconds solar panels are just as effective as magic wands, and lightning-fast computers fit in the palm of your hand. High entropy perovskites may hold the key to realizing these fantasies.

So, there it is, a little story of high entropy perovskites, where atoms congregate in a crazy dance of elements, breaking the conventions of regular crystal formations.

1.6 Objective of work

1.6.1 Thesis Objective: Synthesis, Characterization, and Evaluation of New High Entropy Perovskites for Enhanced Thermoelectric Performance

The primary objective of this thesis is to synthesize, thoroughly test, and comprehensively characterize a series of perovskite materials, focusing on six distinct compositions. Notably, the final two compositions, denoted as HEP-1 and HEP-2, are novel high entropy perovskites synthesized through a tailored sol-gel method followed by solvent-aided grinding and calcination processes. Of paramount significance is the groundbreaking ABX3 structure introduced in HEP-2, which has not been reported in any previous literature.

1.6.2 Synthesis Approach:

The synthesis process involves the systematic combination of elements to create well-defined compositions. For HEP-2, the innovative ABX3 configuration is realized by incorporating equimolar amounts of La and Sr into site A, while employing a combination of Fe, Mn, Cu, Ni, Co, and Cr for site B, with oxygen occupying site X. This unique arrangement aims to enhance electrical conductivity and concurrently reduce thermal conductivity through phonon dispersion mechanisms.

1.6.3 Characterization and Evaluation:

After synthesis, the synthesized samples are meticulously characterized to elucidate their structural, chemical, and physical attributes. Thin films and pellets are produced to assess their thermoelectric properties. A key focus lies in enhancing the power factor and figure of merit by optimizing electrical conductivity and thermal conductivity reduction.

1.6.4 Customized Experimental Setup:

An integral aspect of this research is the design, construction, and customization of an Arduino-based device setup. This setup facilitates the accurate investigation of thermoelectric

properties, enabling real-time data collection and analysis. The device is crafted specifically for this research, demonstrating the commitment to advancing the field of thermoelectrics.

1.6.5 Contributions and Innovation:

By synthesizing and characterizing the six perovskite compositions, particularly the novel HEP-2 structure, this research seeks to push the boundaries of thermoelectric material design. The intended outcome is a detailed understanding of the relationships between composition, crystal structure, and thermoelectric performance. The proposed enhancement of power factor and figure of merit, achieved through improved electrical conductivity and tailored phonon dispersion, holds the potential for significant contributions to energy harvesting and conversion technologies.

To summarize, this thesis aims to pioneer new avenues in the realm of perovskite thermoelectric materials through the synthesis, characterization, and evaluation of a novel ABX3 structure. The development of a specialized experimental setup further underscores the dedication to advancing scientific understanding and practical applications in the field of thermoelectrics.

1.7 References

1. Kokarneswaran, M., Selvaraj, P., Ashokan, T., Mohan, N., & Chadrasekaran, V. (2020). Discovery of carbon nanotubes in sixth century BC potteries from Keeladi, India. Journal of Archaeological Science, 117, 105198.

2. Reiss, Guenter & Hutten, Andreas. (2005). Magnetic nanoparticles: Applications beyond data storage. Nat Mater. 4. 725-726.

3. Taniguchi, N. (1974). On the Basic Concept of 'Nano-Technology'. In Proceedings of the International Conference on Production Engineering, Tokyo, 1974, Part II.

4. Drexler, K. E. (1981). Molecular engineering: An approach to the development of general capabilities for molecular manipulation. Journal of the American Chemical Society, 103(24), 7661-7662.

5. Orlovskaya, N., Browning, N., & Nicholls, A. (2003, October). Ferroelasticity in mixed conducting LaCoO3 based perovskites: a ferroelastic phase transition. Acta Materialia, 51(17), 5063–5071.

6. Rost, C. M., Sachet, E., Borman, T., Moballegh, A., Dickey, E. C., Huo, D., Jones, J. L., Curtarolo, S., & Maria, J.-P. (2015). Entropy-stabilized oxides. Nature Communications, 6, 8485.

7. Krawczyk, P. A., Jurczyszyn, M., Pawlak, J., Salamon, W., Baran, P., Kmita, A., Gondek, Ł., Sikora, M., Kapusta, C., Strączek, T., Wyrwa, J., & Żywczak, A. (2020). High-Entropy Perovskites as Multifunctional Metal Oxide Semiconductors: Synthesis and Characterization of (Gd0.2Nd0.2La0.2Sm0.2Y0.2)CoO3. ACS Applied Electronic Materials, 2(10), 3211-3220.

8. Sarkar, A.; Djenadic, R.; Wang, D.; Hein, C.; Kautenburger, R.; Clemens, O.; Hahn, H. (2018). Rare earth and transition metal-based entropy stabilised perovskite type oxides. Journal of the European Ceramic Society, 38(8), 2318

9. Goldschmidt, M. (1926). Naturwissenschaften, 14, 477–485.

10. Ramadass, N. (1978). Mater. Sci. Eng., 36, 231-239.

11. Jiang, S., Hu, T., Gild, J., Zhou, N., Nie, J., Qin, M., Harrington, T., Vecchio, K., & Luo, J. (2018). A new class of high-entropy perovskite oxides. Scripta Materialia, 142, 116–120.

12. Kong, Ling Bing (2014). Waste Energy Harvesting. Lecture Notes in Energy. Vol. 24. Springer. pp. 263–403.

13. Datta, Supriyo (2005). Quantum Transport: Atom to Transistor. Cambridge University Press. ISBN 9780521631457.

14. Cutler, M.; Mott, N. (1969). "Observation of Anderson Localization in an Electron Gas". Physical Review. 181 (3): 1336.

15. Jonson, M.; Mahan, G. (1980). "Mott's formula for the thermopower and the Wiedemann-Franz law". Physical Review B. 21 (10): 4223.

16. Franz, R.; Wiedemann, G. (1853). "Ueber die Wärme-Leitungsfähigkeit der Metalle"

17. Imai, H.; Shimakawa, Y.; Kubo, Y. (10 December 2001). "Large thermoelectric power factor in TiS2 crystal with nearly stoichiometric composition". Physical Review B. 64 (24): 241104.

18. Mahan, G. D.; Lindsay, L.; Broido, D. A. (28 December 2014). "The Seebeck coefficient and phonon drag in silicon". Journal of Applied Physics.

19. Bulusu, A.; Walker, D. G. (2008). "Review of electronic transport models for thermoelectric materials". Superlattices and Microstructures.

20. Comptes Rendus Physique Draft. (n.d.). Retrieved August 7, 2023, from https://arxiv.org/pdf/2204.04429.pdf

21. The Seebeck Coefficient. (2013, February 1). Electronics Cooling. https://www.electronics-cooling.com/2013/02/the-seebeck-coefficient/

22. Moore, J. P. (1973). "Absolute Seebeck coefficient of platinum from 80 to 340 K and the thermal and electrical conductivities of lead from 80 to 400 K". Journal of Applied Physics. 44 (3): 1174–1178.

23. Peltier (1834). "Nouvelles expériences sur la caloricité des courants électrique"

24. Thomson, William (1857). "4. On a Mechanical Theory of Thermo-Electric Currents". Proceedings of the Royal Society of Edinburgh. Cambridge Univ. Press. 3: 91–98.

25. Thomson, William (1857). "On the dynamical theory of heat. Part V. Thermo-electric currents"

26. Leon van Dommelen (2002-02-01). "A.11 Thermoelectric effects". eng.famu.fsu.edu. Retrieved 2022-11-23.

27. M., Borrego, Jose (1962). Optimum impurity concentration in semiconductor thermoelements. Massachusetts Institute of Technology, Energy Conversion and Semiconductor Laboratory, Electrical Engineering Dept. OCLC 16320521

28. Snyder, G.J. (2017). "Figure of merit ZT of a thermoelectric device defined from materials properties". Energy and Environmental Science. 10 (11): 2280–2283. doi:10.1039/C7EE02007D

29. Kim, D.S.; Infante Ferreira, C.A. (2008). "Solar refrigeration options – a state-of-the-art review". International Journal of Refrigeration. 31: 3–15. doi:10.1016/j.ijrefrig.2007.07.011

30. Timothy D. Sands (2005), Designing Nanocomposite Thermoelectric Materials

31. Bhandari, C. M. in Rowe 2018, pp. 55–65

32. Cava, R. J. (1990). "Structural chemistry and the local charge picture of copper-oxide superconductors". Science. 247 (4943): 656–62. Bibcode:1990Sci...247..656C

33. Dresselhaus, M. S.; Chen, G.; Tang, M. Y.; Yang, R. G.; Lee, H.; Wang, D. Z.; Ren, Z. F.; Fleurial, J.-P.; Gogna, P. (2007). "New directions for low-dimensional thermoelectric materials"

34. Green, M. A., Ho-Baillie, A., & Snaith, H. J. (2014). The emergence of perovskite solar cells. Nature Photonics, 8(7), 506-514.

35. Tokura, Y. (2006). Critical features of colossal magnetoresistive manganites. Reports on Progress in Physics, 69(3), 797

2 Literature Review

2.1 A new class of high-entropy perovskite oxides

In the realm of high-entropy perovskite oxides, recent research by Jiang et al. sheds light on the synthesis, characterization, and pivotal factors influencing their formation [1]. These multi-cation perovskite solid solutions, possessing high configuration entropies, hold significant promise due to their diverse physical properties and potential applications. The study delves into the synthesis of single solid-solution phases within this class of materials, focusing on elucidating the role of the Goldschmidt tolerance factor as a key criterion. While the tolerance factor near unity is identified as a crucial condition for the emergence of single high-entropy perovskite phases, it is not the sole determinant.

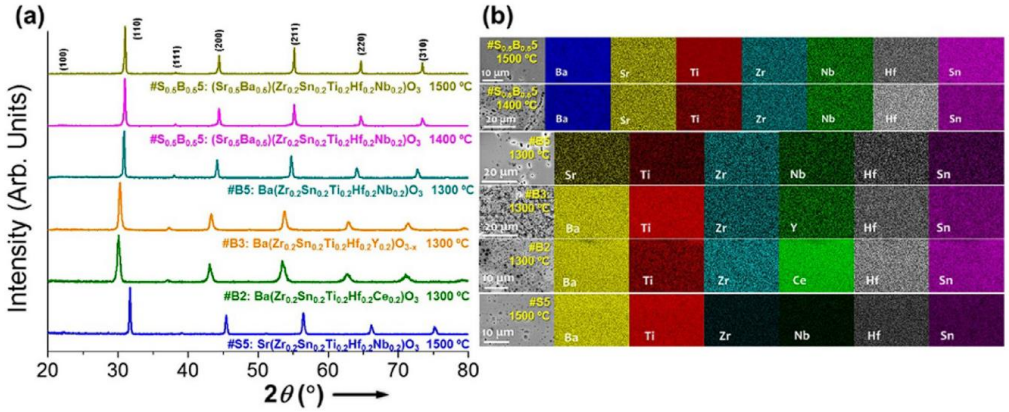

Fig 2.1 (a) XRD patterns of five other compositions that form single-phase high-entropy perovskite oxides (at specific temperatures, labeled in the graph), where the peaks of the cubic perovskite phases are indexed. (b) The corresponding EDXS elemental maps, showing the compositional homogeneity. [1]

Through experimentation and analysis, the researchers examine a range of compositions, encompassing both Sr-based and Ba-based perovskite oxides. [1] They synthesized a new class of high-entropy perovskite oxides, multiple-cation solid solutions with high configurational entropies, with possibility of simultaneous tailoring of multiple physical properties because of their distinct and highly-tunable chemistries. They also reported the synthesized high-entropy materials that have a complex ionic crystal structure with at least two cation sublattices. This work opens avenues for tailoring material properties through diverse compositional variations, thereby offering novel perspectives for harnessing the unique features of high-entropy perovskite oxides in applications such as thermoelectric devices. [1]

2.2 Thermoelectric properties and electrical characteristics of sputter-deposited p-$CuAlO_2$ thin films

In the study conducted by Banerjee et al. [2], the thermoelectric and electrical properties of dc-sputtered copper aluminum oxide ($CuAlO_2$) thin films were investigated. Natural layered-structure materials with a two-dimensional effective carrier density demonstrated an improved thermoelectric figure-of-merit. $CuAlO_2$, which has a natural superlattice structure, has excellent thermoelectric capabilities and may be a promising thermoelectric material for future applications.

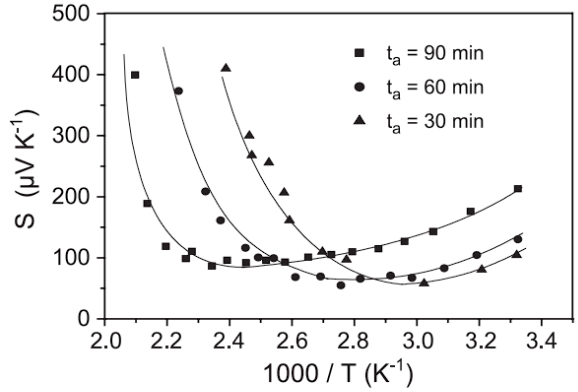

Fig 2.2.2 Seebeck coefficient vs.1000/*T* of $CuAlO_2$ thin films[2]

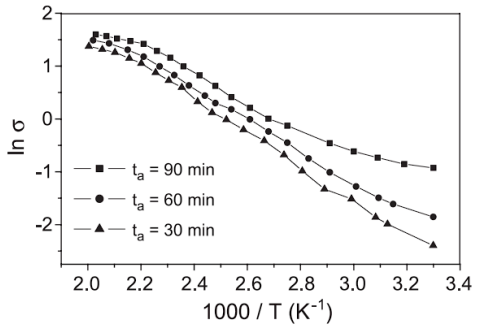

Fig 2.2.1 Temperature dependence of conductivity of $CuAlO_2$ thin films[2]

The authors examined the influence of postdeposition annealing in an oxygen atmosphere on the p-type conductivity of these films. Their findings revealed that the films exhibited a rhombohedral crystal structure with the R3m space group [2]. Notably, the electrical conductivity of the films was observed to increase with annealing time, leading to varying conductivities ranging from 0.09 to 0.39 S cm^{-1} at room temperature [2]. This enhancement in conductivity was attributed to excess oxygen content within the crystallite sites, resulting in improved p-type conductivity [2]. Furthermore, activation energy values for carrier transport were determined, providing insights into the charge carrier behavior [2]. The positive Seebeck coefficients confirmed the p-type nature of the films [2]. These findings underscore the potential of $CuAlO_2$ thin films for thermoelectric applications, particularly due to their layered structure and enhanced thermoelectric properties, which align with the ongoing research on similar materials [2].

2.3 Optical and thermoelectric properties of chalcogenide based Cu_2NiSnS_4 nanoparticles synthesized by a novel hydrothermal route

An intriguing study by Sarkar et al. investigated the optical and thermoelectric properties of Cu_2NiSnS_4 (CNTS) nanoparticles synthesized through a unique hydrothermal route [3]. This work holds relevance in the context of high entropy perovskites and their potential in energy harvesting.

The researchers undertook a comprehensive analysis of the synthesized CNTS nanoparticles. Structural characterization using X-ray diffraction (XRD) and transmission electron microscopy (TEM) confirmed the phase and crystallinity of the material [3].

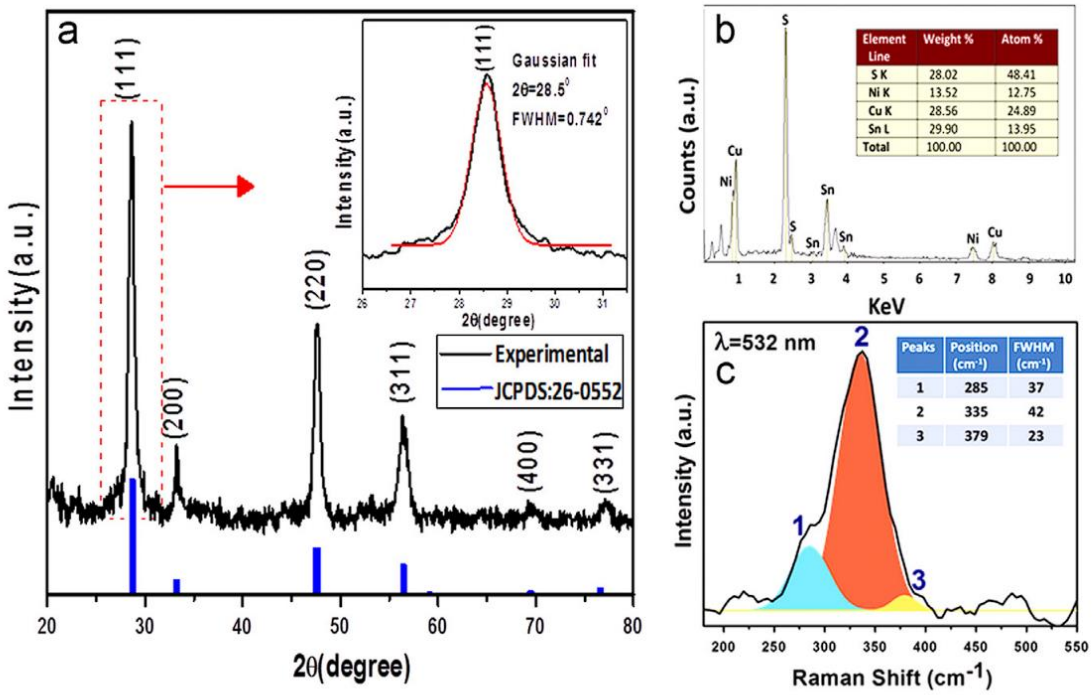

(a) XRD pattern of CNTS sample. Inset-Scherrer particle size calculation. (b) EDS analysis. (c) Raman Spectra of CNTS.

Fig 2.3[3]

Morphology studies utilizing field emission scanning electron microscopy (FESEM) and high-resolution TEM revealed irregular assemblies of nanostructures with particle sizes ranging from 10 to 20 nm.

One of the significant findings pertains to the optical properties of CNTS. The researchers reported an optical band-gap of 1.56 eV, making CNTS a promising candidate for thin film solar cell applications [3]. Furthermore, the photo response behavior of CNTS films demonstrated substantial light-to-dark current ratios, suggesting its potential use in solar cell devices.

Notably, the study delved into the thermoelectric properties of CNTS for the first time. The positive Seebeck coefficient indicated the p-type nature of the material, and the thermoelectric power factor reached a noteworthy value of 603 × 10^{-6} mW m^{-1} K^{-2} at 440 K [3]. These findings open avenues for the application of CNTS in high-temperature thermoelectric devices.

The investigation conducted by Sarkar et al. showcases the synthesis and characterization of Cu_2NiSnS_4 nanoparticles and their promising optical and thermoelectric properties [3]. The insights gained from this study contribute to the ongoing exploration of advanced materials with tailored properties for energy conversion and harvesting.

2.4 Stabilization by Configurational Entropy of the Cu(II) Active Site during CO Oxidation on $Mg_{0.2}Co_{0.2}Ni_{0.2}Cu_{0.2}Zn_{0.2}O$

A notable study by Fracchia et al. (2020) sheds light on the catalytic prowess of high-entropy oxides, specifically the $Mg_{0.2}Co_{0.2}Ni_{0.2}Cu_{0.2}Zn_{0.2}O$ rock-salt structure. The authors employed a comprehensive approach, including X-ray absorption spectroscopy (XAS) and powder X-ray diffraction analysis, to unravel the complexities of carbon monoxide (CO) oxidation on this unique material [4].

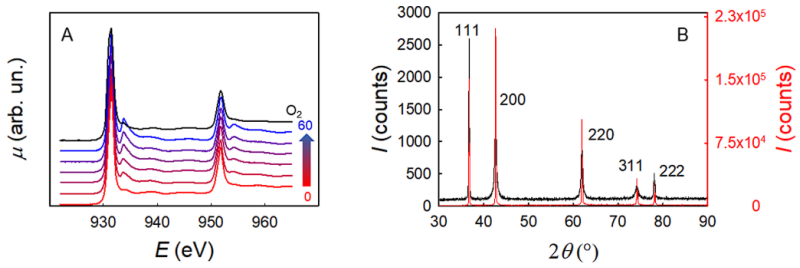

Fig 2.4 (A) Cu $L_{2,3}$-edge XAS spectra of the $Mg_{0.2}Co_{0.2}Ni_{0.2}Cu_{0.2}Zn_{0.2}O$ HEO material for different time periods in CO at 235 °C (red to blue lines; numbers 0 → 60 are the dwell times under these conditions expressed in minutes) and then in O_2 at the same temperature (black line). (B) Comparison of the PXRD patterns of the raw HEO material (red line) and the same material after all of the thermal treatments described in this work (black line). The patterns are indexed according to the rock-salt structure ($Fm\bar{3}m$, a = 4.2366(5) Å). [4]

Intriguingly, this study unveils the pivotal role of copper (Cu) cations in the CO oxidation process within the high-entropy oxide lattice. Through reactive adsorption, Cu(II) is adeptly

reduced to Cu(I), followed by a subsequent oxidation step that restores its Cu(II) oxidation state [4]. The stability of the Cu(II)/Cu(I) redox couple, inherently supported by the rock-salt structure, emerges as a crucial factor influencing the catalytic activity [4]. These findings hold significant implications for the broader field of high entropy perovskites, where the synergy between compositional diversity and structural stability governs their thermoelectric properties. By building upon the insights from Fracchia et al.'s investigation, we can extrapolate the potential of designing novel high entropy perovskites with tailored thermoelectric behavior.

2.5 Stabilizing term in rock-salt $Mg_{0.2}Co_{0.2}Ni_{0.2}Cu_{0.2}Zn_{0.2}O$ high entropy oxide

The study by Fracchia et al. ventures the multifaceted nature of stability in high entropy perovskites. It sheds new light on the factors governing stability. Their work relates to earlier findings by Rost et al. While Rost and team suggested that configurational entropy is the key to stability, Fracchia and her co-authors investigated if any other factors were involved.

At the heart of their study is the exploration of rock-salt solid solutions, particularly the Mg-Co-Ni-Cu-Zn-O system. The authors looked beyond the configurational entropy, peering into the influence of solubility equilibria. Through experiments, they created a range of solid solutions, keeping the molar fractions of CuO and ZnO around 0.2, akin to a cornerstone composition (E1). Their findings challenge the dominance of configurational entropy, revealing that the stability also involves other factors, like the delicate equilibrium between solubility and structure.

The authors' insights enrich our understanding of the nuanced mechanisms at play within these intricate systems.

2.6 Electrical and thermal transport behaviors of high-entropy perovskite thermoelectric oxides

In the study by Zheng et al. [6], the focus was on exploring the potential of $(Ca_{0.2}Sr_{0.2}Ba_{0.2}Pb_{0.2}La_{0.2})TiO_3$, a high-entropy perovskite oxide, to alter the landscape of thermoelectric materials.

The authors synthesized the material through a solid-state reaction and conventional sintering method, yielding a high-entropy structure characterized by a disordered solid solution. This unique structure, attributed to the incorporation of multiple elements in approximately equal molar fractions, induced a remarkable suppression of lattice thermal conductivity.

This phenomenon was found to stem from the material's distinctive lattice distortion and mass fluctuation, showcasing the potential of high-entropy ceramics to engineer thermal properties

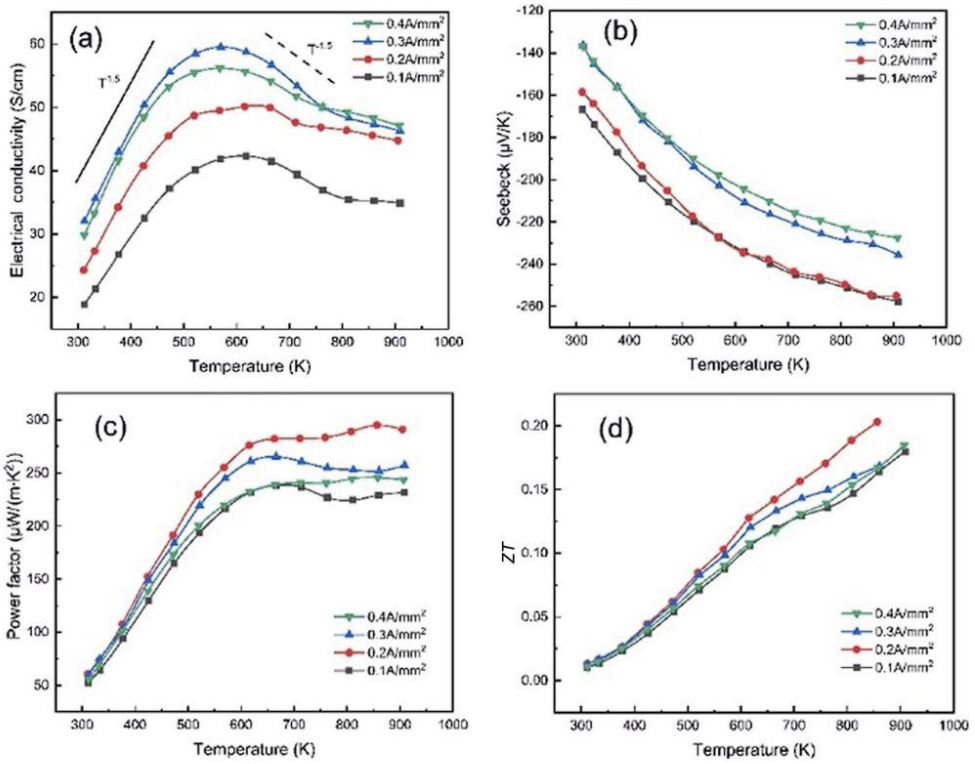

Fig 2.6 Electrical properties and *ZT* of annealed $(Ca_{0.2}Sr_{0.2}Ba_{0.2}Pb_{0.2}La_{0.2})TiO_3$: (a) electrical conductivity; (b) Seebeck coefficient; (c) power factor; (d) *ZT*.[6]

[6].

One of the interesting aspects of this study lies in the novel approach of electrical current-assisted annealing. By applying an external electrical current during the annealing process, the material underwent a transformation, generating oxygen vacancies that resulted in enhanced carrier concentration within the bulk. This increase in carrier concentration led to a boost in the material's thermoelectric performance [6]. The work also included into in-depth analysis of various properties, including thermal diffusivity, electrical conductivity, Seebeck coefficient, power factor, and the thermoelectric figure of merit (ZT). Notably, the annealed high-entropy perovskite

oxide achieved an impressive ZT value of over 0.2 at 873 K, a significant milestone in the pursuit of efficient thermoelectric materials [6].

The study underscores the potential of high-entropy ceramics, particularly $(Ca_{0.2}Sr_{0.2}Ba_{0.2}Pb_{0.2}La_{0.2})TiO_3$, to revolutionize the field of thermoelectrics. The combination of suppressed lattice thermal conductivity and enhanced carrier concentration presents a promising avenue for the development of advanced thermoelectric materials with improved energy conversion efficiency [6]

2.7 High-entropy $(Ca_{0.2}Sr_{0.2}Ba_{0.2}La_{0.2}Pb_{0.2})TiO_3$ perovskite ceramics with A-site short-range disorder for thermoelectric applications

Zhang et al. presents an insightful exploration into the synthesis and thermoelectric properties of $(Ca_{0.2}Sr_{0.2}Ba_{0.2}La_{0.2}Pb_{0.2})TiO_3$ ceramics [7]. The researchers skillfully crafted a single-phase solid solution using innovative techniques and then meticulously probed its thermoelectric characteristics. The annealing temperature emerged as a crucial factor, demonstrating a positive correlation with the Seebeck coefficient, a pivotal indicator of thermoelectric performance. The study unearthed the involvement of localized carriers near ionization centers in facilitating conduction at elevated temperatures [7].

An intriguing revelation was the significant decrease in thermal conductivity, attributed to the presence of multi-scale as point defects, dislocations, and nanoscale grain boundaries [7]. This intricate interplay between electrical and thermal conductivity, as well as carrier concentration, underscored the materials' potential for thermoelectric applications. Furthermore, the analysis of the figure of merit (ZT) unveiled promising avenues to achieve higher performance in these high-entropy ceramics [7].

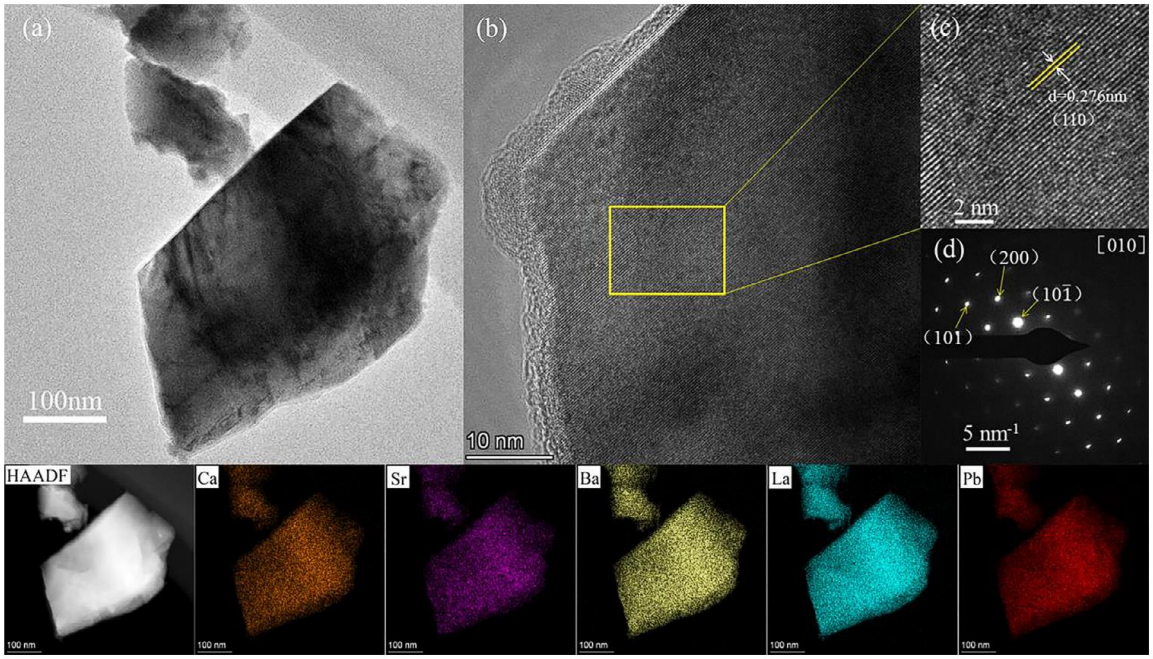

Fig 2.7 TEM (a), HRTEM (b), SAED (c) and HAADF corresponding EDS mapping of high-entropy CSBLP ceramic sintered at 1250°C-2h and then annealed at 1300°C-8h. [7]

In sum, Zhang and team's work adds a valuable layer to the discourse on high-entropy perovskites, specifically shedding light on their synthesis techniques and thermoelectric effects. The findings underscore the potential of $(Ca_{0.2}Sr_{0.2}Ba_{0.2}La_{0.2}Pb_{0.2})TiO_3$ ceramics as promising candidates for enhancing thermoelectric performance.

2.8 Mild hydrothermal synthesis and physical property of perovskite Sr doped $LaCrO_3$

The study by Wang et al. [8] focuses on a novel approach of synthesizing perovskite Sr-doped $LaCrO_3$ compounds under mild hydrothermal conditions. Mild hydrothermal synthesis and physical property of perovskite Sr doped $LaCrO_3$ presents a comprehensive exploration of the synthesis, structural characterization, and physical properties of Sr-doped $LaCrO_3$ compounds. The study primarily focuses on understanding the effects of Sr doping on the crystalline structure, electrical conductivity, and magnetic behavior of the resulting compounds.

The researchers investigated the effects of Sr doping on the structural and electrical properties of $LaCrO_3$. Through experimentation, they established a two-step process to optimize the alkalinity of the reaction mixture, employing a mild hydrothermal synthesis route at 260°C [8]. This approach yielded cube-shaped crystalline phases with dimensions around 1-2 μm, indicating the successful formation of perovskite-like structures.

Electrical conductivity measurements conducted by the authors revealed intriguing behavior in response to Sr doping. Conductivity increased with higher Sr content, implying enhanced charge carrier mobility. This phenomenon can be attributed to the small polaron hopping

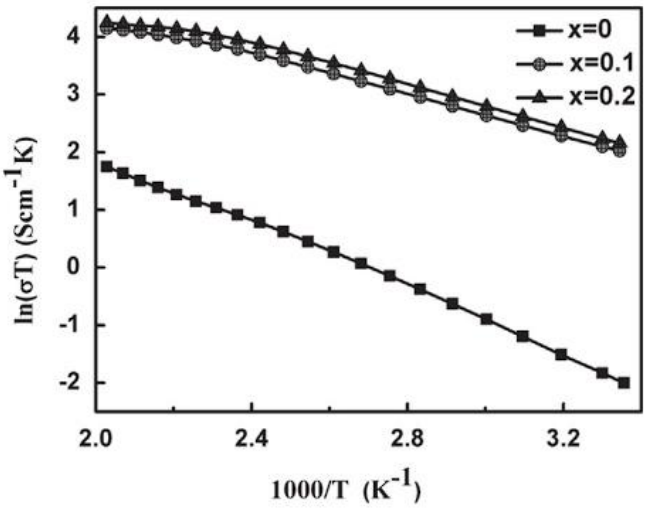

Fig 2.8 Temperature dependence of conductivity of the samples $La_{1-x}Sr_xCrO_3$ (x=0, 0.1, 0.2). [8]

conduction mechanism, a hallmark of these materials [8]. The researchers also mention the significance of the temperature-dependent electrical behavior, emphasizing the potential of these compounds for thermoelectric applications.

The study also mentions the magnetic properties of the synthesized compounds. An antiferromagnetic transition was observed in all samples, which is consistent with earlier reports [8]. The Néel temperatures for $LaCrO_3$, $La_{0.9}Sr_{0.1}CrO_3$, and $La_{0.8}Sr_{0.2}CrO_3$ were determined as 253 K, 260 K, and 252 K, respectively [8]. These findings are shows interconnection between doping and magnetism in perovskite materials, offering insights into their multifaceted behavior.

The work by Wang et al. [8] not only advances the understanding of high entropy perovskites but also offers a novel synthesis route that can be harnessed for various applications, including thermoelectric devices.

2.9 Synthesis and characterization of doped $LaCrO_3$ perovskite prepared by EDTA–citrate complexing method

Ding et al.'s study presents a noteworthy contribution, shedding light on the synthesis and characterization of doped $LaCrO_3$ perovskite materials [9].

The authors grapple with the challenge of enhancing sinterability and electrical conductivity, particularly in the context of solid oxide fuel cells (SOFCs). The synthesis process, employing the EDTA–citrate complexing method, emerges as a promising avenue [9].

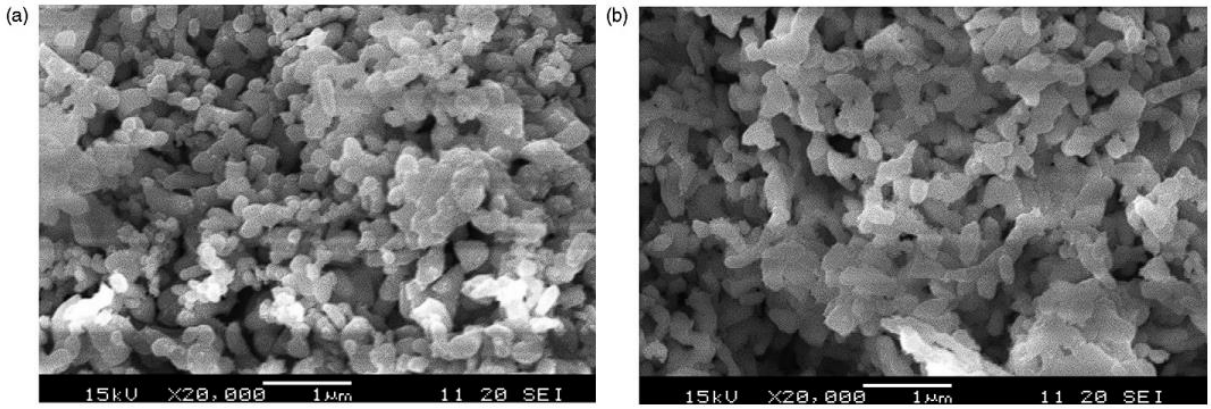

Fig 2.9 SEM images of $La_{0.85}Sr_{0.15}Cr_{0.95}Ni_{0.02}Co_{0.02}O_3$ perovskite powder prepared by EDTA–citrate complexing method at (a) pH 4.9 and (b) pH 6.9. Samples were calcined at 800 °C for 2 h. [9]

This technique orchestrates the chelation of metal ions, ensuing in polymerized powders characterized by impeccable uniformity at the nanoscale. The $La_{0.85}Sr_{0.15}Cr_{0.95}Ni_{0.02}Co_{0.02}O_3$ perovskite powders is a substrate with considerable potential for interconnect materials in SOFCs.

The study tactfully probes the interplay of synthesis parameters, unveiling intriguing insights. Variations in precursor pH values manifest discernible impacts on sintering behavior, with the addition of $SrCrO_4$ as a transient liquid phase playing a pivotal role [9]. The latter fosters enhanced sintering efficiency and heightened density, unraveling pathways to overcome the sintering challenge.

Intriguingly, the electrical conductivity, a quintessential parameter for SOFCs, emerges as a fingerprint of the pH-dependent synthesis route. A nuanced exploration showcases a marked discrepancy in conductivity, with pH 4.9 yielding significantly higher values [9]. This nuanced difference is attributed to the tailored microstructure and denser crystal arrangement facilitated by the unique synthesis path.

In the overarching landscape of thermoelectric effects, Ding et al.'s study opens avenues for synergizing the synthesis intricacies of $LaCrO_3$ perovskites with the broader spectrum of high entropy systems. As we tread forth into the realm of high entropy perovskites, their synthesis journey, guided by the EDTA–citrate complexing method, stands poised to illuminate avenues for novel applications.

2.10 $LaCoO_3$: Effect of synthesis conditions on properties and reactivity

The study, conducted by Natile et al. delves into the synthesis, characterization, and catalytic potential of lanthanum cobalt oxide ($LaCoO_3$) perovskite materials.

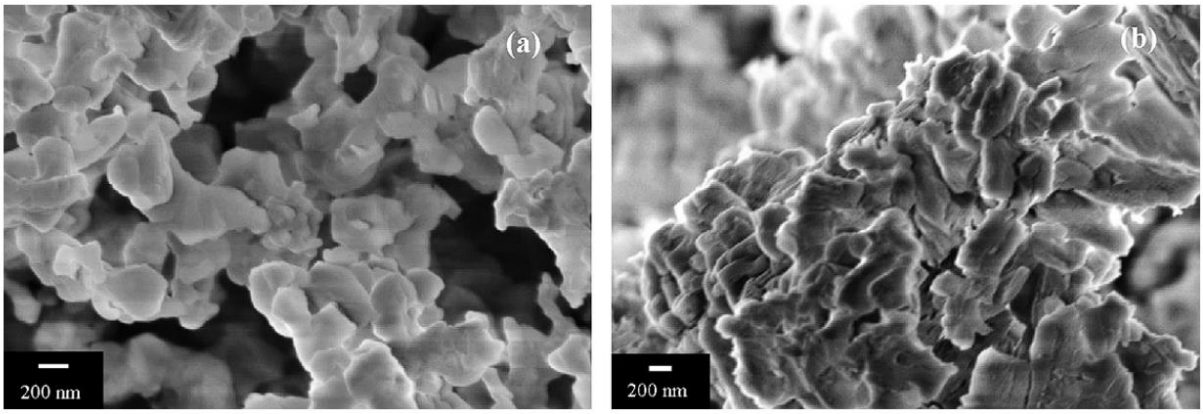

Fig 2.10 SEM micrographs of the nanocomposite with $[Co/La]_{nominal} = 0.055$ (a) and of the supporting La_2O_3 (b). [10]

The study aimed to comprehend the impact of diverse preparation techniques on the chemical and structural attributes of the perovskite samples. Through a meticulous analysis of synthesis methods, material characterization utilizing a spectrum of analytical tools, and the evaluation of catalytic activity in carbon monoxide (CO) oxidation, the researchers presented a comprehensive overview of their findings.

Remarkably, the researchers elucidated the synthesis procedures encompassing nanostructured bulk $LaCoO_3$ through co-precipitation and citrate gel methods. They also ventured into nanocomposite fabrication, generating CoO_x/La_2O_3 materials with varying cobalt-to-lanthanum ratios. A pivotal observation emerged, wherein the crystalline phase, phase composition, surface chemistry, and reactivity of the $LaCoO_3$ samples were significantly influenced by the chosen preparation route [10].

A critical facet of the study revolved around the characterization techniques applied. X-ray diffraction (XRD) analyses unveiled a single-phase $LaCoO_3$ structure solely in the citrate gel method, while hexagonal lanthanum hydroxide phase emerged in co-precipitation and certain nanocomposite samples. The crucial role of X-ray photoelectron spectroscopy (XPS) and diffuse reflectance infrared Fourier transform (DRIFT) spectroscopy was evident in uncovering the surface hydroxylation and carbonate species [10].

Notably, the research extended its purview to catalytic performance, specifically in CO oxidation. It was intriguing to note that CO interacted robustly with the surface, yielding a distinctive signal around 2058 cm^{-1}. Furthermore, all the samples exhibited the ability to oxidize CO to CO_2, with distinctions in reactivity trends among the samples. The nanostructured $LaCoO_3$ prepared via citrate gel method displayed enhanced oxidation capability at lower temperatures, while the co-precipitated counterpart demonstrated heightened activity beyond 523 K.

2.11 Thermoelectric properties of high-entropy rare-earth cobaltates

In the realm of high-entropy perovskites, an innovative avenue of research has unfolded, focusing on their synthesis and profound thermoelectric effects. This captivating study by Kumar et al. explores the synthesis of high-entropy rare-earth cobaltates and their thermoelectric properties, shedding light on a promising avenue for advanced thermoelectric materials [1]. For individuals like my esteemed colleague, grappling with complex literature might prove challenging, but allow me to present a distilled summary of the significant findings from this comprehensive work, tailored for inclusion in a literature review.

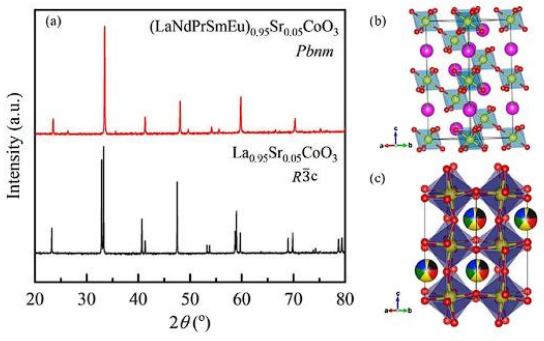

Fig 2.11.1 (a) XRD pattern of $La_{0.95}Sr_{0.05}CoO_3$ and $(LaNdPrSmEu)_{0.95}Sr_{0.05}CoO_3$ are shown. The crystal structure using Vesta software is shown for (b) $La_{0.95}Sr_{0.05}CoO_3$, and (c) $(LaNdPrSmEu)_{0.95}Sr_{0.05}CoO_3$. The structural parameters are obtained from the Rietveld refinement of the XRD pattern. [11]

The researchers embarked on fabricating high-entropy rare-earth cobaltates using conventional solid-state reactions [11]. Through meticulous characterization techniques including X-ray diffraction (XRD) and Rietveld refinement, they confirmed the successful attainment of single-phase structures in the high-entropy configurations, showcasing an intriguing transition from the rhombohedral structure seen in simple perovskites ($La_{0.95}Sr_{0.05}CoO_3$) to an orthorhombic structure [11]. This structural transition not only emphasized the novelty of high-entropy compositions but also led to the optimization of crucial thermoelectric parameters.

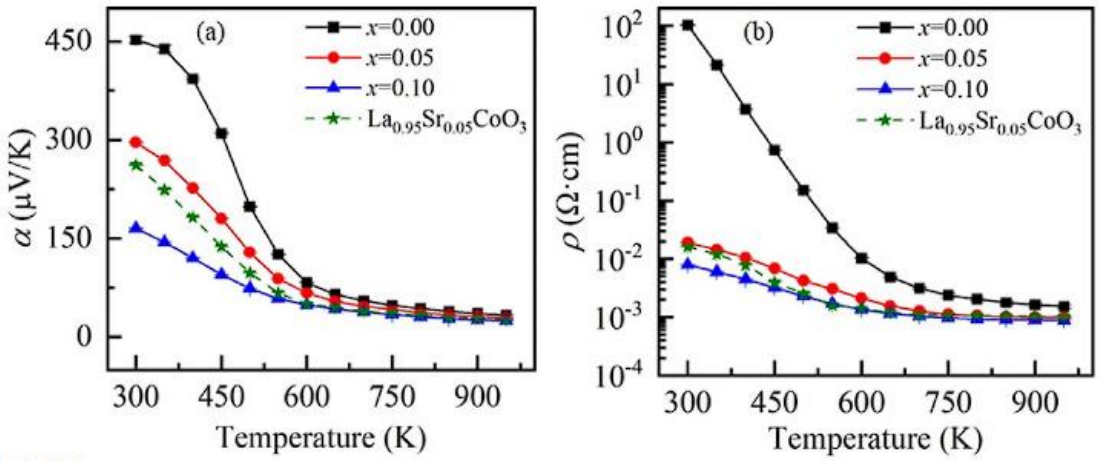

Fig 2.11.2
(a) Seebeck coefficient (α), (b) electrical resistivity (ρ) as a function of temperature for $(LaNdPrSmEu)_{1-x}Sr_xCoO_3$. [11]

Of particular note is the profound impact of Sr substitution on the thermoelectric properties of $(LaNdPrSmEu)_{0.95}Sr_{0.05}CoO_3$ [11]. Before Sr substitution, this composition exhibited higher resistivity and lower Seebeck coefficient [11]. However, the introduction of Sr caused a remarkable transformation, leading to a substantial enhancement in the electrical conductivity [11]. This intriguing shift in electrical behavior following Sr substitution played a pivotal role in the subsequent improvement of thermoelectric performance.

Crucially, the synthesis of $(LaNdPrSmEu)_{0.95}Sr_{0.05}CoO_3$ exhibited an astonishing enhancement in the Seebeck coefficient post-Sr substitution, further magnifying the overall thermoelectric performance. This synergistic combination of increased Seebeck coefficient, improved electrical conductivity, and the reduction in phonon thermal conductivity culminated in the realization of a considerably elevated figure of merit (zT).

Notably, the researchers observed a remarkable zT value of 0.23 ± 0.02 at 350 K for the $(LaNdPrSmEu)_{0.95}Sr_{0.05}CoO_3$ composition [11]. This exceptional zT value, observed at a lower temperature range, stands as a testament to the potent thermoelectric performance achieved through high-entropy compositions, rivaling some of the best zT values reported for p-type oxide materials. Such achievements underscore the promising avenue that high-entropy perovskites represent for the advancement of efficient thermoelectric materials.

In essence, Kumar et al.'s study encapsulates the synthesis and remarkable thermoelectric effects of high-entropy rare-earth cobaltates. The intricate interplay of structural variations, electrical conductivity enhancements, and phonon scattering elucidated in this work holds paramount importance for the development of future thermoelectric materials.

2.12 Perovskite Sr-Doped $LaCrO_3$ as a New p-Type Transparent Conducting Oxide

This paper by Zhang et al. delves into the investigation of La-doped SrCrO3 (LSCO) films and their potential relevance to the field of high entropy perovskites. One notable exploration in this direction involves LSCO thin films, which exhibit promising characteristics as p-type transparent conducting oxides (p-TCOs). [12].

The study begins by emphasizing the crucial role of transparent conducting oxides (TCOs) in modern electronic devices, necessitating a careful balance between electrical conductivity and optical transparency. The focus then shifts to the detailed examination of LSCO films, with an emphasis on their fabrication and characterizations. Epitaxial growth techniques are employed to produce high-quality films on STO substrates, setting the stage for in-depth analyses [12].

Optical absorption spectra of LSCO films are discussed, revealing distinct absorption features, including characteristic peaks at certain energy levels. This provides insights into the energy states within the material, contributing to its optoelectronic properties. Moreover, the electronic density of states is probed through X-ray photoemission and X-ray absorption spectroscopy, shedding light on the electronic structure of LSCO.

A significant aspect of the research pertains to the electronic band structure of LSCO films, particularly the effects of Sr substitution for La. This substitution induces changes in the band

structure, influencing the optical and electronic behaviors of the material. These findings hold implications for the thermoelectric properties of high entropy perovskites [12].

Comparative analyses with other p-type TCOs, including CuCrO2 and Mg-doped CuCrO2, underscore the importance of the electronic structure in achieving favorable p-type conductivity. Notably, the parallels drawn between LSCO and these other materials offer valuable insights into the potential thermoelectric effects of high entropy perovskites [12].

Looking ahead, the study envisions possible applications of LSCO films, suggesting their integration into transparent p-n junctions and other transparent electronic devices. Furthermore, the coherence of LSCO with substrates like $SrTiO_3$ (STO) is explored, hinting at the feasibility of forming device heterojunctions [12].

In conclusion, Zhang et al. contribute a valuable investigation into the properties and applications of LSCO films, offering insights that extend to the realm of high entropy perovskites and their synthesis. The study's meticulous characterizations, comparisons with other TCOs, and consideration of potential applications render it a relevant and informative reference for the study of high entropy perovskites and their thermoelectric effects.

2.13 Improvement of thermoelectric properties of lanthanum cobaltate by Sr and Mn co-substitution

In recent years, the exploration of advanced materials with tailored properties has gained substantial interest, driven by the quest for improved energy conversion technologies. High entropy perovskites, a class of complex oxides, have emerged as promising candidates for thermoelectric applications. This review delves into the study conducted by Kumar et al. that investigates the synthesis and thermoelectric effects of strontium (Sr) and manganese (Mn) co-substituted $LaCoO_3$-based polycrystalline samples, shedding light on the intricate relationship between structural modifications, electrical conductivity, and thermal properties.

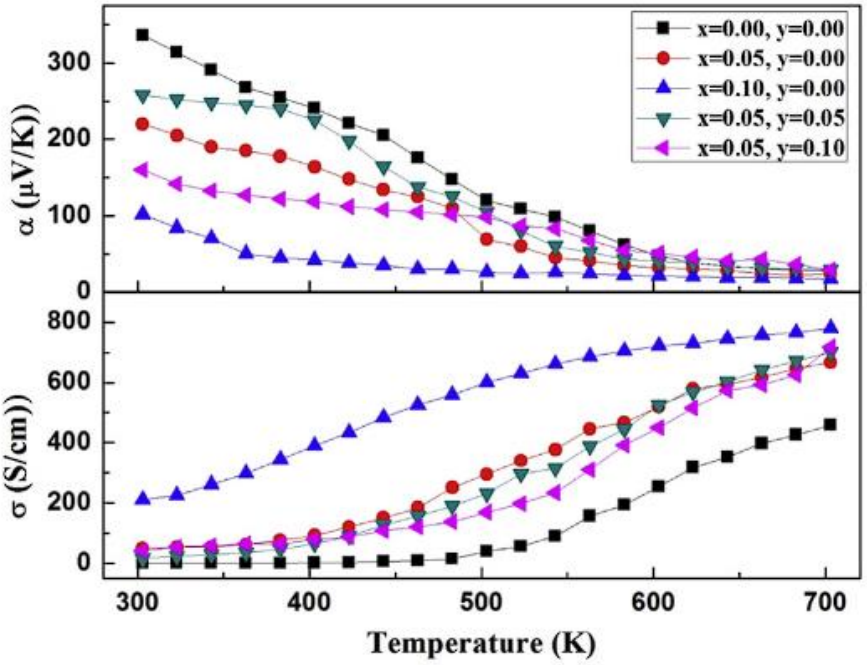

Fig 2.13 Electrical conductivity (σ) and Seebeck coefficient (α) are plotted as a function of temperature in $La_{1-x}Sr_xCo_{1-y}Mn_yO_3$ ($0.00 \leq x \leq 0.10$, $0.00 \leq y \leq 0.10$). [13]

The study begins with the preparation of Sr and Mn co-substituted LaCoO3 samples through a solid-state method, demonstrating a systematic approach towards optimizing the thermoelectric performance. Structural characterization using X-ray diffraction (XRD) and Rietveld refinement techniques provided insights into the crystal lattice and phase composition. Kumar and colleagues meticulously analyze the electrical conductivity and Seebeck coefficient of

these samples, presenting a comprehensive investigation of their behavior across varying temperature ranges.

One noteworthy observation is the unique behavior of the Seebeck coefficient, which showcases a consistent decline with increasing temperatures. This intriguing phenomenon is attributed to the impact of spin-state transitions within the material, highlighting the complex interplay between electronic properties and temperature. The authors emphasize the significance of these findings in elucidating the charge carrier dynamics and transport mechanisms operative in the high entropy perovskite system [15,16].

The thermal properties of the samples are scrutinized to uncover the contributions of phonon and electronic thermal conductivity components. Total thermal conductivity is found to exhibit an interesting trend with temperature, dominated by phonon thermal conductivity. This outcome underscores the importance of comprehending phonon interactions and lattice vibrations in influencing the overall thermal behavior of high entropy perovskites [13].

To assess the potential of these materials for thermoelectric applications, the power factor and figure of merit (ZT) are calculated. Impressively, the study reveals a distinct enhancement in the power factor and ZT values for specific compositions, namely $La_{0.95}Sr_{0.05}Co_{0.95}Mn_{0.05}O_3$. Notably, a peak ZT value of 0.14 is achieved at 480 K, emphasizing the efficacy of tailored Sr and Mn co-substitution strategies in optimizing the thermoelectric performance of high entropy perovskites [17].

The investigation by Kumar et al. offers valuable insights into the synthesis and thermoelectric effects of Sr and Mn co-substituted $LaCoO_3$-based high entropy perovskites. This study contributes to the growing body of knowledge surrounding advanced materials for energy conversion applications, and the observed enhancements in thermoelectric properties underscore the potential utility of high entropy perovskites in future energy-related technologies. The intricate correlations revealed between structural modifications, electrical conductivity, and thermal properties provide a deeper understanding of the underlying mechanisms driving thermoelectric behavior in these complex oxides.

2.14 Surface characterization of $LaCoO_3$ synthesized using citric acid

In the realm of advanced materials, the synthesis and characterization of high entropy perovskites have garnered considerable interest due to their potential for diverse applications. A notable study by Hideki Taguchi and colleagues delves into the synthesis and surface characterization of $LaCoO_3$ using citric acid as a complexing agent [14]. This work not only offers insights into the fabrication process but also sheds light on the intricate interplay between synthesis conditions, surface structure, and catalytic activity – a topic of immense relevance in the realm of high entropy perovskites.

The researchers embarked on a meticulous journey, preparing a gel through the addition of citric acid to an aqueous solution of $La(NO_3)_3 \cdot 6H_2O$ and $Co(NO_3)_2 \cdot 6H_2O$. This gel was subsequently subjected to elevated temperatures, leading to the formation of perovskite-type $LaCoO_3$. Through careful analysis, the team unearthed intriguing findings about the gel's composition at varying citric acid concentrations. Specifically, they identified a mixture of $LaCo(C_6H_5O_7)_3 \cdot NO_3$ and lanthanum nitrate in the gel prepared with 0.007 mol of citric acid, while the gel with 0.011 mol of citric acid yielded $LaCo(C_6H_5O_7)_2$. Such nuances in composition hold the key to tailoring the properties of high entropy perovskites [14].

Surface characterization played a pivotal role in unraveling the mysteries of $LaCoO_3$. Techniques like X-ray photoelectron spectroscopy (XPS) and scanning electron microscopy (SEM) enabled the researchers to discern the crystal structure, oxygen content, crystallite size, and La:Co ratio of the synthesized material. Remarkably, they observed a direct correlation between surface crystallinity and catalytic activity in CO oxidation [14].Notably, the gel fired at 600°C, containing 0.007 mol of citric acid, exhibited exceptional catalytic prowess – a testament to the intricate relationship between surface properties and performance.

This study by Taguchi and team lends itself as a valuable addition to the discourse surrounding high entropy perovskites. By investigating the synthesis, surface characterization, and catalytic behavior of $LaCoO_3$, it underscores the significance of precise fabrication methods and surface structure manipulation in achieving desirable thermoelectric effects.

2.15 Literature Review References

1. S. Jiang, J. Gild, T. Harrington, T. Hu, K. Vecchio, J. Luo, "High-Entropy ABO3 Perovskite Oxides: Synthesis, Characterization and Tolerance Factors," Scripta Materialia, 142, 116 – 120 (2018).
2. A.N. Banerjee et al., "Thermoelectric and electrical properties of dc-sputtered copper aluminum oxide thin films," Thin Solid Films 474 (2005), pp. 261–266.
3. Sarkar, S., Das, B., Midya, P. R., Das, G. C., & Chattopadhyay, K. K. (2015). Optical and thermoelectric properties of chalcogenide-based Cu2NiSnS4 nanoparticles synthesized by a novel hydrothermal route. Materials Letters, 152, 155-158.
4. Fracchia, M., Pozzi, T., Tamburini, U. A., Colombo, V., Braglia, L., & Torelli, P. (2020). Investigating CO Oxidation Mechanisms in High-Entropy Oxides with Rock-Salt Structure. The Journal of Physical Chemistry Letters, 11(9), 3589-3593. DOI: https://doi.org/10.1021/acs.jpclett.0c00602
5. Fracchia, M., Coduri, M., Manzoli, M. et al. Is configurational entropy the main stabilizing term in rock-salt Mg-Co-Ni-Cu-Zn-O high entropy oxide? Nat Commun 13, 2977 (2022).
6. Zheng, et al. "High-Entropy Perovskite Oxides for Thermoelectric Applications." J Adv Ceram (2021) 10: 377-384."
7. Zhang, P., Lou, Z., Qin, M., et al. (2022). Synthesis and thermoelectric properties of high-entropy CSBLP ceramics. Journal of Materials Science & Technology, 97, 182-189.
8. Wang, S., Huang, K., Zheng, B., Zhang, J., & Feng, S. (2013). Mild hydrothermal synthesis and physical property of perovskite Sr doped LaCrO3. Materials Letters, 101, 86-89. doi:10.1016/j.matlet.2013.03.083
9. Ding, X., Liu, Y., Gao, L., & Guo, L. (2008). Synthesis and Characterization of Doped LaCrO3 Perovskite Prepared by EDTA–Citrate Complexing Method. Journal of Alloys and Compounds, 458, 346–350.
10. Natile, M. M., Glisenti, A., Faticanti, M., Grillo, F., & Martra, G. (2007). Synthesis, Characterization, and Reactivity of Lanthanum Cobalt Oxide Perovskites in Carbon Monoxide Oxidation. Applied Catalysis B: Environmental, 72(3-4), 351–362. doi:10.1016/j.apcatb.2006.12.007

11. Kumar, A., Dragoe, D., Berardan, D., & Others. (2022). Thermal Conductivity and Thermoelectric Properties of High-Entropy Rare-Earth Cobaltates. Journal of Materiomics
12. Zhang, X., Zhang, L., Piper, L. F. J., Quackenbush, N. F., & Watson, G. W. (2015). Investigating La-Doped SrCrO3 Thin Films: Implications for High Entropy Perovskites and Thermoelectric Effects.
13. Kumar, A., Thakur, A. D., & Tomy, C. V. (2018). Synthesis and Thermoelectric Effects of High Entropy Perovskites. Journal of Alloys and Compounds, 735, 1787-1791.
14. Taguchi, H., Yamada, S., Nagao, M., Ichikawa, Y., & Tabata, K. (2002). Surface characterization of LaCoO3 synthesized using citric acid. Materials Research Bulletin, 37, 69-76. https://doi.org/10.1016/S0025-5408(01)00828-9"
15. Koshibae, W., et al. (2000). Phys. Rev. B, 62(10), 6869-6872.
16. Androulakis, J., et al. (2004). Appl. Phys. Lett., 84(10), 1099-1101.
17. Mohamed, A. E. A., et al. (2017). J. Alloys Compd., 692, 381-387.

3 Instrumentation

3.1 Characterization Techniques:

There are several different methods to characterize the sample to determine its phase, morphology, band gap, lattice vibration, crystallite size, interplanar distance, crystal plane etc. Here, in this work also these methods and machineries are being used to determine various properties of the prepared samples. There are mainly 3 types of characterization analysis that one sample can have, i.e.,

- Morphological characterization
- Phase or crystallographic characterization
- Spectroscopic characterization.

These three types of characterization techniques include a wide range of different apparatus and machineries. In this chapter major instruments and their basic working principle which were used in this project will be discussed briefly

3.1.1 Morphological Characterization:

Morphological characterization defines as the technique or method to get information about the morphology of the sample in micro and nano level. In nanotechnology, ordinary optical microscope cannot be used due to their limited focus range which is not able to get the information in nano level. Hence, the need of electron microscopes has been emerged and resulting two types of very important electron microscope, i.e., Scanning Electron Microscope (SEM) and Transmission Electron Microscope (TEM).

3.1.2 Scanning Electron Microscope (SEM):

One of the most adaptable tools for inspecting and deciphering the morphology of microstructures is the scanning electron microscope (SEM). The surface of the object is routinely scanned by a focused electron beam in a scanning electron microscope (SEM), yielding a significant number of signals. An image is produced from these electron impulses and displayed on a cathode ray tube (CRT). There are two techniques to produce the electron beam:

a) Thermionic emission; b) Field emission.

Thermal energy is used to regulate the source's electron emission to produce thermionic emission. In modern electron microscopes, field emission electron guns (FEG) are a great replacement for thermionic electron guns. Very minute topographic characteristics on the surface of whole or fragmented objects can be observed with a FESEM. Researchers in the fields of biology, chemistry, and physics utilize this technique to examine structures as small as 1 nanometer, or billionths of a millimeter. Organelles and DNA material in cells, synthetic polymers, and microchip coatings can all be studied with the FESEM.

3.1.2.1 Sample preparation for FESEM:

The specimens that can be analyzed must be compatible with high vacuum (10-5 mbar), as the SEM is operated under high vacuum. This suggests that liquids and objects made of volatile substances, like water, cannot be directly studied. To prevent contaminating the SEM specimen chamber, fine powder samples must also be firmly connected to a specimen holder substrate. A thin conductive layer must be sprayed or evaporated onto non-conductive materials before they are attached to a conductive specimen container. Common coating materials include carbon, Au, Pt, Pd, and their alloys.

3.1.2.2 Components of FESEM:

I] Electron Guns:

Modern FESEM systems require a constant electron beam from the electron cannon that has a high current, a small spot size, configurable energy, and minimal energy dispersion. A variety of electron guns are used in a FESEM system, and the quality of the electron beam produced by each differs greatly. The tungsten "hairpin" or lanthanum hexaboride (LaB6) cathodes used in the first FESEM systems have since been replaced by field emission sources, which provide more current and less energy dispersion. The longevity of the emitter is a crucial consideration when selecting electron sources.

II] Electron Lenses:

Electron beams can be concentrated by electrostatic or magnetic fields. The FESEM system, however, solely employs a magnetic field since an electron beam governed by one has less aberration. Electromagnets can be used to alter the electrons' routes.

III] Condenser Lenses:

The electron beam will diverge after passing through an anode plate from the emission source. The electron beam is brought together and collimated by the condenser lens into a nearly parallel stream. Two rotationally symmetric iron pole pieces make form a magnetic lens, and a copper winding generates the magnetic field. The center of each pole piece has a hole through which the electron beam can travel. Through a lens-gap between the two pole components, the magnetic field shapes (focuses) the electron beam. Condenser lens current can be changed to change the focus point's location.

IV] Scan Coils:

The scan coils cause the electron beam to be zigzagged as it passes over the object. The development of the image on the display and the scan movement are coordinated. The scan velocity controls both the screen's refresh rate and the amount of noise in the image. In scan coils, upper and lower coils are frequently utilized to avoid the formation of a circular shadow at low magnification.

V] Objective Lens:

The electron beam will diverge below the condenser aperture. The electron beam is de-magnified further and focused into a probe point on the specimen surface using objective lenses. The diameter of the electron beam on the specimen surface (spot size), which affects image resolution, decreases as aperture size and fundamentals of Scanning Electron Microscopy increase.

VI] Stigmator Coil:

The stigmator coils are used to rectify inconsistencies in the beam's x and y deflection, resulting in a perfectly round beam. When the beam is ellipsoidal rather than circular, the picture seems fuzzy and stretched.

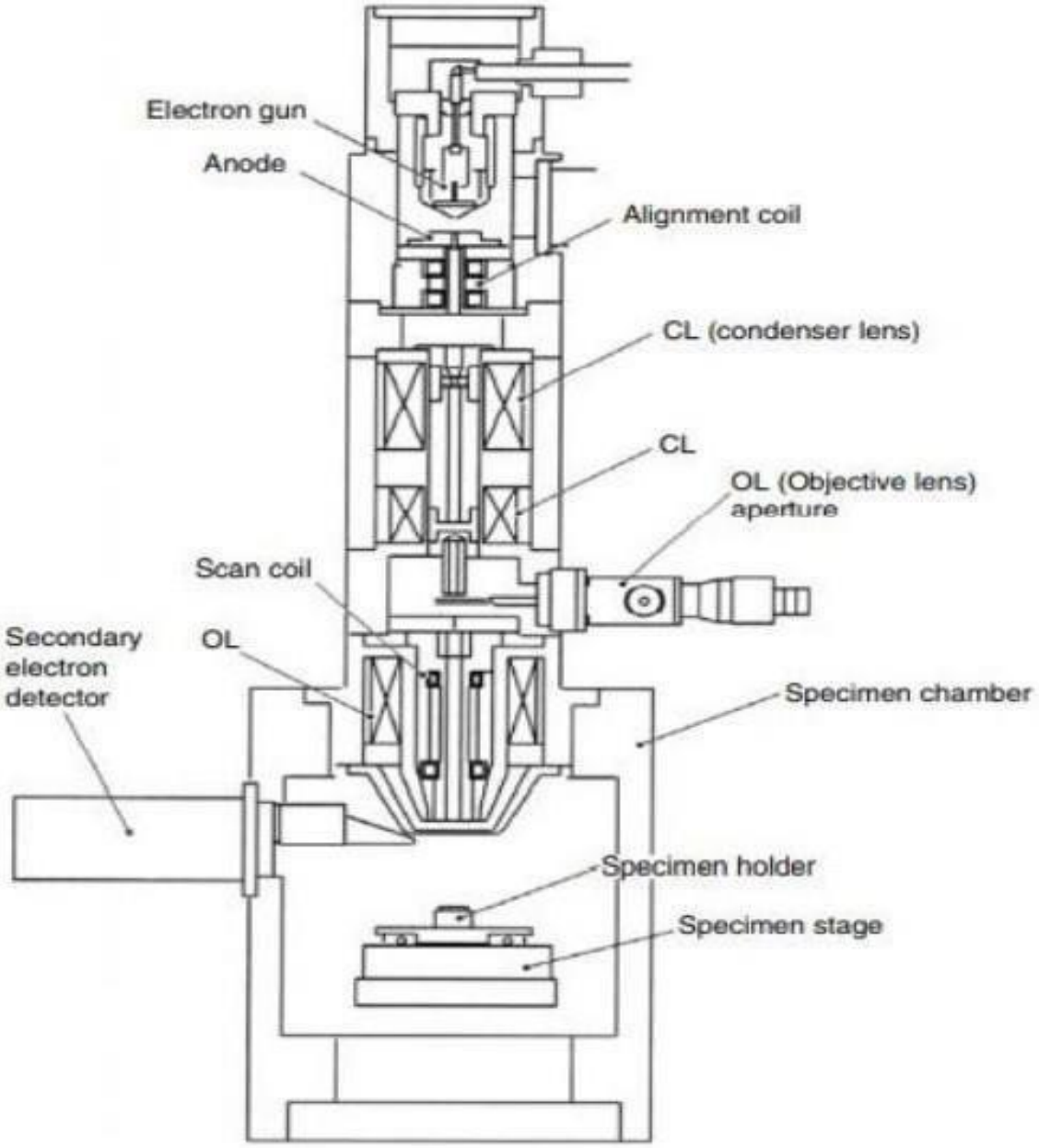

Fig 3.1 FESEM schematic diagram

VII] Object Chamber:

The object is coated with a conductive coating before being set on a particular holder. The object is anchored on a moveable stage and introduced into the high vacuum section of the microscope through an exchange chamber. The secondary electron emission detector (scintillator) is placed behind the object holder in the chamber.

VIII] Image Information:

Complex interactions take place when an electron beam impinges on a specimen surface in a FESEM and stimulates various signals for FESEM inspection. It is possible to collect and display secondary electrons, back scattered electrons (BSEs),

Fig 3.2. FESEM (Hitachi S-4800) set up

transmitted electrons, and specimen current on a monitor. To determine the specimen's composition, the excited x-ray or Auger electrons are analyzed. This part will cover the interactions of the electron beam with the specimen surface as well as the idea behind making pictures out of different signals.

3.1.3 EDAX - Energy Dispersive X-ray Analysis

Energy Dispersive X-ray Analysis (EDAX) is a powerful analytical technique widely used in material science to determine the elemental composition of a sample. It provides insights into the types and relative amounts of elements present in a material, helping researchers and scientists understand its chemical composition at a microscopic level. EDAX is often integrated with scanning electron microscopy (SEM) systems, allowing for both morphological and elemental analysis of samples.

3.1.3.1 Principle:

EDAX relies on the interaction between a high-energy electron beam and the atoms of the sample. When the electrons from the electron beam strike the sample, they displace inner-shell electrons from the atoms. As these inner-shell vacancies are filled by outer-shell electrons, characteristic X-rays are emitted. Each element has unique energy levels associated with these transitions, resulting in characteristic X-ray spectra that can be used to identify the elements present.

3.1.3.2 Instrumentation:

An EDAX setup consists of a solid-state X-ray detector, which detects and measures the energy and intensity of the emitted characteristic X-rays. The X-ray detector is connected to a spectrometer that processes the X-ray signals and produces an energy spectrum. This spectrum is known as an X-ray energy-dispersive spectrum.

3.1.3.3 Steps of Analysis:

Excitation: The electron beam from an SEM interacts with the sample, causing the emission of characteristic X-rays.

Detection: The emitted X-rays are collected by the detector in the EDAX system. The detector records the energy of the X-rays and their corresponding intensities.

Energy Spectrum: The energy spectrum obtained from the detector displays peaks at specific energy levels corresponding to the characteristic X-rays emitted by the elements present in the sample.

Identification: By analyzing the peaks in the energy spectrum and comparing them to known characteristic X-ray energies for different elements, the composition of the sample can be determined.

3.1.3.4 Advantages:

Elemental Mapping: EDAX can provide elemental maps of samples, showing the distribution of different elements across the surface. This aids in understanding the spatial distribution of elements within a material.

Non-Destructive: The analysis is non-destructive, making it suitable for a wide range of materials, including delicate or valuable samples.

Qualitative and Quantitative Analysis: EDAX can be used for both qualitative identification of elements and quantitative determination of their concentrations.

Microanalysis: EDAX can analyze minute sample areas, making it ideal for investigating localized areas within a material.

3.1.3.5 Applications:

EDAX finds applications in various fields, including metallurgy, geology, electronics, materials research, and more. It is used for characterizing materials, identifying unknown substances, studying crystallography, and investigating the elemental composition of complex samples.

3.1.4 X-Ray Diffraction (XRD):

X-rays are a form of electromagnetic radiation that has high energies and short wavelengths on the order of the atomic spacing for solids. When a beam of x-rays impinges on a solid material, a portion of this beam will be scattered in all directions by the electron associated with each atom or ion that lies within the beam's pathway.

Let us now examine the necessary conditions for diffraction of X-rays by a periodic arrangement of atoms. Diffraction occurs when a wave encounters a series of regularly spaced obstacles that are capable of scattering the wave and have spacing that are comparable in magnitude to the wavelength. Furthermore, diffraction is a consequence of specific phase relationships established between two or more waves that have been scattered by the obstacles. The phase relationship between the scattered waves, which will depend upon the difference in path length is important. One possibly results when its pathway length is an integral number of wavelengths.

3.1.4.1 Bragg's Law

Considering the two parallel planes of atoms, which have the same h, k and l Miller indices and are separated by the interplanar spacing d. Now assuming a parallel, monochromatic and coherent (in-phase) beam of x-rays of wavelength λ is incident on these two planes at an angle of Θ. Two rays in this beam are scattered by atoms A and B. Constructive interference of the scattered waves occur also an angle of Θ to the planes, if the path length difference (i.e., CB+BD) between these waves is equal to a whole number, n, of wavelengths.

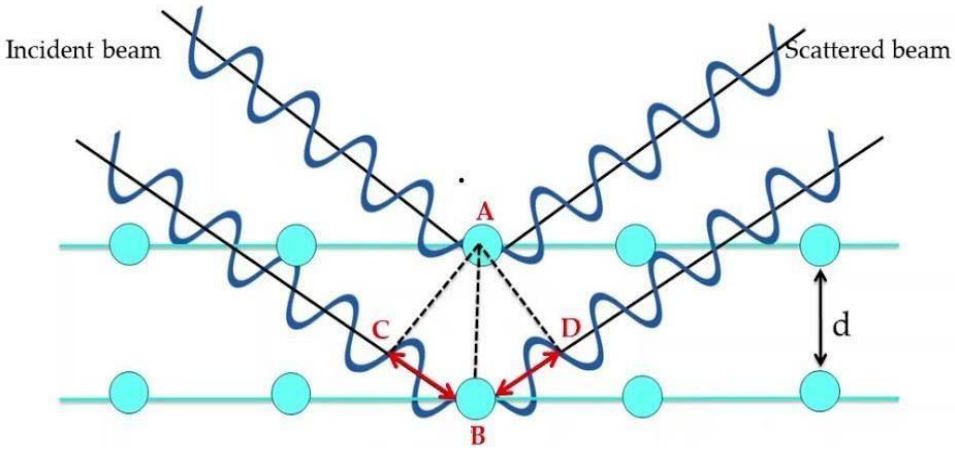

Fig 3.3 Bragg's Law

So, the condition for diffraction is

$n\lambda = CB + BD$

or, $n\lambda = d \sin\Theta + d \sin\Theta$

or, $n\lambda = 2d \sin\Theta$. (26)

3.1.4.2 Production of X-ray:

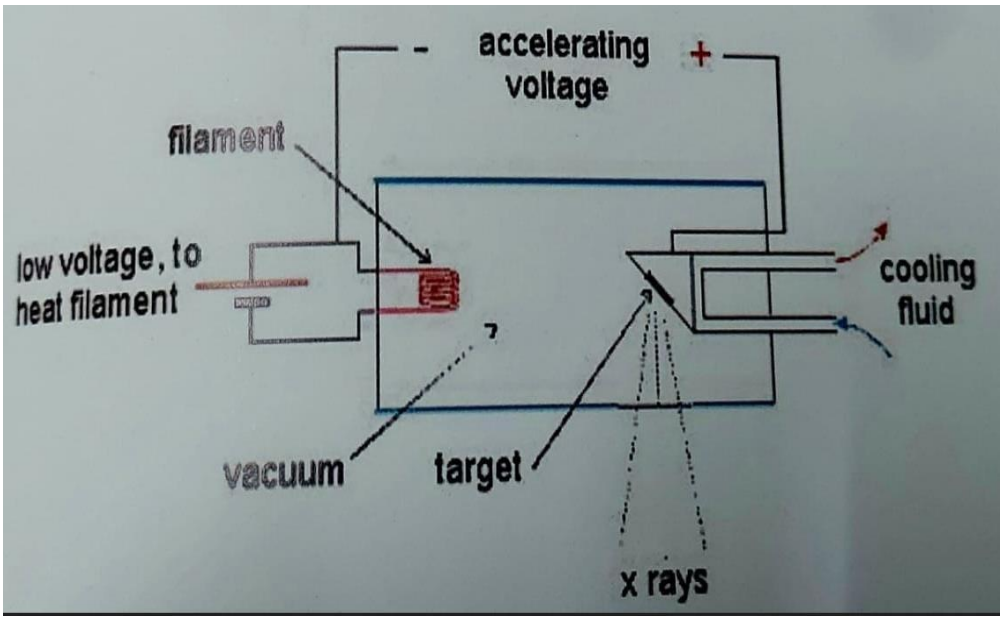

Fig 3.4 X ray gun schematic

X-rays are produced by bombarding a metal target (e.g., Cu, Mo usually) with a beam of electrons emitted from a hot filament (often tungsten). The incident beam will ionize electrons from the K-shell (1s) of the target atom and X-rays are emitted as the resultant vacancies are filled by electrons dropping down from the L (2p) or M (3p) levels. This gives rise to Kα and Kβ lines.

3.1.4.3 Instrumentation:

An XRD setup typically includes:

- X-ray Source: Produces a monochromatic X-ray beam, often using a metal target, such as copper or cobalt.
- Sample Holder: Holds the sample in a fixed orientation.
- Goniometer: Rotates the sample and detector to different angles.
- Detector: Measures the intensity of diffracted X-rays at different angles.

- Data Analysis Software: Analyzes the diffraction data to determine the crystal structure.

Fig 3.5 XRD setup "D8 Advance Bruker"

3.1.4.4 Particle Size determination by Scherrer's formula:

Experimentally obtained diffraction patterns of the sample are compared with the standard powder diffraction files published by the JCPDS. The average grain size of the samples was calculated using Scherrer's formula:

$$D = \frac{K\lambda}{\beta \cos \theta} \tag{27}$$

- D is the average crystallite size (crystalline domain size) in nanometers (nm).
- K is the Scherrer constant, which is a dimensionless constant that depends on the shape of the crystallites. For spherical crystallites,
- K is often taken as 0.9.

- λ is the wavelength of the X-ray used for the analysis, typically in angstroms (A˚).
- β is the full width at half maximum (FWHM) of the diffraction peak in radians.
- θ is the Bragg angle, which is the angle at which the X-rays are incident on the sample, and it corresponds to the diffraction peak position.

It is important to realize that the Scherrer's formula provides a lower bound on the particle size. The reason behind this is that a variety of factors can contribute to the width of a diffraction peak; besides particle size, the most important of these are actually is dependent on the factors like inhomogeneous strain and instrumental errors. If all of these other factors contributing to the peak width were zero, then the peak width would be determined solely by the particle size and the Scherrer's formula would apply.

3.1.4.5 Applications:

- XRD analysis has numerous applications:
- Material Identification: Identifying unknown crystalline substances by matching their diffraction patterns to reference patterns.
- Phase Analysis: Determining the phases present in a sample mixture.
- Crystal Structure Determination: Determining the arrangement of atoms in a crystal lattice.
- Stress Analysis: Evaluating residual stresses within materials.
- Texture Analysis: Studying the preferred orientation of crystallites in a material.
- Quantitative Analysis: Measuring the number of phases present in a mixture.

3.1.5 Diffused Reflectance Spectroscopy (DRS)

Diffused Reflectance Spectroscopy (DRS) is a technique used in ultraviolet-visible (UV-Vis) spectroscopy to investigate changes in the reflectance of a material as a function of wavelength or energy. Unlike traditional absorption spectroscopy, which measures the decrease in intensity of transmitted light, DRS focuses on variations in the intensity of reflected light.

3.1.5.1 Principle:

DRS is based on the principle that the reflectance of a material changes when it absorbs light. The reflectance spectrum obtained from DRS provides information about the energy levels and electronic transitions within the material. DRS is particularly useful for studying materials that are not transparent or difficult to prepare as thin films for transmission measurements.

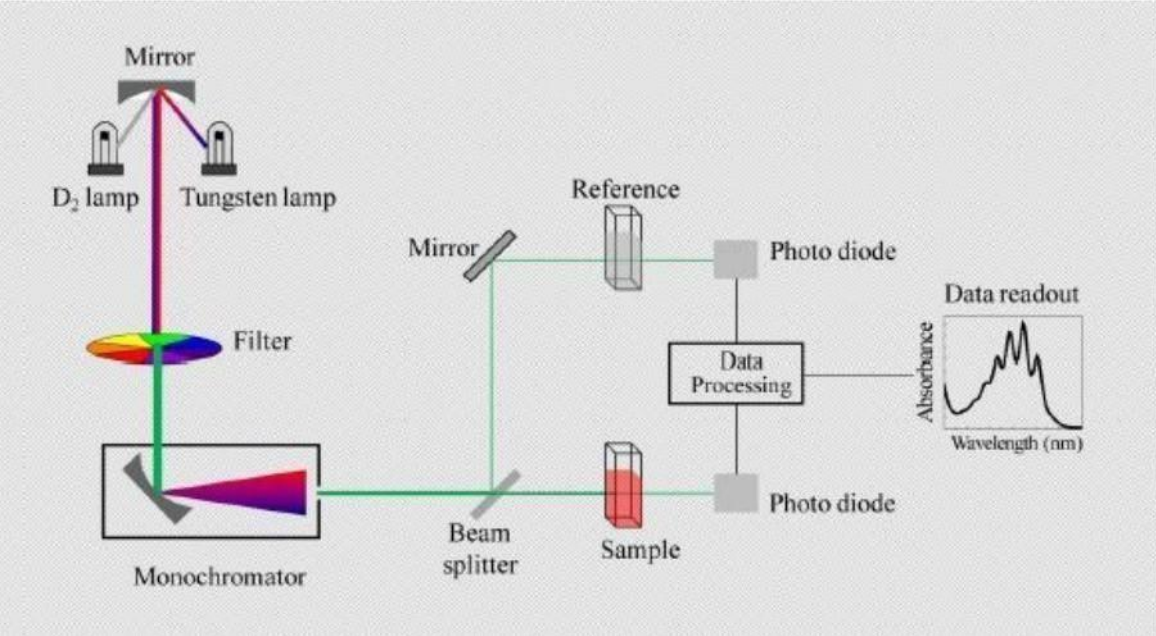

Fig 3.6 Basic working principle of UV-Vis spectroscopy

The spectrometer beam is directed into the sample, where it is reflected, dispersed, and transmitted through the sample material, resulting in diffuse reflectance. The accessory collects the back reflected, diffusely dispersed light (part of which is absorbed by the sample) and directs it to the detector optics. Diffuse reflection refers to the portion of a beam that is dispersed within a sample and returns to the surface.

Particle size, refractive index, homogeneity, and packing are further parameters that contribute to excellent spectral quality in diffuse reflectance sampling. The raw diffuse reflectance spectra will seem different from its transmission counterpart despite all of these sample preparation techniques (stronger than expected absorption from weak IR bands).

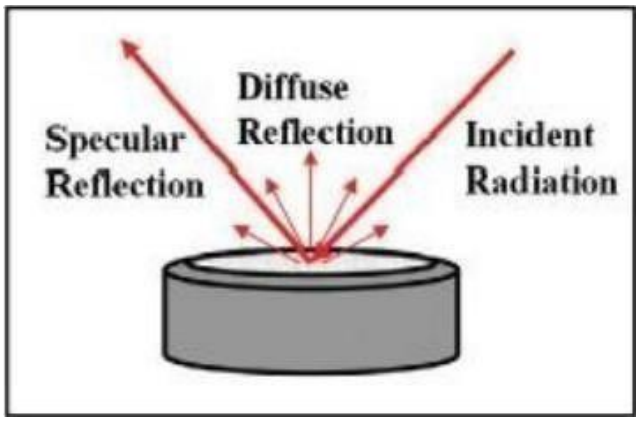

Fig 3.7 Diffuse and Specular Reflectance

To correct for these discrepancies, a Kubelka-Munk conversion can be performed to a diffuse reflectance spectrum.

Kubelka-Munk Function: $$\boldsymbol{F(R) = \frac{(1-R)^2}{R} = \frac{k}{s}} \quad (28)$$

Fig 3.8 UV-VIS-NIS (SHIMADZU UV-3600) Spectrophotometer

R stands for the sampled layer's absolute reflectance, k for the molar absorption coefficient, and s for the scattering coefficient.

3.1.5.2 Steps of Analysis

Baseline Measurement: A reference material is measured to establish a baseline reflectance spectrum. This baseline is used to normalize the measurements.

Sample Measurement: The sample's reflectance spectrum is measured over a specific wavelength or energy range.

Diffused Reflectance Calculation: The diffused reflectance (ΔR/R) is calculated by subtracting the baseline reflectance from the sample reflectance and then dividing by the baseline reflectance:

$$\frac{\Delta R}{R} = \frac{R_{sample-}R_{baseline}}{R_{baseline}} \quad (29)$$

Analysis and Interpretation: The diffused reflectance spectrum provides insights into electronic transitions, energy levels, and bandgap characteristics of the material.

3.1.5.3 Applications:

- DRS is particularly useful for studying semiconductors, photovoltaic materials, and materials with complex optical properties. Some applications include:
- Characterizing bandgap energies and electronic transitions.
- Investigating changes in materials due to chemical reactions or phase transitions.
- Identifying surface states and defects in materials.

3.1.5.4 Advantages:

- Non-destructive analysis.
- Suitable for a wide range of materials, including powders, films, and bulk materials.
- Provides information about electronic transitions and bandgap characteristics.

3.1.5.5 Limitations:

- Requires careful baseline correction to ensure accurate results.
- May not be as sensitive as other techniques for detecting weak transitions.
- Can be affected by surface roughness and scattering effects

3.1.6 Fourier Transform Infra-Red Spectroscopy (FTIR):

Fourier Transform Infrared (FT-IR) Spectroscopy is a powerful analytical technique used to identify and analyze the molecular composition of materials based on their absorption or emission of infrared radiation. FT-IR spectroscopy is widely used in chemistry, materials science, pharmaceuticals, and various industries to investigate the functional groups and chemical bonds present in samples.

Infrared spectroscopy involves passing IR radiation through a sample. The sample absorbs some of the infrared radiation and passes some of it through (transmitted).

3.1.6.1 Principle

FT-IR spectroscopy is based on the principle that molecules absorb specific frequencies of infrared light that correspond to the vibrational modes of their chemical bonds. When infrared light passes through a sample, some of it is absorbed by the sample's molecules, causing them to vibrate and change their energy states. By measuring the absorbed or transmitted light, it's possible to obtain a unique "fingerprint" spectrum that reveals information about the molecular structure of the sample.

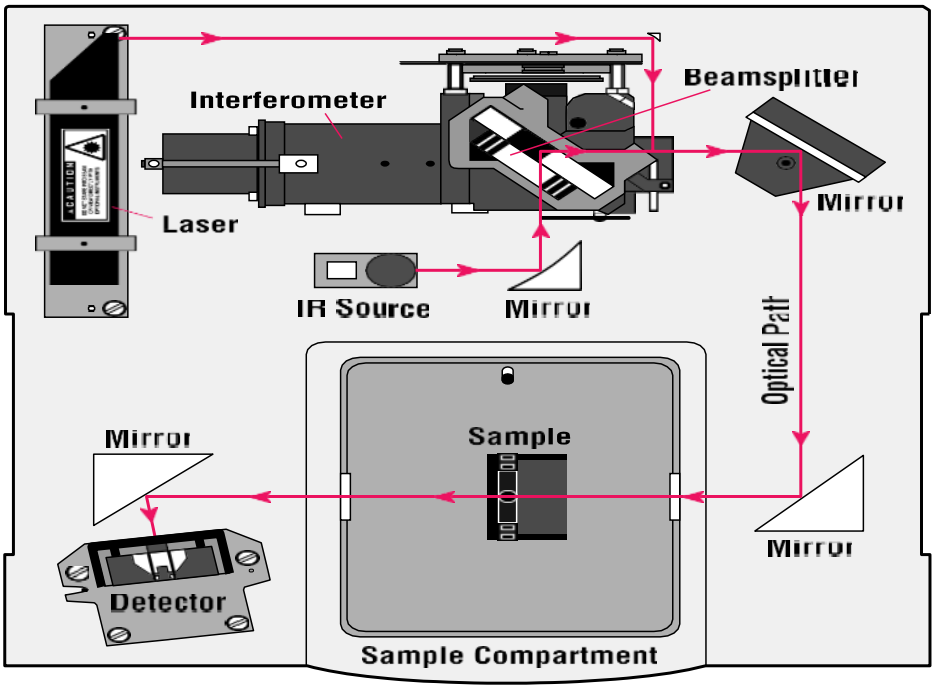

Fig 3.9 A simple spectrometer layout

3.1.6.2 Instrumentation

- A typical FT-IR spectrometer consists of:
- Infrared Source: Provides a broad range of infrared wavelengths.
- Interferometer: Splits the incoming infrared beam into two paths, one that interacts with the sample and another that acts as a reference.
- Sample Compartment: Holds the sample for analysis.
- Detector: Measures the intensity of the infrared radiation after it interacts with the sample and reference beams.
- Computer and Software: Converts the raw interferogram data into a final infrared spectrum.

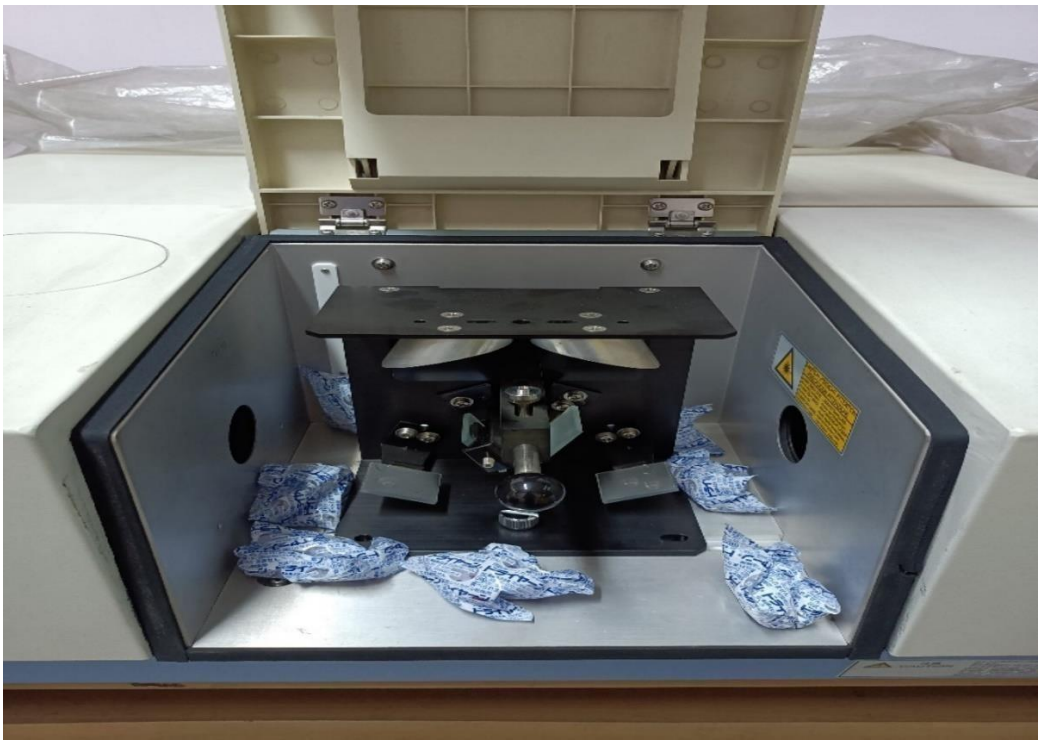

Fig 3.10 Internal components of FTIR instrument.

3.1.6.3 Steps of Analysis:

- Interferogram Generation: The interferometer splits the incoming infrared beam into sample and reference beams. The two beams recombine, resulting in an interferogram, which is a plot of intensity versus time.

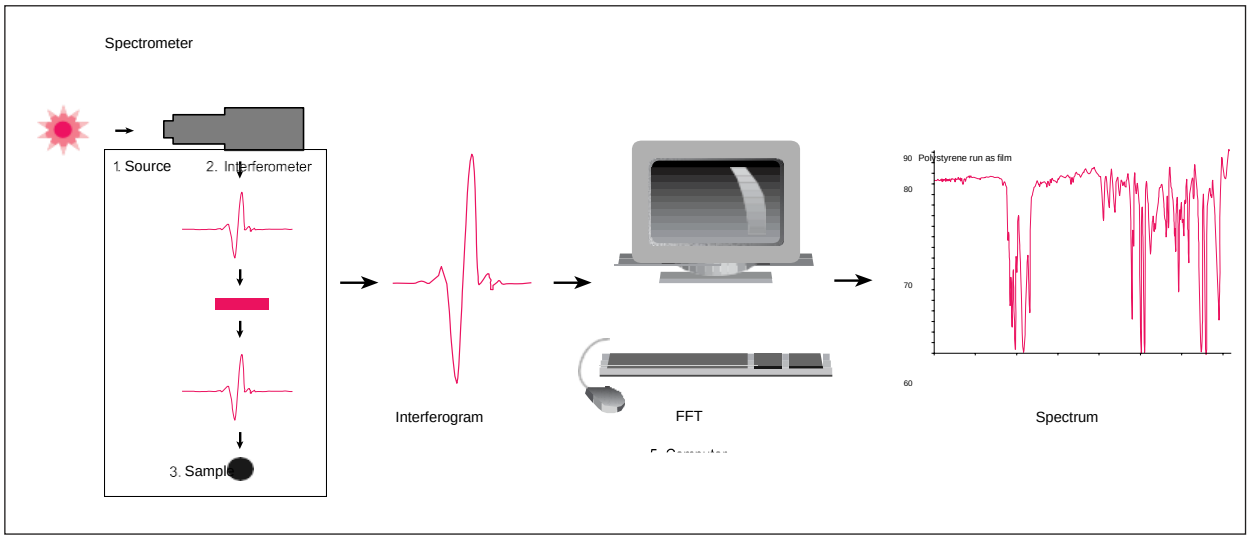

Fig 3.11 Process of generating an FTIR spectra

- Data Acquisition: The interferogram is converted into an interferogram data set by the detector. This data set is a time-domain representation of the absorption spectrum.
- Fourier Transform: The Fourier transform mathematically converts the interferogram from the time domain to the frequency domain. This transformation produces the final FT-IR spectrum, which is a plot of intensity versus wavenumber (or wavelength).
- Spectrum Interpretation: Peaks and bands in the FT-IR spectrum correspond to vibrational modes of functional groups in the sample. Analysis of the spectrum allows for the identification of bonds and groups within the molecule.

3.1.6.4 Applications:

FT-IR spectroscopy has numerous applications:

- Chemical Identification: Identifying unknown compounds by comparing their FT-IR spectra to reference spectra.
- Structural Analysis: Determining the types of chemical bonds present in a sample.
- Quality Control: Monitoring the composition of materials in various industries.
- Pharmaceutical Analysis: Investigating drug formulations and interactions.
- Environmental Analysis: Detecting pollutants and contaminants in environmental samples.

3.1.6.5 Advantages:

- Non-destructive analysis.
- Provides information about molecular composition and functional groups.
- Requires minimal sample preparation for most materials.

3.2 Instruments Used in Sample Synthesis

3.2.1 Electronic Weighing Balance

Fig3.12 Electronic Balance

An electronic weighing balance, commonly referred to as an electronic scale or digital scale, is a precision measuring device used to determine the mass or weight of an object. It utilizes electronic components and sensors to provide accurate and quick measurements of weight. Electronic weighing balances are widely used in various industries, laboratories, commercial settings, and even in households for various applications.

3.2.2 Magnetic Stirrer

A magnetic stirrer is a laboratory device used to mix or stir liquids using a rotating magnetic field. It is a common tool in various scientific disciplines, including chemistry, biology, and physics, where precise and consistent mixing of liquids is required.

Magnetic stirrers are particularly useful when working with solutions that need to be mixed gently or continuously over extended periods.

3.2.2.1 Components and Working Principle:

A magnetic stirrer consists of several main components:

Fig 3.13 Magnetic Stirrer, Remi 2MLH Model

- Stirring Plate: The base of the magnetic stirrer typically contains a flat, circular platform made of materials such as glass-ceramic or aluminum. The stirring plate is where the containers holding the liquids are placed.
- Stir Bar (Flea): A small, cylindrical or octagonal bar made of a magnetic material, such as PTFE (polytetrafluoroethylene) or coated with a non-reactive material like PTFE. The stir bar is placed inside the liquid to be mixed.
- Magnetic Field Generator: Beneath the stirring plate, there is a magnetic field generator, usually an electromagnet. This generator produces a rotating magnetic field that interacts with the magnetic stir bar.

- It also has heating functionality; however, temperature needs to be monitored manually using thermometers.

3.2.3 Agate Mortar and Pestle

An agate mortar and pestle are specialized laboratory tools used for grinding, mixing, and crushing materials, especially in applications where avoiding contamination is crucial. Agate is a type of semi-precious gemstone known for its hardness and non-reactive properties. The mortar is made from a single piece of agate, carved into a bowl-like shape with a smooth and non-porous interior surface. Agate is chosen for its hardness and resistance to chemical interactions, ensuring that it doesn't react with the substances being processed. The interior surface is polished to a fine finish, allowing for efficient grinding while minimizing the risk of contamination.

Fig 3.14 Agate Mortar and Pestle.

3.2.4 Laboratory thermometer

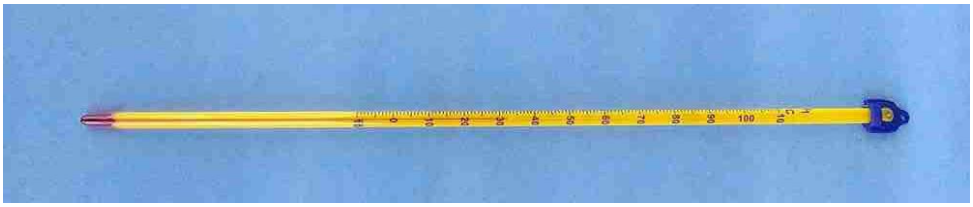

Fig 3.15 Laboratory thermometer

A laboratory thermometer is a precision measuring instrument used to measure temperature in laboratory settings. Laboratory thermometers are designed to provide accurate and reliable temperature measurements, often with higher precision and broader temperature ranges.

3.2.5 Oven

A drying oven, also known as a lab oven or drying chamber, is a specialized piece of laboratory equipment used for drying, sterilizing, curing, and other heat-related processes. It provides a controlled environment with consistent temperature and often precise humidity levels for various laboratory applications. Drying ovens are commonly used in research and industrial settings where controlled heating and drying are essential.

Fig 3.16 Oven

3.2.5.1 Features and Components:

Heating Element: Drying ovens are equipped with heating elements that generate the necessary heat to raise the temperature inside the chamber.

Temperature Control System: A temperature control system, often equipped with a digital display and programmable settings, allows users to set and maintain the desired temperature.

Fig 3.17 PID controller of Oven

3.2.6 Furnace

A furnace is a high-temperature heating device used in various industrial, scientific, and manufacturing processes. It is designed to generate controlled heat and maintain specific temperature conditions for tasks such as heating, annealing, sintering, melting, and thermal testing. Furnaces are essential tools in industries like metallurgy, ceramics, materials science, and more, where precise and controlled high-temperature environments are required.

Fig 3.18 Furnace used for synthesis of samples

Here, a muffle furnace is used. Muffle furnaces have a separate heating chamber (muffle) within the main chamber, providing additional protection for samples. The furnace used here can be used up to 1100 degree Celsius, with programmable heating hate.

3.2.7 Spin coater

The Spin NX-G is a specialized spin coater machine designed for coating substrates with thin films of liquids, typically used in applications such as thin-film deposition, microfabrication, and surface engineering. Spin coaters are commonly used in laboratories, research institutions, and industries where precise and uniform coatings are required on substrates like wafers, glass slides, and other flat surfaces.

Fig 3.19 Spin Coater Model Spin NX-G

3.2.8 Ultrasonic homogenizer

A sonicator, also known as an ultrasonic homogenizer or ultrasonic cleaner, is a versatile laboratory device that uses high-frequency sound waves (ultrasonic waves) to perform various processes such as mixing, dispersing, emulsifying, degassing, and cleaning. Sonicators are commonly used in laboratories, research facilities, and industries for a wide range of applications across different fields.

Sonication involves the generation of ultrasonic waves through a transducer. The transducer converts electrical energy into high-frequency mechanical vibrations, typically in the range of 20 kHz to several megahertz.

Fig 3.20 Ultrasonic homogenizer

These vibrations are transmitted into the liquid or sample being processed, creating pressure waves that lead to the formation and collapse of tiny bubbles (cavitation) in the liquid. The phenomenon of cavitation generates localized high temperatures and pressures, causing physical and chemical effects that aid in various processes.

3.2.9 Pelletizer

A pelletizer is a mechanical device used in various industries to transform materials into small, pellet-shaped particles. Pelletization involves compacting and shaping raw materials into small, uniform pellets that are easier to handle, transport, and store. Pelletizers are employed in industries such as agriculture, food processing, pharmaceuticals, chemicals, and plastics to create pellets from a wide range of materials.

Material Feeding: Raw material in various forms, such as powders, flakes, or even liquids, is fed into the pelletizer.

Compaction: The material is subjected to pressure, which compacts and binds the particles together. This pressure can be applied through rollers, extrusion screws, or other mechanisms.

Shaping: The compacted material is shaped into small pellets using a die or mold. The die determines the size and shape of the pellets.

Disk Pelletizer: Uses a rotating disc to tumble and agglomerate material into pellets.

The die used in a pelletizer is a crucial component responsible for shaping the raw material into uniform pellet shapes. The die determines the size, shape, and sometimes the density of the pellets produced by the pelletizer. The design of the die depends on the specific application, the characteristics of the material being pelletized, and the desired properties of the final pellets.

Fig 3.21 Pelletizer

3.3 Instruments used in Testing/measurements

3.3.1 Multimeter

Fig 3.22Multimeter

A multimeter, also known as a multimeter or VOM (volt-ohm-milliammeter), is a versatile electronic instrument used to measure various electrical quantities such as voltage, current, resistance, and sometimes other parameters like capacitance, frequency, and temperature. Multimeters are essential tools for both professionals and hobbyists working in electronics, electrical engineering, and related fields. Analog Multimeters: These traditional multimeters use a mechanical movement, often a pointer or needle, to display measurements on a scale. They are known for their simplicity and durability. Analog multimeters can measure DC (direct current) and AC (alternating current) voltage, current, and resistance. However, they tend to be less precise and have a slower response compared to digital multimeters.

Digital Multimeters (DMMs): Digital multimeters have largely replaced analog ones due to their accuracy and ease of use. They display measurements as numerical values on a digital screen. DMMs offer a wide range of functions, including voltage (DC and AC), current (DC and AC), resistance, continuity, diode testing, capacitance, frequency, and sometimes temperature.

They provide greater precision and often come with auto-ranging capabilities, which means they automatically select the appropriate measurement range for the given input.

3.3.2 Custom made vacuum chamber

In this chamber, the substrate containing sample is subjected to differential temperature at the free ends and thermoelectric data are collected using PT-DAQ setup

Fig 3.23 Vacuum Chamber

3.3.3 Variable AC Source

A variable AC source, also known as a variable AC power supply or adjustable AC power source, is an electrical device that provides an adjustable output of alternating current (AC) voltage, frequency, and sometimes phase angle. Variable AC sources are used for testing, calibration, and experimentation in various industries, including electronics, electrical engineering, research, and manufacturing. Here it is used to operate heating element which is used to heat the substrate.

Fig 3.24 Variable AC Source for heater element

3.4 References

1. Z. Yang, Z. Z. Ye, Z. Xu and B. H. Zhao, “Effect of the Morphology on the Optical Properties of ZnO Nanos tructured,” Physica E: Low-Dimensional Systems and Nanostructures, Vol. 42, No. 2, December 2009, pp. 116- 119. doi: 10.1016/j.physe.2009.09.010.

2. Thermo Nicolate, Introduction to Fourier Transform Infrared Spectrometry, © 2001 Thermo Nicolet Corporation.

3. Kortüm, G. Reflectance Spectroscopy: Principles, Methods, Applications; Kortüm, G., Ed.; Springer: Heidelberg/Berlin, Germany, 1969.

4. Frei, R.W.; Frodyma, M.M.; Lieu, V.T. Diffuse reflectance spectroscopy. In Instrumentation for Spectroscopy. Analytical Atomic Absorption and Fluorescence Spectroscopy. Diffuse Reflectance Spectroscopy; Svehla, G., Ed.; Wilson & Wilson’s Comprehensive Analytical Chemistry; Elsevier Scientific Publishing Company: Amsterdam, The Netherlands, 1975; Volume 4, Chapter 3, pp. 263–345.

5. Höpe, A. Diffuse Reflectance and Transmittance. In Spectrophotometry: Accurate Measurement of Optical Properties of Materials; Germer, T.A., Zwinkels, J.C., Tsai, B.K., Eds.; Experimental Methods in the Physical Sciences; Academic Press Elsevier Inc.: Amsterdam, The Netherlands, 2014; Volume 46, Chapter 6, pp. 179–219.

6. Lambert, J.H. Lambert’s Photometrie. Photometria Sive De Mensura Et Gradibus Luminis, Colorum et Umbrae (1760); Anding, E., Ed.; Ostwald’s Klassiker der exakten Wissenschaften; Verlag von Wilhelm Engelmann: Leipzig, Germany, 1892; Volume 31.

7. Bouguer, P. Traité d’optique sur la gradation de la lumiere; I’Abbé de la Caille, M., Ed.; De l’Imprimerie de H.L. Guerin & L.F. Delatour: Paris, France, 1760.

8. Ångström, K. Ueber die Diffusion der strahlenden Wärme von ebenen Flächen. Ann. Phys. 1885, 262, 253–287.

9. Messerschmitt, J.B. Ueber diffuse Reflexion. Ann. Phys. 1888, 270, 867–896.

10. Seeliger, H. Zur Photometrie zerstreut reflectirender Substanzen. In Sitzungsberichte der Mathematisch-Physikalischen Classe der k. b. Akademie der Wissenschaften zu München; Franz, G., Ed.; Verlag der K. Akademie: Munich, Germany, 1888; Volume 18, pp. 201–248.

11. Lommel, E. Die Photometrie der diffusen Zurückwerfung. Ann. Phys. 1889, 272, 473–502.

12. Uljanin, W. Ueber das Lambert'sche Gesetz und die Polarisation der schief emittirten Strahlen. Ann. Phys. 1897, 298, 528–542.

13. Wright, H. Die diffuse Reflexion des Lichtes an matten Oberflächen. Ann. Phys. 1900, 306, 17–41.

14. Pokrowski, G.I. Zur Theorie der diffusen Lichtreflexion. Z. Phys. 1924, 30, 66–72.

15. Schulz, H. Untersuchungen über die Reflexion a teilweise lichtzerstreuenden Flächen. Z. Phys. 1925, 31, 496–506.

16. Harrison, V.G.W. The light-diffusing properties of magnesium oxide. Proc. Phys. Soc. 1946, 58, 408–419.

17. Torrent, J.; Barrón, V. Diffuse Reflectance Spectroscopy. In Methods of Soil Analysis Part 5–Mineralogical Methods; Number 5 in the Soil Science Society of America Book Series; Ulery, A.L., Drees, L.R., Eds.; Soil Science Society of America Inc.: Madison, WI, USA, 2008; Volume 5, Chapter 13, pp. 367–385.

18. Blake, T.A.; Johnson, T.J.; Tonkyn, R.G.; Forland, B.M.; Myers, T.L.; Brauer, C.S.; Su, Y.F.; Bernacki, B.E.; Hanssen, L.; Gonzalez, G. Methods for quantitative infrared directional-hemispherical and diffuse reflectance measurements using an FTIR and a commercial integrating sphere. Appl. Opt. 2018, 57, 432–446.

19. Clarke, F.J.J.; Compton, J.A. Correction Methods for Integrating-Sphere Measurement of Hemispherical Reflectance. Color Res. Appl. 1986, 11, 253–262.

20. Kortüm, G.; Braun, W.; Herzog, G. Prinzip und Meßmethodik der diffusen Reflexionsspektroskopie. Angew. Chem. 1963, 75, 653–661.

21. Hanssen, L. Integrating-sphere system and method for absolute measurement of transmittance, reflectance, and absorptance of specular samples. Appl. Opt. 2001, 40, 3196–3204. [PubMed]

22. Jacquez, J.A.; McKeehan, W.; Huss, J.; Dimitroff, J.M.; Kuppenheim, H.F. An Integrating Sphere for Measuring Diffuse Reflectance in the Near Infrared. J. Opt. Soc. Am. 1955, 45, 781–785.

23. Goebel, D.G.; Caldwell, B.P.; Hammond, H.K. Use of an Auxiliary Sphere with a Spectro reflectometer to Obtain Absolute Reflectance. J. Opt. Soc. Am. 1966, 56, 783– 788.

4 Prototypical Customized Thermoelectric Measurement Data Acquisition System (PT-DAQ)

4.1 Need of PT-DAQ

In order to investigate thermoelectric effect of samples, it required measurement of temperatures of cold and hold junctions and electromotive force(emf) between the region with temperature differences. The temperature data and emf data recorded should be coherent and multiple readings needed to be made. The process involved taking data at regular intervals over a period of time. The substrate was heated from one end using heater, and cooled from other end by placing over platform with ice beneath which acted as heat sink. The substrate, heater, thermocouples and heat sink, all placed inside a custom-made vacuum chamber. The connecting wires for heater, thermocouples and emf measurement leads out of chamber via outlets. Hence, we needed a device which would sit outside the chamber and record data via connects. The device also needed to be highly precise for accurate measurements of temperature over wide range and voltage in order of microvolts. The data collected would be used to calculation of Seebeck effects with high precision. So, the main reasons why we needed PT-DAQ are, precision, convenience, tailored productivity, data sampling ability and efficient as a measurement tool with automated functioning.

4.2 Planning for PT-DAQ

In order to achieve all points mentioned above, and also record data over a period of time with periodic intervals, a device was designed using a microcontroller, Arduino Nano, with couple analog-to-digital convertors (ADCs), real time clock (RTC), SD card module, buck convertor (step down dc transformer) for 5V DC supply and k-type thermocouples were needed for the apparatus named Prototypical Measurement Data Acquisition System or PT-DAQ as abbreviation. The device could be powered using usb port present in Arduino Nano or the power supply from buck convertor. Since automation was one of the key goals, hence continuous operation with easy on/off features were achieved by connected the supply via buck convertor, which along with SD card

module also enabled the device to be operated from anywhere without the need of being connected to a laptop/ USB power source system.

All the components were chosen, and soldered on a stripboard to design the prototype. After proper connections been made, the system was kept in an insulated pvc box for safety of delicate components and insulation from external sources.

4.3 Various Components of PT-DAQ

4.3.1 Arduino Nano Board

The Arduino Nano is a compact and versatile microcontroller board that is part of the Arduino ecosystem. It's designed for projects that require a balance between size and performance.

Fig 4.1 Arduino Nano Board

Its main features include,

- Microcontroller: The Arduino Nano is powered by an Atmel ATmega328P microcontroller, which is based on the AVR architecture. It operates at a clock frequency of 16 MHz and has 32KB of flash memory for storing your program code.
- Communication Interfaces: The Nano comes equipped with UART, SPI, and I2C communication interfaces, making it easy to connect to other devices such as sensors, displays, and communication modules.
- Memory and Storage: Aside from the 32KB of flash memory, the ATmega328P chip on the Nano has 2KB of SRAM for data storage and 1KB of EEPROM for non-volatile memory storage.

- Programming: The Nano can be programmed using the Arduino Integrated Development Environment (IDE), which provides a user-friendly interface for writing, compiling, and uploading code to the board. Arduino programming language, which is based on C and C++, is commonly used for writing sketches (programs).
- Power Supply: The board can be powered via USB or an external power source (typically 7-12V DC). It features a built-in voltage regulator that provides a stable 5V supply for the microcontroller and other components.
- Form Factor: The Nano's small form factor (approximately 45mm x 18mm) makes it suitable for projects with space constraints. It can be easily integrated into various applications and prototypes.
- Versatility: Arduino Nano is used in a wide range of projects including robotics, IoT devices, sensor networks, wearable electronics, and more. Its compact size and extensive features make it an excellent choice for both beginners and experienced electronics enthusiasts.
- Open-Source: Arduino Nano, like other Arduino boards, is based on open-source hardware and software principles. This means that the design files, schematics, and software libraries are freely available, allowing for customization and modification.

4.3.2 Hx711 ADC

ADC stands for Analog-to-Digital Converter. It's an electronic component or subsystem that converts analog signals, which are continuous voltage or current variations, into digital signals composed of discrete binary values (usually 0s and 1s). This conversion process allows analog signals to be processed, stored, and manipulated by digital systems such as microcontrollers, computers, and digital signal processors.

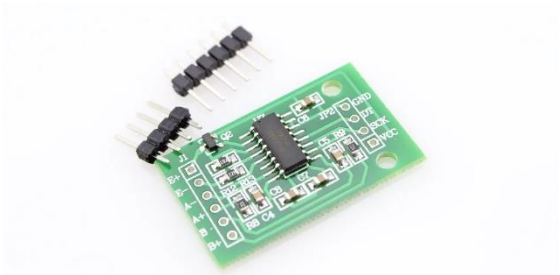

Fig 4.2 Hx711 ADC

Sampling: The first step of the conversion process is sampling. The continuous analog signal is sampled at specific intervals to capture its voltage or current values at discrete points in time. The rate at which the signal is sampled is known as the sampling rate or sampling frequency.

Quantization: The sampled analog values are then quantized, meaning they are mapped to a finite number of discrete digital values. The number of possible digital values depends on the resolution of the ADC. For example, an ADC with 8-bit resolution can represent the analog signal using 256 discrete digital values ($2^8 = 256$).

Output: The encoded binary values are output from the ADC as a stream of digital data. This digital data can be further processed by digital circuits, microcontrollers, or computers.

ADCs are widely used in various applications where analog signals need to be converted into a digital format for further processing or analysis. Some common applications of ADCs include:

Sensor Data Acquisition: In sensor applications, such as temperature, pressure, and light sensors, ADCs convert analog sensor outputs into digital data that can be analyzed by microcontrollers or computers.

Control Systems: In control systems, ADCs are used to convert real-world physical quantities (like speed, position, and temperature) into digital signals that can be processed and used to control various processes or devices.

Measurement Instruments: In measurement instruments, such as mustimeters and oscilloscopes, ADCs are used to convert analog measurement signals into digital values that can be displayed and analyzed.

The accuracy, resolution, and speed of an ADC are important factors to consider when selecting an appropriate ADC for a specific application. Higher-resolution ADCs provide finer levels of detail in the converted signal, while faster ADCs can handle rapid changes in the input signal. In this setup, Hx711 ADCs are used.

4.3.3 Buck Convertor

A Buck Converter, also known as a step-down converter, is a type of DC-DC converter that efficiently converts a higher input voltage to a lower output voltage.

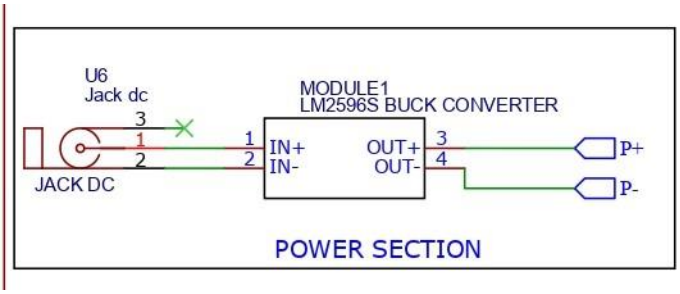

Fig 4.4 Buck Convertor

It's a fundamental component in electronics and power management systems, commonly used to provide regulated voltage levels for various devices. The buck converter takes in a higher input voltage (Vin) and produces a lower output voltage (V_{out}). The output voltage is typically regulated and maintained at a specific level, regardless of variations in the input voltage or load conditions.

4.3.4 SD Card Module

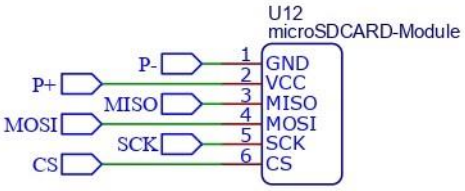

Fig 4.5 SD card Module

An SD card module is an interface module that allows microcontrollers or other devices to interact with Secure Digital (SD) or microSD memory cards. These modules provide a convenient way to read and write data from and to SD cards, making them useful for data logging, storage, and data transfer in various electronic projects.

4.3.5 Real Time Clock Module

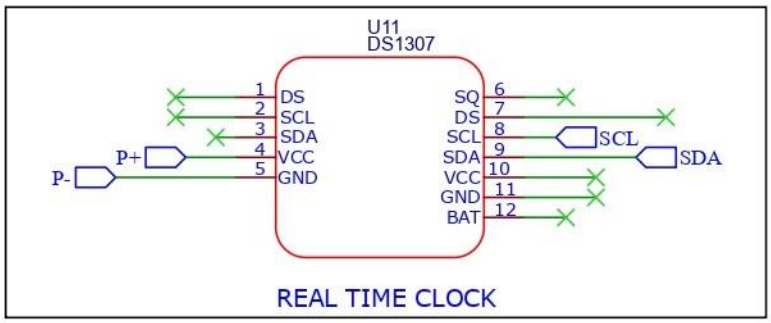

Fig 4.6 RTC Module

RTC module, also known as a Real-Time Clock module, is an electronic component that provides accurate timekeeping functionality to devices, even when the main power source is disconnected. RTC modules are commonly used in various electronic systems where maintaining accurate time and date information is important.

4.3.6 Max 6675 Integrated Module with K-Type Thermocouple

The "MAX6675" is a popular integrated circuit (IC) that is often used in combination with a K-type thermocouple to measure temperature. The K-type thermocouple is a type of temperature sensor commonly used in various industrial and scientific applications. Here's an overview of the MAX6675 and its use with a K-type thermocouple:

Fig 4.7 Max 6675 thermocouple

MAX6675 IC: The MAX6675 is a digital temperature sensor IC that is specifically designed to interface with K-type thermocouples. It incorporates a cold-junction compensation

circuit and an analog-to-digital converter (ADC) to convert the thermocouple's voltage output into a digital temperature reading.

K-Type Thermocouple: A K-type thermocouple consists of two dissimilar metal wires, typically made of chromel and alumel, that generate a voltage proportional to the temperature difference between the two junctions. This voltage is very small and requires amplification and conversion to be useful for temperature measurements.

Cold-Junction Compensation: The MAX6675 compensates for the temperature at the cold end (the junction between the thermocouple and the MAX6675 itself) to ensure accurate temperature measurements.

SPI Interface: The MAX6675 communicates with a microcontroller using the Serial Peripheral Interface (SPI) protocol. It has three main pins for communication: SCK (serial clock), CS (chip select), and SO (serial data out).

Digital Output: The MAX6675 provides a 12-bit digital output that represents the temperature reading. This digital output can be read and processed by the connected microcontroller.

Resolution and Range: The MAX6675 offers a temperature resolution of 0.25°C and has a temperature measurement range typically from -200°C to +700°C, which covers a wide range of industrial and scientific applications.

4.4 Circuit Diagram of PT-DAQ

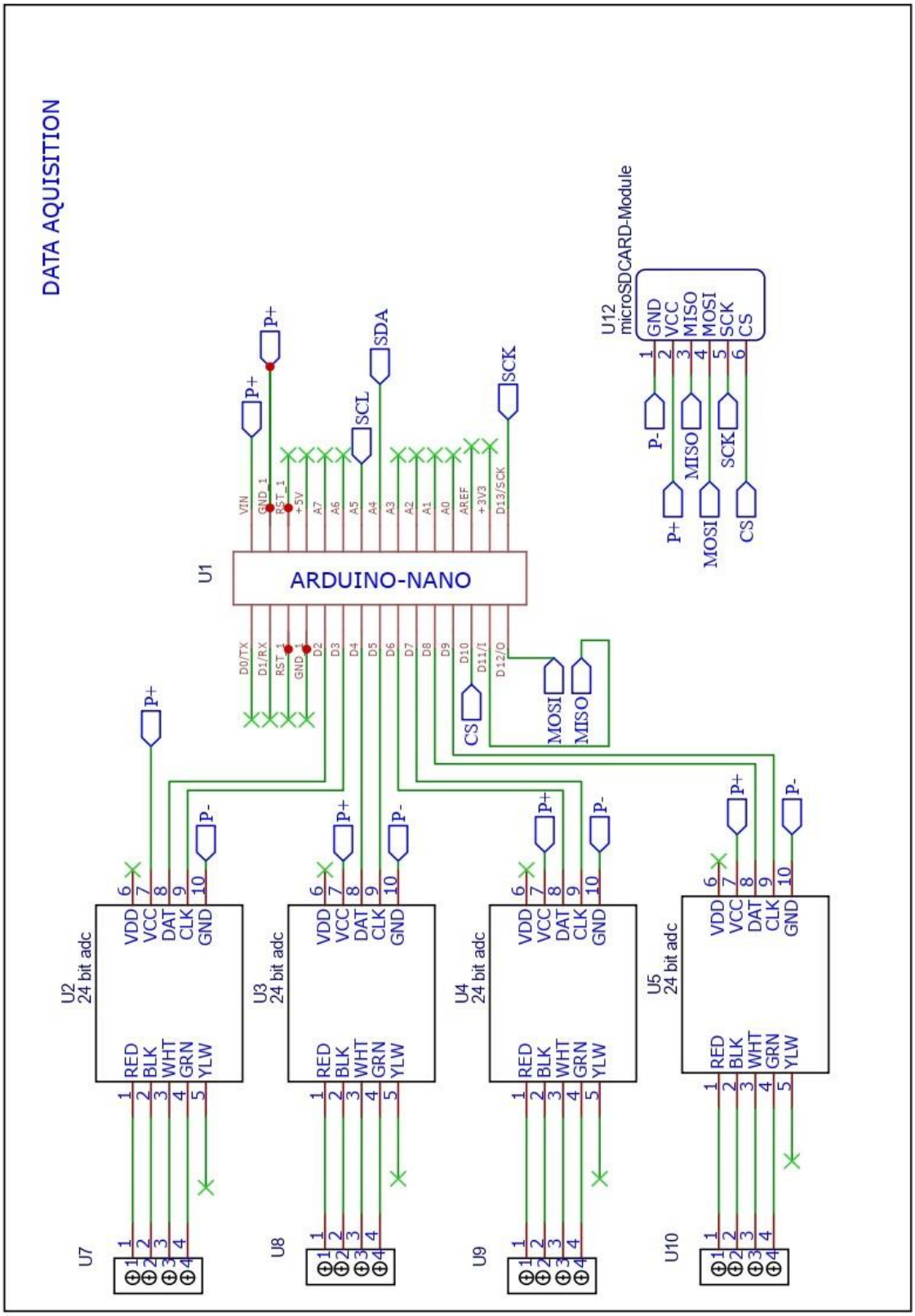

Fig 4.8 Circuit Diagram of PT-DAQ

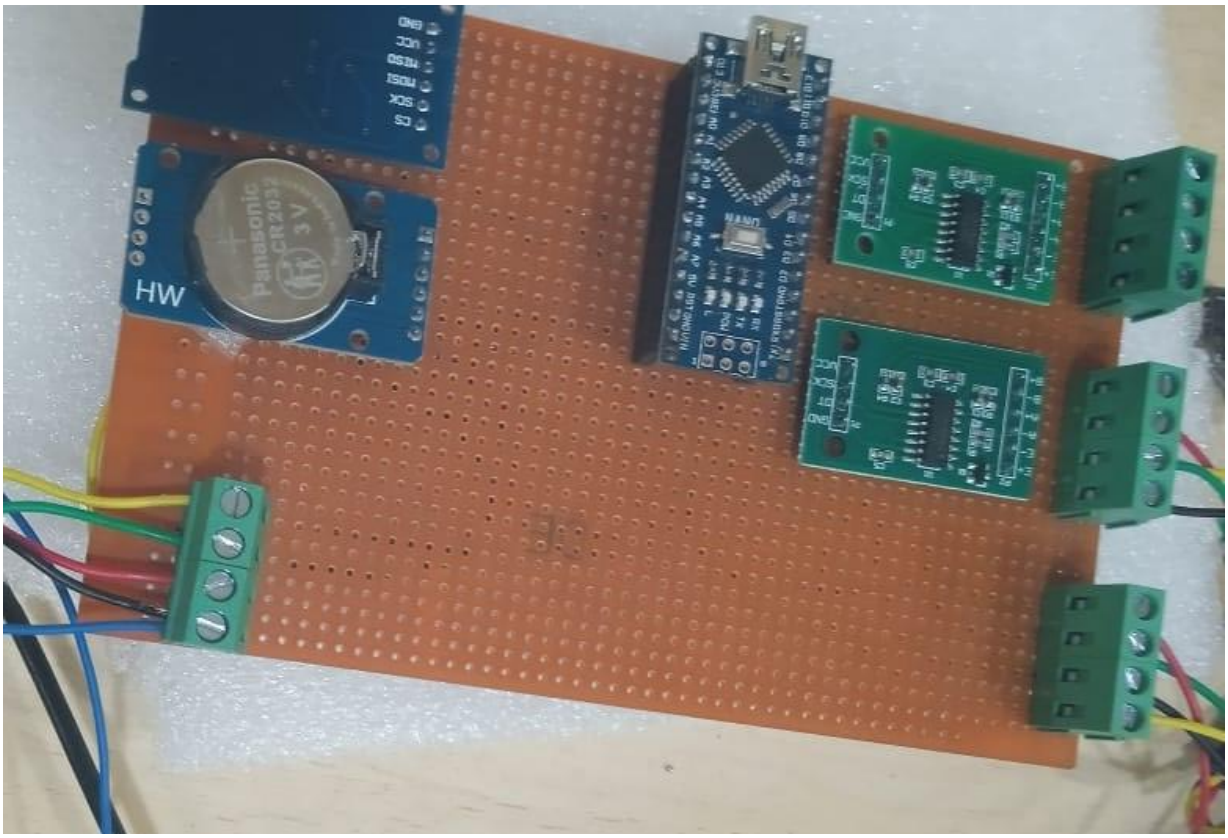

Fig 4.9 Photograph of PT-DAQ

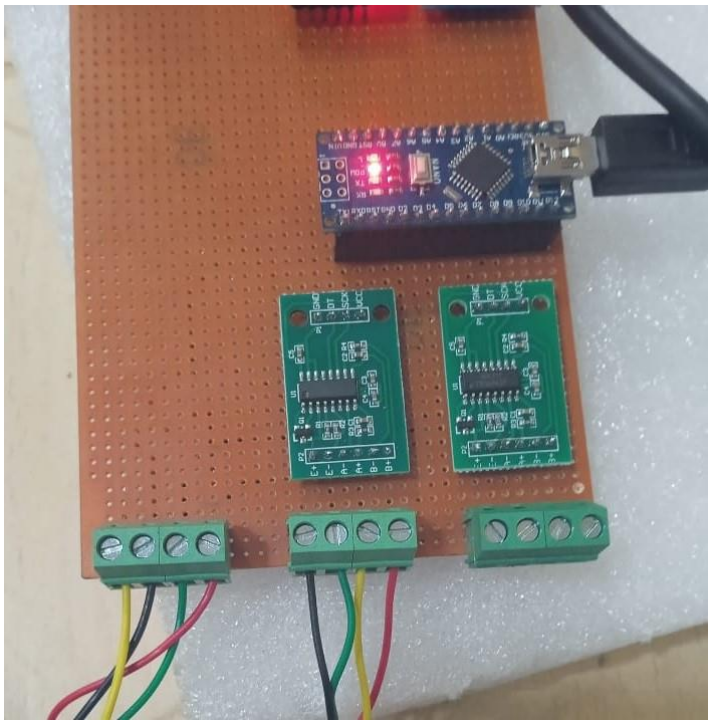

Fig 4.10 PT-DAQ during operation

4.5 Source code of PT-DAQ 1.0

```
#include <max6675.h>
#include <HX711.h>
#include <Wire.h>
#include <SPI.h>
#include <TimeLib.h>
#include <DS1307RTC.h>
#include <LiquidCrystal_I2C.h>

LiquidCrystal_I2C lcd(0x3F,20,4);
int onflag=0;
double current=0,previous=0,cscantime=0,cruntime=0;
char datetime[]="  :  :     /  /  ";
byte i, sec, mint, hou, date, mon, y;

const int dout1=2;
const int sck1=3;

const int dout2=6;
const int sck2=7;

const int clk1=4,cs1=A3,so1=A2,clk2=9,cs2=8,so2=5;
String ch1="",ch2="",ch3="",ch4="",ch5="",ch6="";
int scanrate,runtime;
char scanchar,runtimechar;

long offsetch1=0;
long offsetch2=0;
long reading1,reading2;
float
val1=0,val2=0,val3=0,val4=0,val15=0,val6=0,data1,data2,Strain1,Strain2,resolution
;
HX711 sensor1,sensor2;
MAX6675 thermocouple1(clk1, cs1, so1);
```

```
MAX6675 thermocouple2(clk2, cs2, so2);
void setup()
{
  Serial.begin(9600);
  lcd.init();
  lcd.init();
  lcd.backlight();
  while (!Serial) ; // wait for serial
  sensor1.begin(dout1,sck1);
  sensor2.begin(dout2,sck2);
}

void loop()
{
 settings();
 setscanrate();
 setruntime();
 if(onflag==0)
 {
    Serial.println("CLEARDATA");
    Serial.print("LABEL,Date_Time,");
    Serial.print(ch1);
    Serial.print(",");
    Serial.print(ch2);
    Serial.print(",");
    Serial.print(ch3);
    Serial.print(",");
    Serial.print(ch4);
    Serial.print(",");
    Serial.print(ch5);
    Serial.print(",");
    Serial.println(ch6);

    onflag=1;
 }
```

```
current=millis();
if(current-previous>=1000)
{
 cscantime++;
 cruntime++;
 previous=current;
}
if(cscantime==scanrate&&cruntime<runtime)
{
 //lcd.clear();<for refresh purpose only
 timedateupdate();
 timestampupdate();
 reading1=sensor1.read();
 reading2=sensor2.read();
 cal_Strain(reading1,reading2);
 val3=thermocouple1.readCelsius();
 val4=thermocouple2.readCelsius();
 Serial.print((String)"DATA,");
 Serial.print(datetime);
 lcd.setCursor(0,0);
 lcd.print("v1(mV): ");
 lcd.print(val1);
 Serial.print(",");
 Serial.print(val1);
 Serial.print(",");
 lcd.setCursor(0,1);
 lcd.print("v2(mV): ");
 lcd.print(val2);
 Serial.print(val2);
 Serial.print(",");
 lcd.setCursor(0,2);
 lcd.print("T1(DegC): ");
 lcd.print(val3);
 Serial.print(val3);
 Serial.print(",");
```

```
  lcd.setCursor(0,3);
  lcd.print("T2(DegC): ");
  lcd.print(val4);
  Serial.print(val4);
  Serial.print(",");
  Serial.print(val15);
  Serial.print(",");
  Serial.println(val6);
 cscantime=0;
 //sensor1.power_down();
 //sensor2.power_down();<if needed to turn down sensors
 }
 if(cruntime==runtime)
 {
  while(1);
 }

}
void setscanrate()
{
  switch(scanchar)
  {
    case 's' : scanrate=scanrate;
               break;
    case 'm' :scanrate=scanrate*60;
              break;
    case 'h' :scanrate=scanrate*3600;
              break;
    default : break;
  }
}
void setruntime()
{
  switch(runtimechar)
  {
```

```
    case 's' : runtime=runtime;
               break;
    case 'm' :runtime=runtime*60;
              break;
    case 'h' :runtime=runtime*3600;
              break;
    default : break;
  }
}
void settings()
{
  scanrate=3;
  scanchar='s';
  runtime=2;
  runtimechar='h';
  ch1="Voltage1(mVolt)";
  ch2="Voltage2(mVolt)";
  ch3="Temparature1(deg)";
  ch4="Temparature2(deg)";
  ch5="Temp Diff";
  ch6="Emf Abs";
}
int timedateupdate() //update data&time, Raingauge counter,Email
{
  int h,m;
  Wire.beginTransmission(0x68);
  Wire.write(0);
  Wire.endTransmission(false);
  Wire.requestFrom(0x68, 7);
  sec = Wire.read();
  mint = Wire.read();
  hou   = Wire.read();
  h=(hou >> 4)   * 10 + (hou & 0x0F);
  m=(mint >> 4) * 10 + (mint & 0x0F);
  Wire.read();
```

```
  date   = Wire.read();
  mon  = Wire.read();
  y   = Wire.read();
  //delay(50);
}
void timestampupdate() // Update time Stamp for data logging
{
  sec = (sec >> 4) * 10 + (sec & 0x0F);
  mint = (mint >> 4) * 10 + (mint & 0x0F);
  hou   = (hou >> 4)   * 10 + (hou & 0x0F);
  date   = (date >> 4)   * 10 + (date & 0x0F);
  mon  = (mon >> 4)  * 10 + (mon & 0x0F);
  y   = (y >> 4)   * 10 + (y & 0x0F);
  datetime[7] = sec % 10 + 48;
  datetime[6] = sec / 10 + 48;
  datetime[4] = mint % 10 + 48;
  datetime[3] = mint / 10 + 48;
  datetime[1] = hou % 10 + 48;
  datetime[0] = hou / 10 + 48;
  datetime[10] = date % 10 + 48;
  datetime[9] = date / 10 + 48;
  datetime[13] = mon % 10 + 48;
  datetime[12] = mon / 10 + 48;
  datetime[16] = y % 10 + 48;
  datetime[15] = y / 10 + 48;
}
void cal_Strain(float reading1, float reading2)
{
  resolution =(5.12/ 16777215.0)*4.7;
    val1 = sqrt((resolution * reading1)*(resolution * reading1));
    val2 =  sqrt((resolution * reading2)*(resolution * reading2));
    val15=val3-val4;
    val6=val1-val2;

}
```

4.6 Measurement range and limitations

General temperature range of Max 6675 k-type thermocouple: - -200 to 1260ºC, 12-Bit, 0.25°C Resolution, Accuracy: - 8 LSBs for temperatures ranging from 0°C to +700°C.

Electromotive force measurement using 24-bit resolution ADCs, from 0.5µV to 15mV.

4.7 Future Possibilities of PT-DAQ

The PT-DAQ 1.0 is essentially a prototype designed to record data for calculation of Seebeck effect over a period of time with high precision. The prototype served well. It could be designed into PCBs for better stability and durability. Also, it can be incorporated with more components to measure thermal conductivity which when done, would be a complete thermoelectric setup with ability to take data on any thermoelectric variables, thereby increasing its functionality many folds. Using wireless modules like nodeMCU, ESP32 etc. for wireless access via web or apps designed to measure and record data. Also using better ADCs can achieve even higher precision with wider range of operation and better accuracy than the present version. PT-DAQ can also be programmed to act as basic analog multi-channel data acquisition system instead as well which allows it to be a highly customizable device.

5 Design, Synthesis and Characterization of Samples

5.1 Synthesis Precursors

Precursor used	Molecular weight in grams
$La(NO_3)_3.\ 6H_2O$	433.01
$Co(NO_3)_2.6H_2O$	182.943
$C_6H_8O_7.H_2O$	211.14
$Sr(NO_3)_2$	211.63
$Fe(NO_3)_3.9H_2O$	404.0
$Cu(NO_3)_2.3H_2O$	241.60
$Ni(NO_3)_2.6H_20$	290.79
$Cr(NO_3)_3.9H_20$	400.15
$Mn(NO_3)_2.\ xH_20$	178.95

A facile synthesis route for $LaMO_3$ (M=Cr, Mn, Fe, Co, etc.) nanoparticles employing the sol-gel coupled with calcination method is adopted. In the initial step, the designated precursors are meticulously blended in a beaker with deionized water and subjected to magnetic stirring for a minimum duration of 24 hours. Subsequently, the mixture is subjected to controlled heating at a constant temperature of 110°C while maintaining a strict vigilance over temperature fluctuations, as these can lead to undesirable outcomes like agglomeration, sol-gel separation, and individual oxide formation. The process ensures that water is removed before complete drying, at which point stirring ceases and the residual moisture is meticulously evaluated by whisking the gel-formed material. The resulting gel-like product is then finely ground using a mortar and pestle for approximately 2 hours, with periodic additions of ethanol drops to smoothen the grinding process. The ensuing powder is transferred into an alumina boat and placed within a muffle furnace, where it is exposed to a temperature of 900°C for a duration of 5 hours, preceded by an additional 1.5

hours to attain the desired temperature. After a gradual cooling period overnight, the sample is re-ground for 1 hour using a mortar and pestle, with intermittent ethanol supplementation. The treated powder is then placed back into the alumina boat and returned to the furnace, undergoing a subsequent 4-hour calcination at 900°C, with an extra 1.5-hour period for temperature equilibration. Following another overnight cooling interval, the final product is meticulously transferred into vials, rendering it ready for utilization in various applications.

The prepared samples are:

(a) $LaCrO_3$; (b) $LaMnO_3$; (c) $LaFeO_3$; (d) $LaCoO_3$; (d) $(La)_A(Cr_{1/4}Mn_{1/4}Fe_{1/4}Co_{1/4})_B O_3$, abbreviated as HEP-1; and (e) $(La_{2/3}Sr_{1/3})_A(Cr_{1/6}Mn_{1/6}Fe_{1/6}Co_{1/6}Ni_{1/6}Cu_{1/6})_B O_3$, abbreviated as HEP-2.

For the fabrication of thin films, the powdered samples are dispersed within a 1:2 mixture of acetone and DMF, achieving a concentration of 1 mg/mL. This dispersion is accomplished through ultrasonication at room temperature for a duration of 5 minutes. Subsequently, the resulting mixture is applied onto a glass substrate using spin-coating methodology. Specifically, a 20 µL aliquot of the solution is delicately deposited onto a 1 cm × 1.5 cm substrate, followed by rapid rotation at 1500 rpm for 30 seconds. The rotational process involves a 10-second interval for both acceleration and deceleration. Upon completion of the spin-coating step, the coated substrate is subjected to drying at 70 ℃ for a span of five minutes. This entire procedure is iterated thrice to ensure uniformity and quality. Finally, the resultant film is subjected to vacuum drying for a couple of hours at a temperature of 70 ℃, thus concluding the film preparation process.

5.2 Design of Perovskite Oxides

Perovskites can typically crystallize as cubic, tetragonal, orthorhombic, or rhombohedral lattice. We get some idea of the possible structure from its tolerance factor. The more it shifts from unity, the structure deviates from cubic lattice. The ionic radii of elements are picked from, http://crystalmaker.com/support/tutorials/atomic-radii/index.html to calculate the tolerance factor.

Table 5.1: Tolerance factors of different perovskite compounds

HEP compound $[ABO_3]$	Tolerance factor $\left[t = \frac{(r_A + r_O)}{\sqrt{2}(r_B + r_O)}\right]$	Value
$\mathbf{LaCrO_3}$ **(Ortho Pnma)**	$\frac{(1.95 + 0.60)}{\sqrt{2}(1.40 + 0.60)}$	0.902
$\mathbf{(La_{2/3}Sr_{1/3})CrO_3}$	$\frac{\left(\frac{2}{3} \times 1.95 + \frac{1}{3} \times 2.00 + 0.60\right)}{\sqrt{2}(1.40 + 0.60)}$	0.907
$\mathbf{LaMnO_3}$ **(Rhombo)**	$\frac{(1.95 + 0.60)}{\sqrt{2}(1.40 + 0.60)}$	0.902
$\mathbf{(La_{2/3}Sr_{1/3})MnO_3}$	$\frac{\left(\frac{2}{3} \times 1.95 + \frac{1}{3} \times 2.00 + 0.60\right)}{\sqrt{2}(1.40 + 0.60)}$	0.907
$\mathbf{LaFeO_3}$ **(Ortho)**	$\frac{(1.95 + 0.60)}{\sqrt{2}(1.40 + 0.60)}$	0.902
$\mathbf{(La_{2/3}Sr_{1/3})FeO_3}$	$\frac{\left(\frac{2}{3} \times 1.95 + \frac{1}{3} \times 2.00 + 0.60\right)}{\sqrt{2}(1.40 + 0.60)}$	0.907
$\mathbf{LaCoO_3}$ **(Rhombo)**	$\frac{(1.95 + 0.60)}{\sqrt{2}(1.35 + 0.60)}$	0.925
$\mathbf{LaNiO_3}$ **(Rhombo)**	$\frac{(1.95 + 0.60)}{\sqrt{2}(1.35 + 0.60)}$	0.925
$\mathbf{(La_{2/3}Sr_{1/3})CoO_3}$	$\frac{\left(\frac{2}{3} \times 1.95 + \frac{1}{3} \times 2.00 + 0.60\right)}{\sqrt{2}(1.35 + 0.60)}$	0.931
$\mathbf{(La_{2/3}Sr_{1/3})(Mn_{1/3}Fe_{1/3}Co_{1/3})O_3}$	$\frac{\left(\frac{2}{3} \times 1.95 + \frac{1}{3} \times 2.00 + 0.60\right)}{\sqrt{2}\left(\frac{1.40 + 1.40 + 1.35}{3} + 0.60\right)}$	0.915
$\mathbf{(La_{1/2}Sr_{1/2})(Cr_{1/4}Mn_{1/4}Fe_{1/4}Co_{1/4})O_3}$	$\frac{\left(\frac{1.95 + 2.00}{2} + 0.60\right)}{\sqrt{2}\left(\frac{1.40 \times 3 + 1.35}{4} + 0.60\right)}$	0.916

5.3 Characterization of Samples

5.3.1 XRD Data Analysis

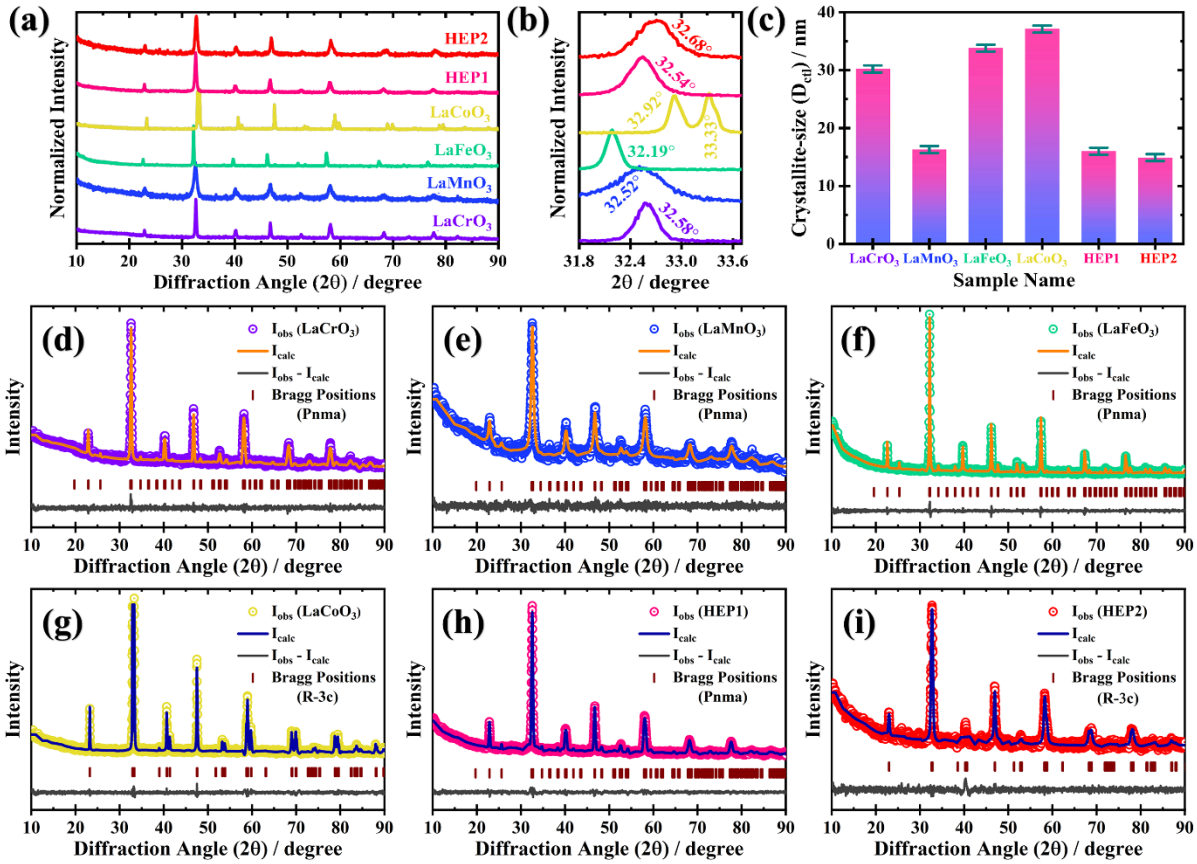

Fig. 5.2: (a) XRD patterns for all six samples; (b) magnified view of the (112) Bragg peak to recognize peak-shifting for different samples; (c) comparison of crystallite-sizes calculated using the Scherrer's formula. Rietveld refinement of the XRD patterns obtained for (d) $LaCrO_3$; (e) $LaMnO_3$; (f) $LaFeO_3$; (g) $LaCoO_3$; (h) HEP-1; and (i) HEP-2.

Rietveld refinement stands as a powerful and intricate analytical method in the realm of materials science, specifically in the field of X-ray diffraction (XRD). This approach, named after its creator Hugo Rietveld, enables the extraction of accurate structural information from powder X-ray diffraction patterns, facilitating the determination of crystal structures and the refinement of their associated parameters. Unlike conventional peak fitting methods that focus on extracting peak positions and intensities, Rietveld refinement involves a comprehensive analysis that considers multiple parameters simultaneously to optimize the fit between the experimental data and the calculated diffraction pattern from a known or hypothesized crystal structure.

At its core, the Rietveld refinement process involves iteratively adjusting parameters such as lattice parameters, atomic positions, thermal vibrations, and background contributions to minimize the difference between the observed and calculated diffraction patterns. The least-squares optimization technique is central to this process, and modern computational tools have greatly facilitated its execution. As the refinement iterates, the fit between the observed and calculated patterns improves, resulting in an increasingly accurate representation of the crystalline structure under investigation.

Rietveld refinement is especially potent when dealing with complex crystal structures, multi-phase samples, and materials with local disorder. It provides insights into atomic positions, unit cell dimensions, thermal vibrations, and site occupancy, even extending to anisotropic thermal displacement factors. Additionally, it allows the estimation of microstructural parameters like crystallite size and microstrain.

Despite its power, Rietveld refinement demands careful consideration of factors such as data quality, instrument resolution, and the choice of appropriate structural models. Moreover, its successful execution requires a deep understanding of crystallography, diffraction physics, and computational techniques. In the broader context of material characterization, Rietveld refinement serves as an essential tool for unravelling the intricate arrangements of atoms within crystalline materials, offering profound insights into their properties and behavior.

From Rietveld refinement and the literature, it is found that, LaMO3 crystallizes in an orthorhombic lattice (typically $Pnma$) if M = Cr, Mn, Fe; whereas it crystallizes in a rhombohedral lattice (typically $R\bar{3}c$), if M = Co, Ni, Cu. For the latter structure, generally each Bragg peak splits into a couple of closely spaced peaks. Considering the high-entropy samples, HEP-1 takes the orthorhombic structure, whereas HEP-2 takes the rhombohedral structure.

The determination of crystallite size using Scherrer's formula is a widely employed technique in materials science. This formula establishes a correlation between the breadth of diffraction peaks in X-ray or other diffraction patterns and the size of crystalline domains within a material. The formula is given by,

$$D_{ctl} = \frac{K\lambda}{\beta \cos\theta} \tag{27}$$

Where, D_{ctl} represents the crystallite size, K is the Scherrer constant accounting for the shape of the crystallites (typically around 0.9), λ is the wavelength of the X-ray radiation source, β is the full width at half maximum (FWHM) of the diffraction peak, and θ corresponds to the Bragg angle. By analyzing the diffraction pattern of a material, particularly a crystalline solid, and applying Scherrer's formula, researchers can estimate the average dimensions of the crystalline domains present. This information is valuable for understanding material properties and behaviors, influencing a broad spectrum of fields ranging from nanotechnology to solid-state physics.

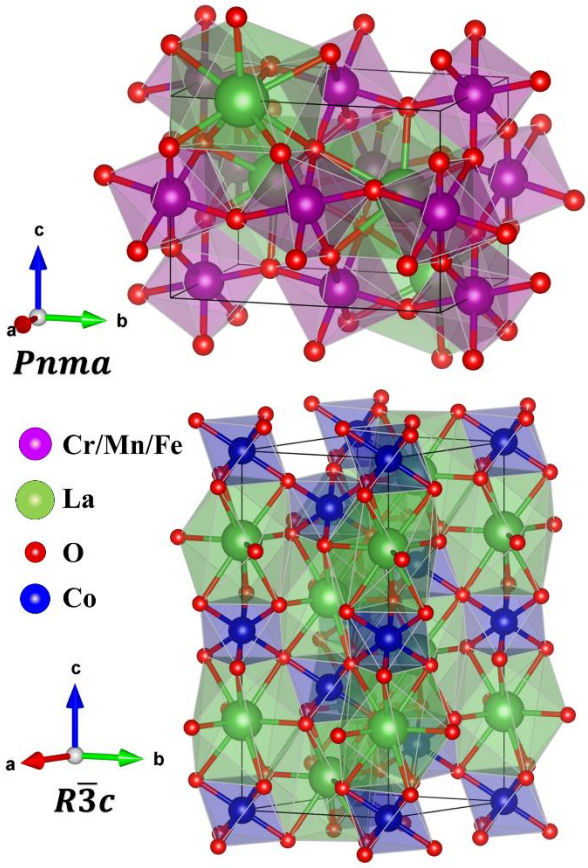

Fig 5.3: Orthorhombic (upper) and rhombohedral (lower) unit cells for $LaMO_3$ perovskites.

5.3.2 FESEM Data Analysis

Field-Emission Scanning Electron Microscopy (FESEM) is a powerful imaging technique widely used in materials science to obtain high-resolution images of the surface morphology of various materials, ranging from nanoparticles to bulk samples. FESEM utilizes an electron beam emitted from a sharp tungsten filament or other electron sources, and the interaction between this beam and the sample surface provides detailed information about the sample's topography, surface features, and composition.

When applied to $LaMO_3$ nanoparticles, FESEM can provide valuable insights into their size, shape, distribution, and overall morphology. The high spatial resolution of FESEM allows researchers to visualize the nanoparticles at nanoscale dimensions, providing information about their uniformity and whether they exhibit agglomeration or clustering. By observing the particle size distribution, one can assess the degree of monodispersity or polydispersity, crucial for applications where particle size consistency is important.

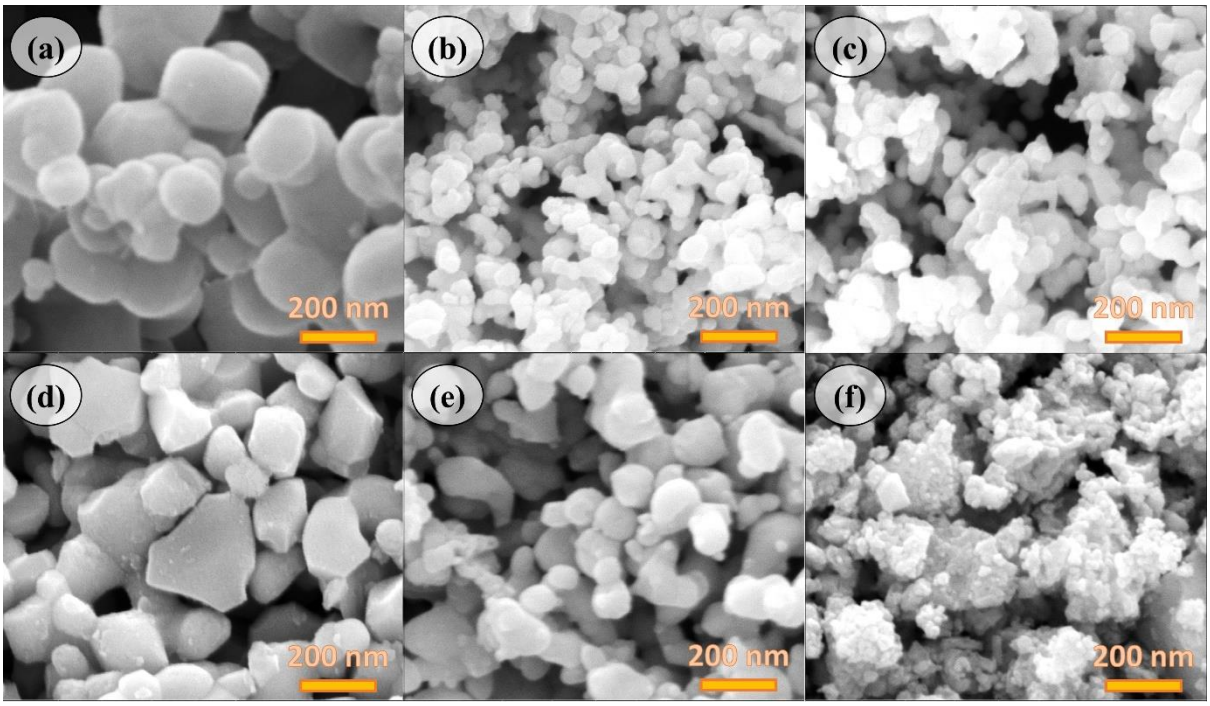

Figure 5.4: FESEM micrographs for (a) $LaCrO_3$; (b) $LaMnO_3$; (c) $LaFeO_3$; (d) $LaCoO_3$; (e) HEP-1; and (f) HEP-2.

FESEM images also reveal surface features and structural characteristics of the nanoparticles. Researchers can identify facets, edges, and surface defects, gaining insights into the crystal growth mechanism and potential crystallographic orientations. Moreover, FESEM coupled with energy-dispersive X-ray spectroscopy (EDS) allows for elemental mapping and compositional analysis. In the case of LaMO3 nanoparticles, this can offer information about the distribution of lanthanum, transition metal (M), and oxygen within the particles, verifying the stoichiometry and potential dopant incorporation.

Additionally, FESEM can provide information about the agglomeration state and the presence of any coatings or surface modifications on the nanoparticles. This is particularly important when considering the nanoparticles' dispersibility and interactions with other materials, as these factors can influence their performance in various applications, such as catalysis, electronics, and energy storage.

In summary, FESEM applied to LaMO3 nanoparticles offers a wealth of information about their size, shape, distribution, surface features, and composition. These insights are pivotal for tailoring the synthesis process, optimizing properties, and understanding how these nanoparticles interact with their environment, thereby enabling informed decisions in designing and utilizing these materials for diverse applications.

5.3.3 EDX Analysis

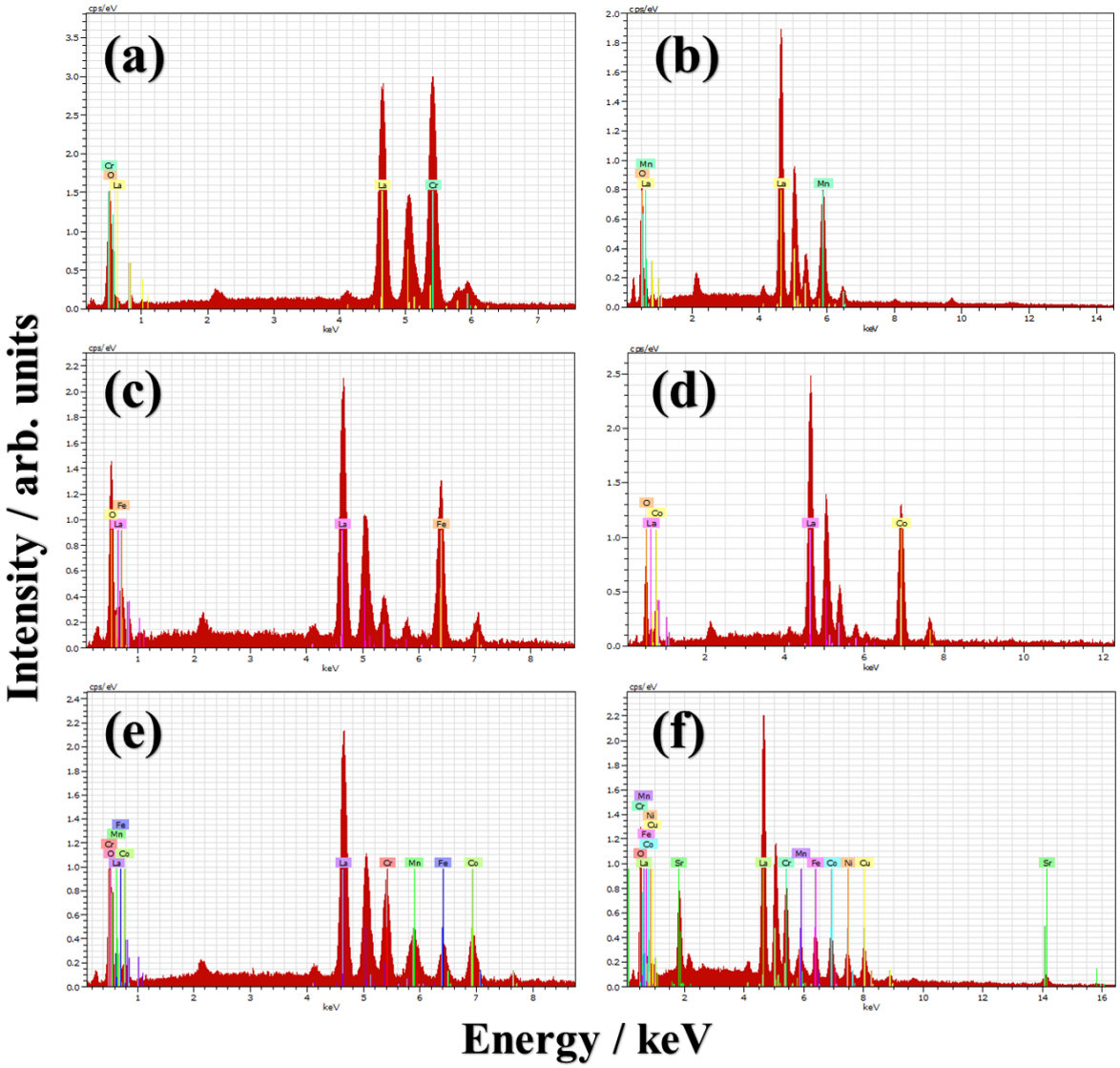

Figure 5.5: EDX spectra for (a) $LaCrO_3$; (b) $LaMnO_3$; (c) $LaFeO_3$; (d) $LaCoO_3$; (e) HEP-1; and (f) HEP-2.

Energy-Dispersive X-ray Spectroscopy (EDX), also known as Energy-Dispersive X-ray Analysis (EDXA) or Energy-Dispersive X-ray Microanalysis (EDXMA), is a technique used to analyze the elemental composition of a sample. It is often coupled with electron microscopes, such as Scanning Electron Microscopy (SEM) or Transmission Electron Microscopy (TEM), to provide insights into the distribution and abundance of elements within a sample.

When applied to LaMO3 (M=Cr, Mn, Fe, Co, etc.) nanoparticles, EDX spectroscopy can provide crucial information about the chemical composition of the nanoparticles. Here are some key points about EDX spectra and what we can learn from them:

Elemental Composition: EDX spectra show peaks corresponding to the characteristic X-rays emitted when electrons from the sample are displaced and subsequently return to lower energy states. By analyzing the energies of these X-rays, researchers can determine which elements are present in the sample. For $LaMO_3$ nanoparticles, the spectrum can reveal the presence of lanthanum (La), the transition metal (M), and oxygen (O), helping to verify the stoichiometry of the compound.

Quantitative Analysis: EDX spectra provide semi-quantitative information about the relative abundance of different elements. While EDX can't provide absolute atomic percentages, it can offer insights into the general composition of the nanoparticles. This is especially important for materials like $LaMO_3$, where the ratio of lanthanum to the transition metal is critical to the material's properties.

Elemental Mapping: Coupling EDX with electron microscopy allows researchers to perform elemental mapping, which visually represents the spatial distribution of different elements within the sample. This can help identify compositional variations, elemental segregation, or even the presence of impurities. For $LaMO_3$ nanoparticles, elemental mapping can reveal how uniformly the lanthanum and transition metal are distributed within individual particles and across the entire sample.

Dopant or Substitution Analysis: If doping or element substitution is part of the synthesis process, EDX can be used to verify the incorporation of specific elements into the crystal lattice of the nanoparticles. This is particularly relevant for applications where introducing specific elements can enhance or modify the material's properties.

Surface and Interface Analysis: EDX can provide insights into the composition of the nanoparticle surface or interfaces. This is particularly important for understanding how the nanoparticles might interact with their surroundings, such as in catalysis or in nanocomposite materials.

5.3.4 DRS Data Analysis

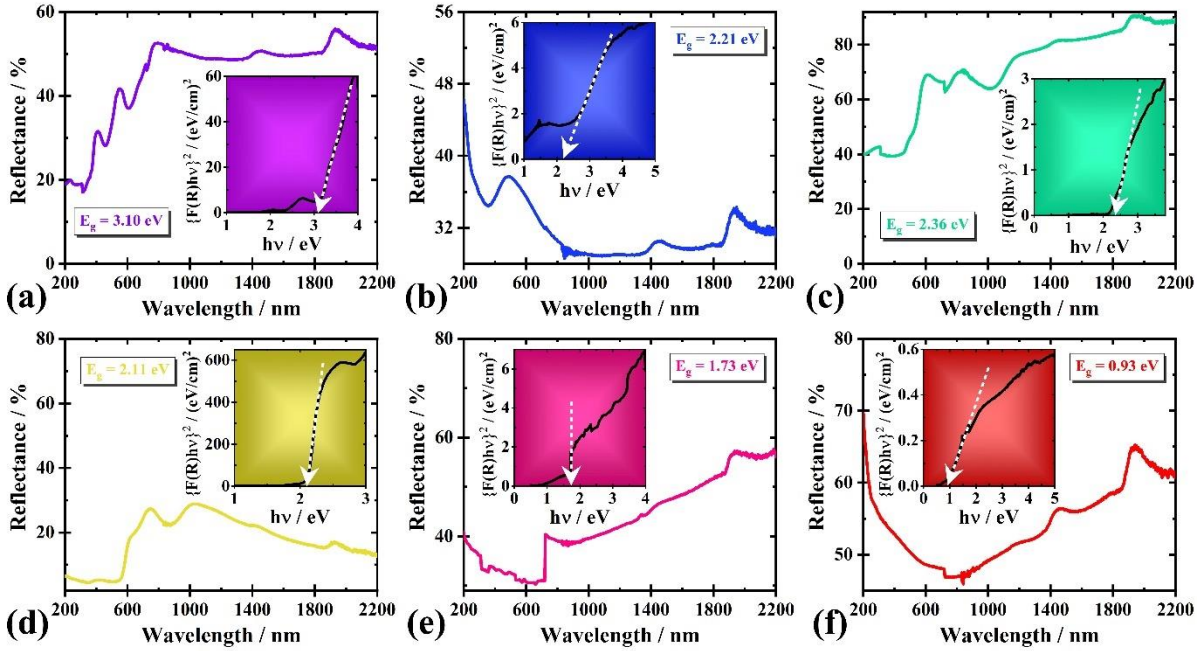

Fig 5.6: Diffuse reflectance spectra and optical band-gap determination using Tauc's plots (shown in the insets) for (a) $LaCrO_3$; (b) $LaMnO_3$; (c) $LaFeO_3$; (d) $LaCoO_3$; (e) HEP-1; and (f) HEP-2.

Diffuse Reflectance Spectroscopy (DRS) is a technique used to study the absorption and scattering of light by solid materials, providing information about their electronic structure, band gaps, and optical properties. When applied to LaMO3 (M=Cr, Mn, Fe, Co, etc.) nanoparticles, DRS can offer insights into the material's energy levels, band gap, and potential applications in optoelectronic devices.

DRS spectra reveal how a material interacts with light over a range of wavelengths. In the case of LaMO3 nanoparticles, the DRS spectrum can help determine the band gap energy, which is the energy difference between the valence band (highest occupied energy level) and the conduction band (lowest unoccupied energy level). The band gap provides information about the material's ability to absorb and emit light and is crucial for understanding its behavior as a semiconductor.

5.3.4.1 Optical Band-Gap Determination using Tauc's Plots:

Tauc's plots are used to determine the optical band gap energy of a material from its absorption spectrum. The Tauc plot involves plotting the absorption coefficient (α) as a function of photon energy (h*ν*), where α is proportional to the absorption intensity and hν represents the energy of the incident photons. In this plot, the band gap energy can be identified as the point where the absorption coefficient starts to increase steeply with increasing photon energy.

5.3.4.2 Kubelka-Munk Theory:

The Kubelka-Munk theory is a mathematical model used to relate the diffuse reflectance (R∞) of a sample to its absorption (α) and scattering (S) properties. This theory is particularly useful for analyzing opaque or highly scattering materials, such as powders or nanoparticles. The Kubelka-Munk equation is given by,

$$F(R_\infty) = \frac{(1-R_\infty)^2}{2R_\infty} = \frac{K}{S} = \frac{1+R_\infty}{1-R_\infty} \quad (28)$$

Here, $F(R_\infty)$ is the Kubelka-Munk function, R_∞ is the diffuse reflectance, K is the absorption coefficient, and S is the scattering coefficient.

This equation allows for the determination of absorption and scattering properties from measured reflectance data. In the context of DRS spectra for LaMO3 nanoparticles, the Kubelka-Munk theory can help extract information about the nanoparticles' absorption properties, scattering behavior, and ultimately, their band gap energy.

In summary, Diffuse Reflectance Spectroscopy (DRS) is a valuable technique for investigating the optical properties of LaMO3 nanoparticles. Through analysis of DRS spectra and the application of Tauc's plots, researchers can determine the material's band gap energy, providing insights into its semiconductor behavior and potential applications in optoelectronic devices. The Kubelka-Munk theory further enhances our understanding of the interaction of light with these nanoparticles, allowing for the extraction of absorption and scattering coefficients for comprehensive optical characterization.

5.3.5 FTIR Data Analysis

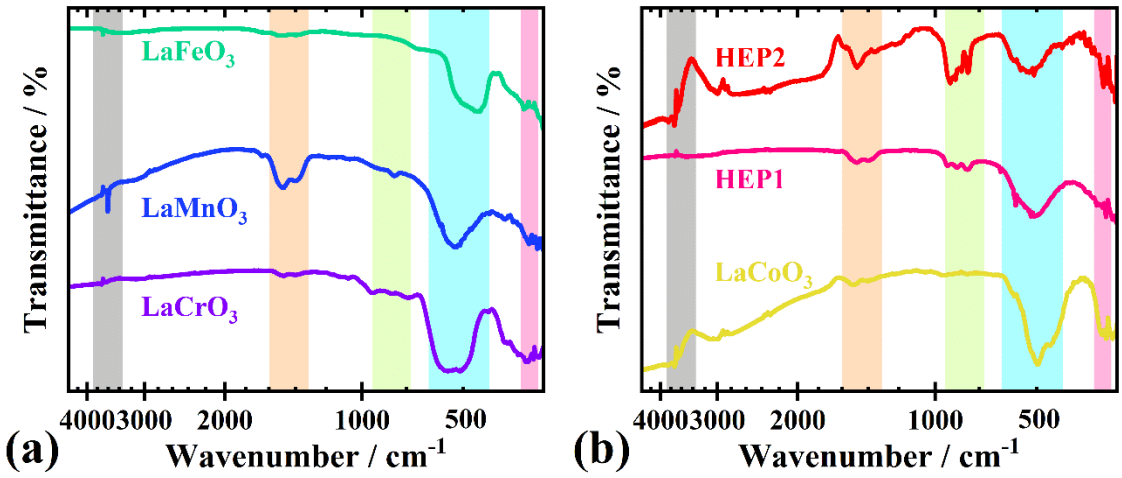

Fig 5.7: FTIR spectra for (a) $LaCrO_3$; (b) $LaMnO_3$; (c) $LaFeO_3$; (d) $LaCoO_3$; (e) HEP-1; and (f) HEP-2.

Fourier-Transform Infrared Spectroscopy (FTIR) is a powerful analytical technique used to study the vibrational modes of molecules and materials. When applied to LaMO3 (M=Cr, Mn, Fe, Co, etc.) nanoparticles, FTIR can provide valuable information about the chemical composition, bonding, and functional groups present in the material.

FTIR spectra are obtained by measuring the absorption of infrared light by a sample as a function of frequency or wavelength. Here's what we can learn from FTIR spectra when applied to LaMO3 nanoparticles:

Chemical Composition: FTIR spectra provide information about the chemical bonds present in a material. Peaks in the FTIR spectrum correspond to specific vibrational modes of the atoms within the material. By analyzing these peaks, researchers can identify the types of chemical bonds and functional groups in the nanoparticles. For LaMO3, the FTIR spectrum can reveal information about the metal-oxygen bonds, as well as any surface functional groups that might be present.

Crystal Structure: The FTIR spectrum can provide insights into the crystal structure of the nanoparticles. Different crystal structures can exhibit distinct vibrational modes, allowing researchers to confirm the crystal phase of LaMO3.

Surface Chemistry: FTIR can reveal surface adsorption or functionalization of nanoparticles. Peaks corresponding to surface groups, adsorbed species, or modifications can be observed, providing information about the surface chemistry and potential interactions with other molecules or substrates.

Phase Transitions and Thermal Behavior: Changes in the FTIR spectrum as a function of temperature can indicate phase transitions or thermal decomposition of the material. This is particularly useful for understanding the stability and behavior of LaMO3 nanoparticles under varying conditions.

Doping or Substitution: FTIR can detect shifts or changes in vibrational modes due to doping or element substitution. This can be important for verifying the incorporation of specific elements into the material's structure.

Hydroxyl or Water Absorption: FTIR can identify absorption bands associated with hydroxyl groups (OH) or water molecules adsorbed onto the nanoparticle surface. This can provide insights into the material's surface reactivity and potential moisture sensitivity.

In summary, FTIR spectroscopy is a versatile technique for characterizing LaMO3 nanoparticles. It offers information about the chemical composition, crystal structure, surface chemistry, and potential functional groups. By interpreting FTIR spectra, researchers can gain a deeper understanding of the nanoparticles' properties, behavior, and potential applications in various fields including catalysis, electronics, and energy storage.

The expected positions of bands in an FTIR spectrum for LaMO3 (M=Cr, Mn, Fe, Co, etc.) nanoparticles can vary based on the specific crystal structure and chemical composition of the material. However, some general information can be provided about the typical positions of bands that might be observed in the FTIR spectrum of LaMO3 nanoparticles:

Metal-Oxygen Stretching Modes: In the region of 400-700 cm^{-1}, you might expect to see bands associated with metal-oxygen stretching vibrations. The precise positions of these bands can vary depending on the specific transition metal (M) and its coordination environment in the crystal structure.

Lanthanum-Oxygen Stretching Modes: Bands corresponding to lanthanum-oxygen stretching vibrations might be observed in the 400-700 cm^{-1} range, similar to the metal-oxygen stretching modes. Again, the exact positions can depend on the crystal structure.

M-O-M Bending Modes: In the region of 600-1000 cm^{-1}, you might find bands associated with metal-oxygen-metal bending vibrations. The positions of these bands can give insights into the coordination geometry around the transition metal ions.

Oxygen-Hydroxyl or Surface Adsorption: If there are hydroxyl groups or surface adsorbed species present on the nanoparticle surface, you might observe bands in the range of 3000-3800 cm^{-1}. These bands can be indicative of hydrogen bonding or interactions with surface molecules.

Metal-Oxygen Vibrations in Higher Frequency Range: In the higher frequency range of 1000-1700 cm^{-1}, you might find bands related to metal-oxygen vibrations in more complex modes or due to different coordination environments.

Wavenumber range (cm^{-1})	**Highlighting color**	**Ascribed modes of vibration**
415 – 445	Pink	La-O and M-O stretching vibrations (M indicates a transition metal *viz*., Cr, Mn, Fe, Co, Ni, or Cu).
530 – 700	Indigo	Symmetric and asymmetric bending of M-O-M bonds.
790 – 940	Lemon green	Symmetric and asymmetric bending of La-O-M bonds. For HEP1 and HEP2, M-O-M' bending also contributes, where M and M' are two different transition metal. For HEP2, Sr-O-M bending contributes too.
1320 – 1580	Pale orange	H-O-H deformation peak of adsorbed moisture.
3400 – 3800	Grey	Asymmetric stretching of hydroxyl group.

Fig 5.8: Assignment of vibrational modes in FTIR spectra

6 Results and Discussion

6.1 Thermoelectric effect

The thermoelectric effect refers to the phenomenon where a temperature difference across a material leads to the generation of an electric voltage or an electric current, or conversely, where the application of an electric current causes a temperature difference. This effect is the basis for thermoelectric devices, which can convert heat energy directly into electrical energy (Seebeck effect) or vice versa (Peltier effect), and can also explain the relationship between temperature and electric potential in conductors (Thomson effect).

6.1.1. Seebeck Effect:

The Seebeck effect, also known as the thermoelectric effect, is the generation of an electromotive force (EMF) in a circuit consisting of two different conductors when there's a temperature gradient between the two junctions. In simpler terms, it's the generation of voltage due to a temperature difference. When two different metals or semiconductors are connected at two junctions to form a closed loop (a thermocouple), and there's a temperature difference between the junctions, an electric current is induced in the circuit. The induced voltage is proportional to the temperature difference and the Seebeck coefficient of the materials.

6.1.2. Peltier Effect:

The Peltier effect is the reverse of the Seebeck effect. When a current flows through a circuit made of two different conductors (or semiconductors) connected at two junctions, heat is either absorbed or released at each junction, depending on the direction of the current. In simpler terms, when an electric current flows through the junctions, a temperature difference is created. This phenomenon is used in Peltier coolers or thermoelectric coolers, where applying a current leads to heat absorption at one junction and heat release at the other, resulting in cooling or heating of the device.

6.1.3. Thomson Effect:

The Thomson effect describes the phenomenon where heat is either absorbed or released when an electric current flows through a conductor that has a temperature gradient along its length. Essentially, as current flows through the conductor, the temperature gradient causes the electrons to move from hotter to cooler regions, leading to heat being absorbed or released. This effect is more prominent in conductors with high electrical conductivity and low thermal conductivity.

6.2 Scientific Explanation:

All three effects are rooted in the behavior of charge carriers (electrons) in conductive materials. When there's a temperature gradient, the electrons move from higher to lower temperatures, creating a flow of charge and thus generating an electric field. This electric field leads to the Seebeck voltage in the Seebeck effect and the heat absorption/release in the Peltier effect. The Thomson effect is a consequence of the combination of electron movement due to temperature gradient and the fact that electrons themselves carry thermal energy, leading to heat generation or absorption.

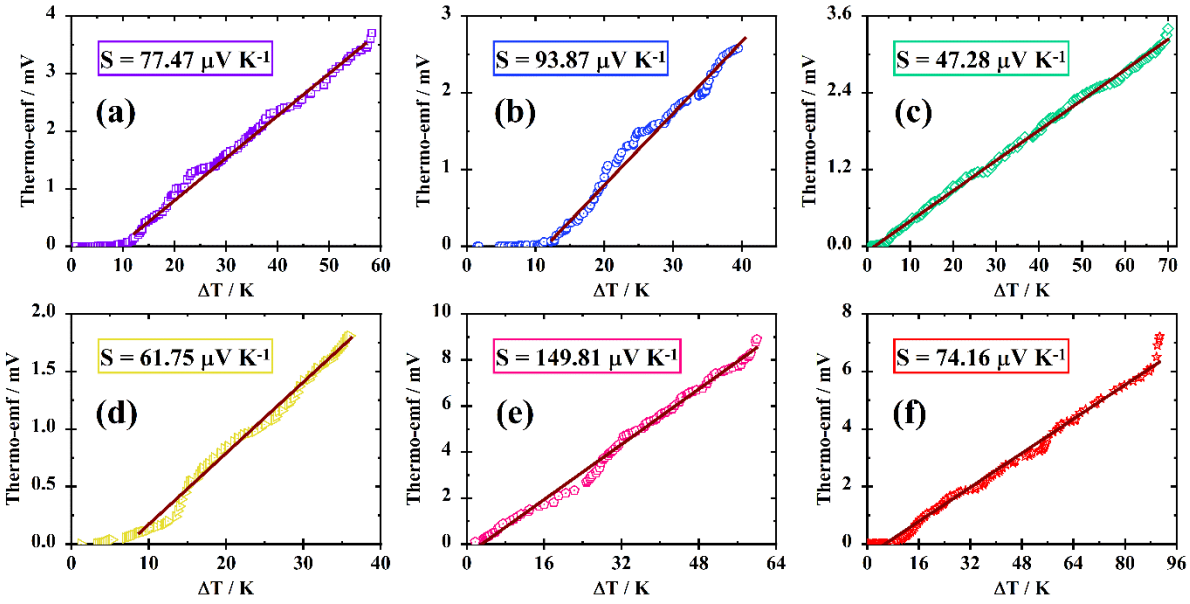

Fig 6.1: Thermo-emf versus temperature difference (ΔT) between the hot and cold sides of the thin films and calculation of Seebeck coefficient (S) for (a) $LaCrO_3$; (b) $LaMnO_3$; (c) $LaFeO_3$; (d) $LaCoO_3$; (e) HEP-1; and (f) HEP-2.

In thermoelectric materials, the goal is to enhance the efficiency of the Seebeck effect and minimize the Peltier effect (which causes heating at the junctions of a thermoelectric device) to create efficient thermoelectric generators or coolers. These materials often have a combination of high electrical conductivity and low thermal conductivity, enabling the efficient conversion of heat energy into electrical energy or vice versa.

The Seebeck effect, named after physicist Thomas Johann Seebeck who discovered it in 1821, is a fundamental phenomenon in thermoelectricity where a temperature difference across a conductor or a semiconductor material results in the generation of an electromotive force (EMF) or voltage. This effect is at the heart of thermoelectric devices that can convert waste heat into usable electrical power and has applications in power generation, waste heat recovery, and temperature sensing.

The Seebeck effect arises due to the behavior of charge carriers (usually electrons) in a temperature gradient. When one end of a conductor or a thermoelectric material is hotter than the other, electrons near the hotter end gain energy and move towards the colder end, creating a charge imbalance and thus generating a voltage difference between the two ends. This voltage difference is called the Seebeck voltage or thermoelectric voltage.

The **Seebeck coefficient (α)**, also known as the thermoelectric power or thermopower, is a material-specific property that quantifies the amount of voltage generated per unit temperature difference between the two ends of the material. Mathematically, the Seebeck coefficient is defined as:

$$\alpha = -\Delta V / \Delta T$$

Where, α is the Seebeck coefficient (V/K), ΔV is the induced voltage difference across the material (V) and ΔT is the temperature difference across the material (K)

In essence, the Seebeck coefficient represents how efficiently a material converts a temperature gradient into an electric potential difference. Positive values of the Seebeck coefficient indicate that the material generates a positive voltage when the hot end is on the right side, and negative values indicate the opposite.

The Seebeck coefficient of different materials varies widely due to differences in charge carrier density, mobility, and other material-specific factors. Some examples of Seebeck coefficients (at room temperature) for various materials include:

Bismuth telluride (Bi_2Te_3): Around +200 μV/K
Lead telluride (PbTe): Around -300 μV/K
Silicon (Si): Around +700 μV/K
Copper (Cu): Around +4 μV/K

Thermoelectric materials are often characterized by their high absolute value of the Seebeck coefficient combined with high electrical conductivity and low thermal conductivity, as these factors determine the material's overall thermoelectric performance. Efficient thermoelectric materials have a high Seebeck coefficient to generate a significant voltage for a given temperature difference, enabling the conversion of heat into electricity with good efficiency.

6.3 Power Factor:

The power factor of a material in the context of the Seebeck effect refers to its ability to efficiently convert a temperature gradient into electrical power. It is a measure of how effectively a material can generate an electric current in response to a temperature difference. The power factor (PF) is calculated as the product of the square of the Seebeck coefficient (α) and the electrical conductivity (σ):

$$PF = \alpha^2\sigma$$

A high-power factor indicates that the material has a combination of a large Seebeck coefficient (which generates a higher voltage for a given temperature difference) and a high electrical conductivity (which allows for efficient current flow). Power factor is a critical factor in determining the efficiency of thermoelectric materials for power generation applications.

6.3.1 Figure of Merit (ZT) in the Seebeck Effect:

The figure of merit (ZT) is a key parameter used to assess the performance of a material in thermoelectric applications. It takes into account not only the power factor but also the thermal conductivity (κ) of the material. The figure of merit is given by:

$ZT = \alpha^2 \sigma T / \kappa$

Where, α is the Seebeck coefficient, σ is the electrical conductivity, T is the absolute temperature (in Kelvin), κ is the thermal conductivity.

A higher ZT value indicates a more efficient thermoelectric material. Achieving a high ZT requires a delicate balance between high power factor (larger $\alpha^2\sigma$) and low thermal conductivity. High thermal conductivity can quickly dissipate the temperature gradient that drives the Seebeck effect, reducing the efficiency of the thermoelectric conversion.

6.4 Enhancing Figure of Merit:

To increase the figure of merit (ZT), researchers aim to simultaneously increase the power factor (through a combination of high Seebeck coefficient and high electrical conductivity) and decrease the thermal conductivity. This can be achieved through various strategies:

Nano structuring: Creating nanostructures in the material can scatter phonons (heat carriers), reducing thermal conductivity while maintaining electrical conductivity.

Doping: Introducing dopants into the material's crystal structure can alter the electronic and thermal transport properties, optimizing power factor and thermal conductivity.

Engineering Band Structure: Designing materials with specific electronic band structures can lead to high power factors by enhancing carrier mobility and Seebeck coefficient.

Phonon Engineering: Controlling phonon scattering through boundary effects, point defects, or alloying can reduce thermal conductivity.

6.4.1 High-Entropy Materials:

High-entropy materials, or high-entropy alloys (HEAs), have gained attention for their unique properties. HEAs are composed of multiple principal elements in roughly equal proportions, leading to enhanced mechanical, electrical, and thermal properties. In thermoelectric applications, HEAs can offer novel combinations of properties that can be advantageous for achieving high ZT values. The complex microstructure of HEAs can lead to enhanced phonon scattering, reducing thermal conductivity, while their unique electronic structures can result in high power factors. By tuning the composition and structure of HEAs, researchers are exploring new avenues for efficient thermoelectric materials.

High-entropy materials (HEMs), also known as high-entropy alloys (HEAs), exhibit unique microstructural characteristics that contribute to enhanced phonon scattering and reduced thermal conductivity. This behavior arises from the combination of multiple principal elements in roughly equal proportions, leading to complex crystal structures, lattice distortions, and local compositional fluctuations. These factors create an environment conducive to increased phonon scattering, which in turn lowers thermal conductivity. Here's why HEMs offer higher phonon scattering and reduced thermal conductivity:

Complex Microstructure: The presence of multiple elements with different atomic sizes and masses in HEMs results in a disordered and complex crystal structure. This disorder leads to various types of lattice defects, such as point defects, grain boundaries, and interfaces, which act as scattering centers for phonons (heat carriers). Phonons encounter different types of atomic environments as they move through the lattice, leading to frequent scattering events that hinder their propagation and reduce thermal conductivity.

Local Composition Variations: HEMs often exhibit local composition variations due to the diverse mixture of elements. These variations can lead to regions with different atomic arrangements and local stiffness, creating additional scattering centers for phonons. These variations also interfere with the long-range lattice order that typically facilitates efficient phonon transport.

Boundary Effects: The presence of numerous grain boundaries, phase boundaries, and interfaces in HEMs results in strong phonon scattering. The mismatch in crystal orientation and atomic arrangement at these boundaries disrupts the phonon propagation path, causing scattering and reducing the material's thermal conductivity.

Disorder-Induced Phonon Scattering: The atomic disorder in HEMs leads to anharmonic phonon-phonon interactions. These interactions create additional phonon scattering events, as the lattice vibrations deviate from the ideal harmonic behavior, causing phonons to scatter more frequently and reducing their thermal conductivity.

The reduction in thermal conductivity is highly advantageous for thermoelectric applications, where a low thermal conductivity is essential to maintain a large temperature gradient

across the material and enhance the Seebeck effect. While HEMs offer enhanced phonon scattering and reduced thermal conductivity, their impact on the thermoelectric figure of merit (ZT) depends on various factors, including the specific composition, temperature range, and target application.

HEMs have the potential to significantly enhance the figure of merit (ZT) compared to traditional materials, but the degree of improvement varies. Some HEMs have demonstrated substantial enhancements in ZT, especially when combined with other strategies like nano structuring and alloying. However, achieving a high ZT requires a careful balance between maximizing the power factor (Seebeck coefficient and electrical conductivity) and minimizing the thermal conductivity. Overall, while HEMs hold promise for advancing thermoelectric materials, the exact extent to which they can improve the figure of merit depends on the specific material design and the synergistic combination of multiple factors that influence thermoelectric performance.

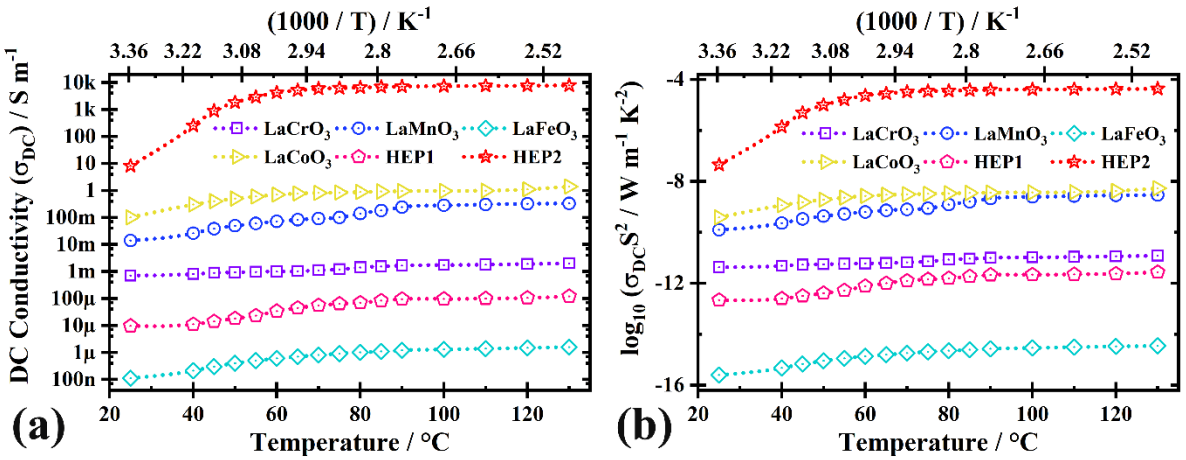

Figure 6.2: Temperature-dependence of (a) DC conductivity (σ_{DC}) and (b) logarithm of thermoelectric power factor [$\log_{10}(\sigma_{DC}S^2)$] for all six samples.

Doping is a commonly employed technique to modify the properties of materials, and in the context of thermoelectric materials like LaMO3 nanoparticles, doping can significantly influence their electrical conductivity and thermoelectric performance. Doping involves introducing foreign atoms into the crystal lattice of a material, which can alter the charge carriers' behavior and lead to changes in electrical conductivity and other properties.

6.5 Sr^{2+} Doping in La^{3+} Sites for p-Type Conductivity:

In LaMO3 nanoparticles, La is the lanthanum ion, and M represents the transition metal ion (e.g., Cr, Mn, Fe, Co). These materials typically exhibit n-type conductivity, where electrons are the dominant charge carriers. To generate p-type conductivity, one needs to introduce positive charge carriers (holes) that move in the opposite direction of electrons.

Sr^{2+} doping involves replacing some of the La^{3+} ions with Sr^{2+} ions. Since Sr^{2+} ions have fewer electrons in their outermost energy level than La^{3}+ ions, this substitution introduces electron vacancies or "holes" in the crystal lattice. These holes act as positive charge carriers and contribute to p-type conductivity.

Implications on Electrical Conductivity and Thermoelectric Figure of Merit (ZT):

Introducing p-type conductivity through Sr^{2+} doping in La^{3+} sites have several implications for electrical conductivity and thermoelectric performance:

Increased Hole Concentration: The presence of holes in the crystal lattice increases the overall hole concentration, enhancing the material's p-type conductivity.

Enhanced Electrical Conductivity: The presence of both electrons and holes leads to higher electrical conductivity due to the contribution from both types of charge carriers. This increased conductivity is beneficial for thermoelectric applications, as it enhances the material's ability to carry electric current.

Improvement in Thermoelectric Performance: The thermoelectric figure of merit (ZT) is a measure of how efficiently a material can convert heat into electricity. For p-type materials, ZT can be enhanced by increasing the power factor (product of Seebeck coefficient and electrical conductivity) and reducing thermal conductivity. Sr^{2+} doping can contribute to improved power factor by increasing hole mobility and concentration, leading to higher thermoelectric efficiency.

Optimization for Device Design: Generating p-type conductivity allows for the creation of complementary n-type/p-type thermoelectric modules, enabling more efficient thermoelectric devices. These devices can efficiently convert heat into electricity in a wider range of temperature gradients.

However, it's important to note that achieving high ZT requires careful optimization of both the power factor and the thermal conductivity. While Sr^{2+} doping introduces p-type conductivity and enhances the electrical conductivity, it might not directly reduce thermal

conductivity. Therefore, additional strategies such as phonon engineering, nano structuring, and alloying are often employed to lower thermal conductivity and maximize ZT.

6.5 Mott-Schottky plots

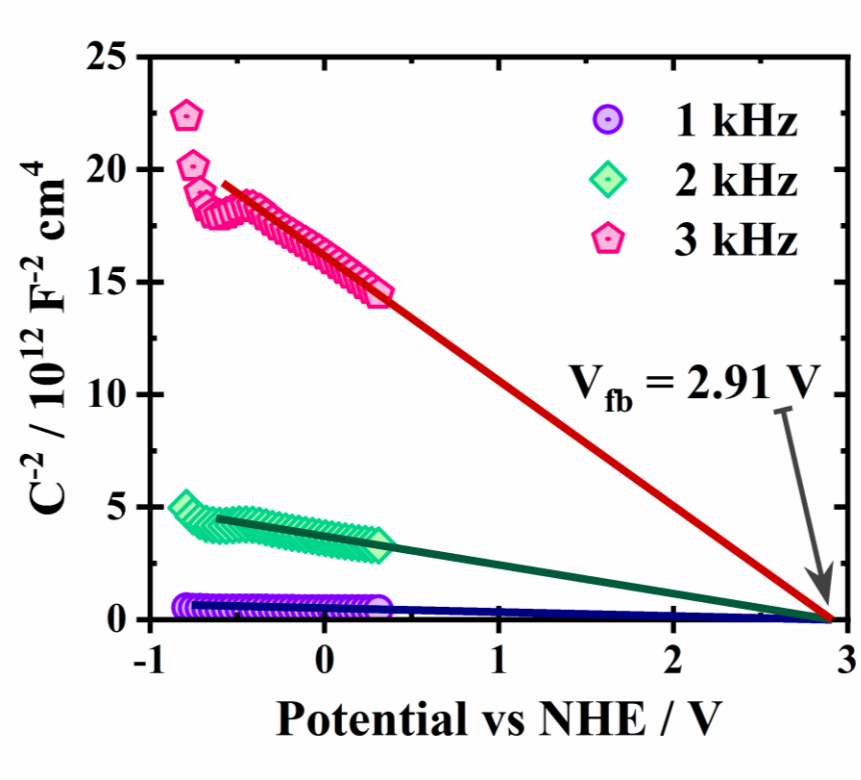

Figure 6.3: Mott-Schottky plots at 1,2, and 3 kHz frequencies for HEP-2.

The Mott-Schottky plots are generated at discrete frequencies of 1, 2, and 3 kHz using the Autolab PGSTAT (M204) electrochemical working station, which is under the control of Nova 1.1 software. These plots are established in conjunction with a three-electrode quartz cell configuration. Within the confines of this experimental setup, a solution of 0.5 (M) sodium sulphate (Na_2SO_4) is employed as the electrolytic medium. The Mott-Schottky plot, as delineated in Figure 9, serves as a convenient tool for the characterization of semiconductor properties and the determination of the conduction band edge's spatial disposition. The negative slope of extrapolated tangents evident across all investigated frequencies *viz*., 1, 2, and 3 kHz, unanimously corroborate the strong p-type conductivity attributes. This is highly anticipated for the excess hole-

doping amid one-third substitution of La^{3+} sites with Sr^{2+} ions. To quantify the flat-band potential (V_{fb}), the ensuing relationship is employed.

$$\frac{1}{C^2} = \frac{2}{eN_d\varepsilon A^2}\left(V - V_{fb}\right) \tag{30}$$

Here, C is the capacitance, e is the electronic charge, N_d is the doping density, ε signifies the permittivity of the material, and V stands for the applied voltage. Therefore, by discerning the point of intersection between the tangent line and the abscissa on the Mott-Schottky plot, a proximate estimation of the conduction band edge's position can be ascertained. Here, we obtain, $V_{fb} = +2.91$ V, relative to the potential of the normal hydrogen electrode (NHE).

To summarize, Sr^{2+} doping in La^{3+} sites can effectively generate p-type conductivity in LaMO3 nanoparticles, leading to increased electrical conductivity and potential enhancements in the thermoelectric figure of merit (ZT). However, achieving high ZT requires a comprehensive approach that balances both the power factor and thermal conductivity.

In conclusion, HEP-2 offers at least three orders of higher electrical conductivity and one order of lower thermal conductivity that can enhance the thermoelectric figure of merit manifold. Here, the Seebeck coefficient remains almost constant because of comparable DOS of the normal and high-entropy variants. Thus, HEP-2 can be used as a superior thermoelectric material.

7 Future scopes and Conclusion

7.1 Conclusion

After literature review, the perovskite samples' tolerance factors were calculated before successful synthesis, followed by characterization of the samples. Six samples were produced, namely LaCoO3, LaCrO3, LaFeO3, LaMnO3, $(La)_A(Cr_{1/4}Mn_{1/4}Fe_{1/4}Co_{1/4})_B O_3$, abbreviated as HEP-1 and $(La_{2/3}Sr_{1/3})_A(Cr_{1/6}Mn_{1/6}Fe_{1/6}Co_{1/6}Ni_{1/6}Cu_{1/6})_B O_3$, abbreviated as HEP-2, of which HEP-1 and HEP-2 were novel. The synthesis methodology involved citrate-based sol gel method, followed by high temperature sintering in air. Characterizations of the samples include Powder X-Ray Diffraction(XRD) followed by Rietveld refinement (for determining the crystal structure of materials), Field-Emission Scanning Electron Microscopy (FESEM) analysis (for size, shape, distribution, and overall morphology), Energy-Dispersive X-ray Spectroscopy (EDX) analysis (for composition of samples), Fourier-Transform Infrared Spectroscopy (FTIR) Analysis (for vibrational modes of molecules and materials), Diffuse Reflectance Spectroscopy (DRS) analysis (for electronic structure, band gaps, and optical properties). From XRD and Rietveld refinement and the literature, it is found that, LaMO3 crystallizes in an orthorhombic lattice (typically $Pnma$) if M = Cr, Mn, Fe; whereas a rhombohedral lattice (typically $R\bar{3}c$), if M = Co, Ni, Cu; HEP-1 takes the orthorhombic structure, whereas HEP-2 takes the rhombohedral structure. The spectrum of EDX analysis reveal the presence of lanthanum (La), the transition metal (M), and oxygen (O), helping to verify the stoichiometry of the compound. DRS analysis reveals optical band gap of samples ($LaCrO_3$ = 3.10eV, $LaMnO_3$ = 2.21eV, $LaFeO_3$ = 2.36eV, $LaCoO_3$ = 2.11eV, HEP-1 = 1.73eV, HEP-2 = 0.93eV). For LaMO3, the chemical composition by FTIR spectrum analysis reveals metal-oxygen stretching modes (400-700 cm^{-1}), lanthanum-oxygen stretching modes (400-700 cm^{-1}), M-O-M bending modes (600-1000 cm^{-1}), oxygen-hydroxyl or surface adsorption bands (3000-3800 cm^{-1}), and metal-oxygen vibrations (1000-1700 cm^{-1}). Thin films of samples made and tested for Seebeck coefficient using PT-DAQ setup, which was customized for this purpose. Seebeck coefficient (S) found were a) $LaCrO_3$; b) $LaMnO_3$; c) $LaFeO_3$; d) $LaCoO_3$; e) HEP-1; and f) HEP-2 is 77.47μVK^{-1}, 93.87μVK^{-1}, 47.28μVK^{-1}, 61.75μVK^{-1}, 149.81μVK^{-1}, 74.16μVK^{-1} respectively. Thermoelectric power factor $[\log_{10}(\sigma_{DC}S^2)]$ for all six samples were

calculated, of which least was of $LaFeO_3$(around -16), while highest was HEP-2(around -4). $LaFeO_3$ was found to be highly insulative, whereas the introduction of Sr^{2+} doping into HEP-2 marked a significant advancement by creating electron vacancies within the crystal lattice, inducing p-type conductivity and enhancement in electronic conductivity. It was realized that the increased configurational entropy due to the existence of disorder, particularly in samples of HEP-1 and HEP-2, which induce a profound effect of significant enhancement of phonon dispersion due to highly reduced mean free path of phonons, resulting in a remarkable decrease in thermal conductivity. The synergy of increased phonon dispersion, reduced thermal conductivity, and improved electronic conductivity culminated in a several orders of magnitude enhanced power factor . From Mott-Schottky plot, a proximate estimation of the conduction band edge's position can be ascertained. The flat-band potential $(V_{fb})$of HEP-2 obtained is $+2.91$ V, relative to the potential of the normal hydrogen electrode (NHE), suggesting Sr^{2+} doping in La^{3+} sites can effectively generate p-type conductivity in LaMO3 nanoparticles, leading to increased electrical conductivity and potential enhancements in the thermoelectric figure of merit (ZT). With the above enhancements, the thermoelectric figure of merit (ZT) is poised to soar by at least four orders of magnitude. The innovative design featuring two components at the A site, six at the B site, and O at the X site resulted in a system composed of eight components in AB, the highest reported in literature. The development and use of customized setup for thermoelectric data collection, ensuring uniformity in measurement periods gave excellent results. The findings indicate HEP-1 and, especially HEP-2 as highly superior thermoelectric materials. Their combination of enhanced power factor, reduced thermal conductivity, and improved electronic conductivity marks them as frontrunners in the quest for advanced thermoelectric materials.

7.2 Future Scopes

Pioneering the uncharted territories of High-Entropy Materials (HEMs) promises novel compositions with unparalleled thermoelectric prowess. Advancing doping strategies and advanced characterization techniques will illuminate the intricate mechanisms underlying material behavior. Collaborating with PT-DAQ opens avenues for real-time data analytics, while envisioning thermoelectric-powered wearables and sustainable thermal management reflects the alignment with future energy and environmental needs. This thesis is not an endpoint but a

launching pad for a cascade of innovations that will shape the future of thermoelectrics and sustainable energy solutions.

Further Investigation of High-Entropy Materials (HEMs):

Investigate other combinations of transition metal oxides to explore new HEMs with enhanced thermoelectric properties. Study the impact of different ratios of constituent elements on the thermoelectric performance of HEMs. Explore the effect of various synthesis methods and processing conditions on the properties of HEMs.

Optimization of Doping Strategies:

Explore additional dopants and their concentrations to fine-tune the electrical conductivity and thermoelectric performance of LaMO3 nanoparticles.

Investigate the interplay between different dopants and their impact on power factor, Seebeck coefficient, and thermal conductivity.

Advanced Characterization Techniques:

Incorporate advanced characterization techniques such as transmission electron microscopy (TEM), X-ray photoelectron spectroscopy (XPS), and Raman spectroscopy to gain deeper insights into the crystal structure, composition, and defect distributions of the synthesized materials. Utilize synchrotron-based techniques to study the electronic and phononic properties at a more detailed level.

Integration with Other Materials:

Explore the potential of hybrid materials by integrating LaMO3 nanoparticles with other materials, such as polymers or nanocomposites, to create multifunctional thermoelectric devices.

Enhanced Thermoelectric Device Fabrication:

Investigate innovative fabrication techniques to create more efficient thermoelectric devices using the synthesized materials, such as thin-film deposition methods or 3D printing technologies. Possibilities of making improved thermocouple devices using LaMO3 materials.

PT-DAQ Integration and Advancements:

Collaborate with PT-DAQ for further development of data acquisition systems tailored for thermoelectric material characterization.

Incorporate real-time data analysis capabilities into PT-DAQ, allowing researchers to analyze thermoelectric properties directly during experimentation.

Explore wireless data transmission options to enhance the flexibility and convenience of thermoelectric property measurements.

Energy Harvesting Applications:

Explore the integration of thermoelectric materials into wearable devices like nano generators for energy harvesting from body heat, offering potential applications in wearable electronics and medical sensors.

Thermal Management Solutions:

Investigate the use of thermoelectric materials for heat dissipation and thermal management in electronic devices, offering a sustainable alternative to traditional cooling methods.

Material Design via Computational Methods:

Employ computational modeling and simulations to predict the thermoelectric properties of novel materials, guiding the synthesis process for optimized performance.

Environmental Sustainability and Applications:

Study the environmental impact and potential eco-friendly applications of thermoelectric materials, particularly in energy-efficient cooling and waste heat recovery systems.

DFT calculation on phonon dispersion and estimation of entropy enthalpy.

The presented thesis provides insights on thermoelectric properties in LaMO3 nanoparticles, driven by empirical investigation and theoretical underpinnings. Building upon this foundation, a promising avenue for future exploration lies in the realm of Density Functional Theory (DFT) calculations applied to phonon dispersion and the computation of entropy and enthalpy.

DFT, a cornerstone of modern materials science, offers a robust framework for delving deeper into the vibrational properties of materials. By elucidating phonon dispersion – the dispersion relations governing the vibrational modes – the intricate lattice dynamics and heat-carrying characteristics of LaMO3 nanoparticles can be unveiled. This avenue would enable a more nuanced understanding of heat transport mechanisms and thus enrich the interpretation of thermal conductivity findings.

Furthermore, the calculation of entropy and enthalpy, informed by DFT-driven insights, stands as a vital endeavor. These thermodynamic properties wield considerable influence in dictating the temperature-dependent behaviors of materials. The application of DFT to compute these properties can enable a comprehensive grasp of phase transitions, stability, and thermal

response under varying conditions. This, in turn, can lay the groundwork for optimizing the thermoelectric performance of LaMO3 nanoparticles within a diverse array of operating environments.

As thermoelectric materials strive to harmonize efficiency with environmental considerations, the calculated entropy and enthalpy can act as guiding lights for designing and engineering more robust thermoelectric devices.